

NORTHWESTERN UNIVERSITY

Graphene Hydrogel Materials for Next Generation Energy Storage Devices

A DISSERTATION

SUBMITTED TO THE GRADUATE SCHOOL IN PARTIAL FULFILLMENT OF THE
REQUIREMENTS

For the degree

DOCTOR OF PHILOSOPHY

Field of Materials Science and Engineering

By

Thomas (Yue Yang) Yu

EVANSTON, ILLINOIS

September 2018

ABSTRACT

Graphene Hydrogel Materials for Next Generation Energy Storage Devices

Thomas (Yue Yang) Yu

Electrochemical energy storage devices have become increasingly relevant to the operation and sustainability of the modern world, as proliferation of mobile electronics, renewable electrical energy generators, electrical vehicles, and various high-tech bio-medical sensing device continues. The widespread need of easier to produce, better performing, and multifunctional energy storage materials in these applications is becoming increasingly urgent. It is particularly demonstrated in energy storage devices such Li-ion batteries and supercapacitors, where the intense research in the last two decades have yet to satisfy the consumer and industrial demand for better material design. One candidate material has been met with intense interests in the recent years. Graphene, and its chemical derivatives, graphene oxide and reduced graphene oxide, offer potential scalable material solutions for higher performing battery and supercapacitor materials. Due to its unique chemical structure, graphene has excellent chemical stability and high electrochemical performance. And its chemical derivative, graphene oxide, offers scalable and cost-effective processing methods due to its hydrophilic nature and ability to be easily manipulated via simple solution-based chemistry. Nonetheless, majority of contemporary studies have not fully utilized the potential benefits of graphene, due to the limitation of the two-dimensional electrode design where graphene layers are often closely packed into dense films and coating, and thereby reducing its active surface sites in electrochemical applications resulting in decreases the performance of the constructed devices.

In this dissertation, the development of a novel class of graphene based materials, graphene hydrogel, is discussed in detail. The free-standing, three-dimensional, and highly porous structure

of the graphene hydrogel is composed of loosely stacked and cross-linked graphene sheets, resulting in higher specific surface area and increase in electrochemical active sites when compared to the two-dimensional graphene films. Implementation of the graphene hydrogel materials were successfully demonstrated in both Li-ion battery and supercapacitor devices in this dissertation.

For battery application, a porous 3D graphene hydrogel composite embedded with Si nanoparticles coated with an ultrathin SiO_x layer is successfully synthesized using a solution-based self-assembly process. The excellent electrochemical performance can be attributed to the porous, open cell 3D structure of graphene hydrogel, which provides a large internal space and flexible, electrically conductive graphene matrix that can accommodate volumetric changes of Si nanoparticles. Its highly porous 3D structure of high specific surface area allows rapid diffusion of Li-ions and easy penetration of electrolyte, resulting in high specific capacity even at high current density.

A polyurethane supported graphene hydrogel composite was fabricated and used as flexible electrode material for supercapacitors. Nano and micro-particles of electrochemically active materials, graphite and MnO_2 , were mixed with graphene oxide solution and then treated with a mechanical spray dry method. The resulting powder consists of the said active materials wrapped with graphene oxide sheets. The hydrophilic nature of the graphene oxide wrapping allows for even suspension of hydrophobic active materials in aqueous suspension. Graphene hydrogel can then be synthesized through hydrothermal reduction of the aqueous suspension of such composite particles, with even distribution of active hydrogel throughout the hydrogel microstructure. Through mechanical and electrochemical testing, the hydrogel electrode material demonstrated its capability as highly flexible supercapacitor electrode. The resulting understanding in the

fabrication and electrochemical properties of such composite system paved the foundation for the designs of future multifunctional electrode materials capable of withstanding high degree of elastic deformation.

Both the electrochemical and mechanical properties of this three-dimensional electrode material were studied in detail. The formation of stress induced surface defects on graphene coating were reported in this dissertation. These stress induced defects exposed edge planes of graphene layers to electrolyte solution and resulted in significantly increase in the electrochemical activity of the material. Such phenomenon was not previously reported in literature and offered new insights on the effects of mechanical deformation have on interaction between electrolyte and flexible graphene based electrode. The effects of intercalated monovalent and divalent cations have on the mechanical properties of the graphene hydrogel were also observed. Graphene hydrogel samples were treated with solutions of monovalent and divalent salts. The graphene hydrogel samples were able to retain trace amount of monovalent and divalent ions, resulting noticeable increases to the elastic modulus of the graphene hydrogel, particularly in samples treated with divalent cations Mg^{2+} and Ca^{2+} . The results correlate with previous studies conducted on two-dimensional graphene structure.

ACKNOWLEDGEMENTS

Above all, I would like to thank Prof. Harold Kung and Mayfair Kung for their guidance and support throughout my graduate study. Whether it is offering tips and directions on our research projects, engaging in stimulating discussion, or helping me finding right setup to conduct the numerous experiments that I have conducted over the years. They have been extremely kind and understanding to me ever since I met them.

I would also like to thank my thesis committee advisors, Prof. Scott Barnett, Mark Hersam, and Yip-wah Chung, for taking the time out of their busy schedule to assist me in completing this final phrase of my doctoral program. In addition, I would like to thank these individuals for their excellent teaching of the courses I have attended during my graduate and undergraduate studies at Northwestern University. I would particularly like to thank Scott Barnett for the mentorship I received during my BS/MS research and the informative electrochemistry course he taught, which piqued my interests in electrochemical energy storage. I want to thank Mark Hersam as well for the engaging nanotechnology course I taken as an undergrad that raised my interests in applications of graphene materials. I also want to thank Prof. Jiaxing Huang and Monica Olvera de la Cruz, who assisted me during my qualifying exam two years ago.

My work at my research group could not be possible without the help I received from the wonderful lab mates and alumni of our research group, Renee Xuejun Bai, Cary Hayner, Kevin Kai Han, and Jingmei Shen. I would also like to thank Yuan Li, Xuan Dou, Zhenyu Bo, Zhi Lu, and many other friends I made over the years during graduate school—for their help and the memorable moments we shared in this chapter of our life. I particularly want to thank Cary for teaching me everything he can when I first joined the Kung group and the mentorship he generously provided over the years.

Many of my experiments could not be possible without help and training I received from Jinsong Wu, Ben Myers, Xinqi Chen, Eric Miller, and Karl Hagglund at NUANCE, Mark Seniw at CLaMMP, and Jerrold Caresllo at X-Ray Diffraction Facility, and Denis T. Keane at Argonne National Laboratory. Their diligent support and exceptional training were critical to the completion of my doctoral study. I would also like to thank my team at SiNode Systems, Cary Hayner, Josh Lau, and Samir Mayekar, who kept me motivated during the last five years despite the ups and downs one unavoidably encounters in a doctoral program. They made me realized the skills and experience I gained as a graduate student goes way beyond the academic environment. That said though, I probably would have completed my thesis a few months earlier had I run fewer samples for you guys. I kid!

Last but not least, I want to express my foremost gratitude to my mother and father, for doing everything that they can to provide me the best support and guidance that I can possibly receive since I arrived at this world. Of course, I want to thank my girlfriend→fiancé→wife, Shelley Liu, for the emotional support and motivation that contributed to my drive for greater heights, despite the long distance between us during both of our graduate school careers. I have to say, I am not sure I could have pulled through with this degree without you, my dear. Finally, I would like to thank the rest of my extended family for their relentless support over the years.

TABLE OF CONTENTS

List of Figures	8
List of Tables	13
Chapter 1: Introduction	14
Chapter 2: Background Information	16
2.1 Graphene and its Chemical Derivative, Graphene Oxide.....	16
2.2 Self-assembled Graphene and Graphene Oxide Hydrogel	17
2.3 Graphene-based Li-ion Battery Electrode Materials	19
2.4 Graphene-based Supercapacitor Electrode Materials	21
Chapter 3: General Experimental Procedures	23
Chapter 4: Si@SiO_x/graphene Hydrogel Composite Anode for Lithium-ion Battery	27
Chapter 5: Electrochemical Properties of Reduced Graphene Oxide Thin Film on 3D Elastomeric Substrate	47
Chapter 6: Reduced Graphene Oxide Hydrogel Embedded Polyurethane Composite as Elastomeric Supercapacitor Electrode Materials	80
Chapter 7: Effects of Ion Infiltration on the Mechanical Properties of Free Standing Reduced Graphene Oxide Hydrogel	96
Chapter 8: Conclusion and Recommendations for Future Work	109
References	112

LIST OF FIGURES

- Figure 2.1** Schematic diagrams[1] showing a) 3-D graphite lattice with individual graphene layers and b) zigzag and armchair edge planes in graphene
- Figure 3.1** Schematic showing elements of simplified Randles cell equivalent circuit model in relationship to double layer of supercapacitors.
- Figure 4.1** Schematic illustration of procedure to synthesize Si@SiO_x/GH composites, with insert showing the digital images of the samples.
- Figure 4.2** (a-d) TEM images of Si@SiO_x-1, -2, -3, -4 respectively with HRTEM image inserted, showing amorphous SiO_x layer of 1.3, 1.7, 2.4, and 4.2 nm, respectively; (e) high-resolution XPS spectra of Si 2p for the Si@SiO_x nanoparticles.
- Figure 4.3** SEM images of Si@SiO_x/GH composite: (a) Si@SiO_x-1, (b) Si@SiO_x-2, (c) Si@SiO_x-3, (d) Si@SiO_x-4 (or named Si@SiO_x/GH-1) with insert showing the EDS spectrum, (e) Si@SiO_x/GH-2, and (f) Si@SiO_x/GH-3. Arrows indicate cluster of Si@SiO_x nanoparticles.
- Figure 4.4** (a) XRD patterns of GO, Si@SiO_x-4, and Si@SiO_x-1; (b), (c), and (d) Raman spectrum, survey scan of XPS spectra, and high resolution C 1s XPS spectra of Si@SiO_x/GH-1, respectively; (e) TGA curves of Si@SiO_x/GH composites, GH, and Si@SiO_x-4.
- Figure 4.5** (a) Rate cycle performance of Si@SiO_x/GH composites and (b) galvanostatic charge-discharge profiles of Si@SiO_x/GH-1 at various current densities as marked; (c) Cyclic voltammograms of the Si@SiO_x/GH-1 in the initial five cycles at 0.1 mV/s. For Si@SiO_x/GH-1, 1 A g⁻¹ corresponded to about 12 mA cm⁻² for an active component of about 30 mg cm⁻².
- Figure 4.6** SEM images of Si@SiO_x/GH-1 anode after rate cycles test.
- Figure 4.7** SEM images of Si@SiO_x particles: (a) Si@SiO_x-1, (b) Si@SiO_x-2, (c) Si@SiO_x-3, (d) Si@SiO_x-4.
- Figure 4.8** Low- and high-magnification SEM images of GH.

- Figure 4.9** Low magnification SEM images of graphene hydrogel combines with Si@SiO_x particles: (a) Si@SiO_x-1, (b) Si@SiO_x-2, (c) Si@SiO_x-3, (d) Si@SiO_x-4.
- Figure 4.10** Cycling performances of GH anode at 100mA g⁻¹ between 0.01 and 2.0 V.
- Figure 4.11** Cyclic voltammograms of the GH in the initial five cycles at 0.1mV/s and the voltage is between 0.01 and 2.0 V
- Figure 5.1** Scheme showing steps employed to form a PU-rGO foam sample.
- Figure 5.2** SEM images of: (a, b) pristine PU foam; (c, d) PU-rGO-1; (e, f) PU-rGO-3; inset in e is cross-sectional image obtained using FIB, with the rGO layer highlighted by arrows. From additional images (Figure S1), the thickness was estimated to be 570±185 nm; and (g, h) PU-rGO-5; inset in g is cross-sectional image with rGO layer highlighted, and the thickness was estimated to be 1260±220 nm (Figure S2).
- Figure 5.3** High-resolution XPS C1s spectra of (a) untreated rGO thin film, (b) PU-rGO-1 single coated and (c) PU-rGO-5 five times coated composite samples after ethylenediamine and hydrazine hydrothermal reduction, and (d) PU-rGO-1 single coated composite sample after only ethylenediamine hydrothermal reduction.
- Figure 5.4** XRD patterns of sample (a) PU-rGO-1 single coated composite sample after only ethylenediamine hydrothermal reduction, (b) PU-rGO-1 single coated composite sample after ethylenediamine and hydrazine hydrothermal reduction.
- Figure 5.5** SEM images of PU-rGO-3 foam at different compressive strain (vertical compression): (a) 0%, (b) 10%, (c) 20%, (d) 30%, (e) 40%, (f) 50%, (g) 60%, and (h) 70%. The scale bar is 300µm.
- Figure 5.6** (a) Resistance of a PU-rGO-3 foam at different compressive strain after 2, 50, and 100 repeated cycles of compression; (b) Resistance of PU-rGO-1,3,5 samples as a function of applied compressive strain after 100th cycle of compression.

- Figure 5.7** (a) Capacitance of a PU-rGO-5 foam electrode as a function of compressive strain; (b) Its EIS data at corresponding compressive strain, with illustration of equivalent circuit used for obtaining the fitted resistance values.
- Figure 5.8** (a) Schematic cross-sectional diagrams of a coating of stacked graphene layers (black) on a PU substrate (yellow) and (b and c) after bending due to compression, showing tension-induced formation of micro-fracture. (d) SEM image of PU-rGO-3 under 70% compression strain, exhibiting facial micro-cracks of the rGO coating.
- Figure 5.9** FTIR spectra of polyurethane foam in as received condition, after 4 hours of hydrothermal treatment at 100 °C with ethylenediamine, and same sample as after additional 3 hours of submersion in 65 wt. % hydrazine monohydrate solution at 80 °C.
- Figure 5.10** SEM images of (a) as received PU foam, (b) PU foam after 4 hours of hydrothermal treatment at 100 °C with ethylenediamine, (c) same sample as (b) after 3 hours of submersion in 65 wt.% hydrazine monohydrate solution at 80 °C.
- Figure 5.11** XPS C1s spectra of (a) as received PU, (b) PU foam after 4 hours of hydrothermal treatment at 100 °C with ethylenediamine, (c) same sample as (b) after additional 3 hours of submersion in 65 wt.% hydrazine monohydrate solution at 80 °C.
- Figure 5.12** XPS N1s spectra of (a) untreated rGO thin film, (b) PU-rGO-1 single coated and (c) PU-rGO-5 five times coated composite samples after ethylenediamine and hydrazine hydrothermal reduction, and (d) PU-rGO-1 single coated composite sample after only ethylenediamine hydrothermal reduction.
- Figure 5.13** SEM images of FIB milled PU-rGO-3 at 4 separate regions. No Pd coating was applied for these samples. The thickness of the rGO was measured every μm for all four images to arrive an average of 570 nm, with a standard deviation of 185 nm.
- Figure 5.14** FIB milled SEM images of PU-rGO-5 at 4 individual regions. No Pd coating was applied to these samples. The thickness of the rGO

was measured every μm for all four images to arrive an average of 1260 nm, with standard deviation of 220 nm.

- Figure 5.15** Compressive stress-strain (S-S curves) of polyurethane foam in as received condition and after 4 hours of hydrothermal treatment at 100 °C with ethylenediamine plus additional 3 hours of submersion in 65 wt.% hydrazine monohydrate solution at 80 °C.
- Figure 5.16** X-ray tomography setup.
- Figure 5.17** X-ray tomography images of PU-rGO-3 foam under (a) 0%, (b) 30%, (c) 50%, (d) 60%, and (e) 70% uniaxial compression.
- Figure 5.18** I-V curves of PU-rGO-3 with different compressive strain.
- Figure 5.19** (a) A schematic diagram of the electrochemical testing device; Comparison of CV curves of PU-rGO foam with different compressive strain at (b) 10 mV s^{-1} , (c) 50 mV s^{-1} , and (d) 100 mV s^{-1} .
- Figure 6.1** Diagram showing the functional principle of Buchi Mini Spray Dryer B-290. Diagram is retained from Technical Data Sheet publicly available from www.buchi.com
- Figure 6.2** SEM images of (a) as-received graphite particles after sonication, (b) spray-dried graphene oxide wrapped graphite particles, (c) as-received MnO_2 particles, (b) spray-dried graphene oxide wrapped MnO_2 particles. Scale bar is 25 μm .
- Figure 6.3** SEM images of G-PGH under (a) 35X and (b) 350X magnifications and Mn-PGH under (c) 35X and (d) 350X magnifications. Corresponding scale bars are shown within each image.
- Figure 6.4** Stress-strain measurement of as-received PU foam, G-PGH, and Mn-PGH samples.
- Figure 6.5** XPS spectrum of (a) C 1s and (b) O 1s of G-PGH, (c) C 1s, (d) O 1s, (e) Mn 2p, and (f) Mn 3s of Mn-PGH
- Figure 6.6** Resistance of G-PURGOH and Mn-PURGOH electrode samples under compressive strain of 0 to 70% and after 0, 50, and 100 repeated cycles of 70% compression

- Figure 6.7** Capacitances of (a) GO-G and (b) GO-Mn samples under 0.05 A g^{-1} , 0.1 A g^{-1} , and 0.5 A g^{-1} and under compressive strain of 30%, 40%, 50%, and 70%. EIS spectrum of (c) GO-G and (d) GO-Mn samples under compressive strain of 30%, 40%, 50%, and 70%.
- Figure 7.1** SEM images of (a) control, (b) 2M HCl, (c) 1M MgCl₂, (d) pore walls of rGOH. (e) Reduced graphene oxide hydrogel (rGOH) samples after ion infiltration and vacuum drying.
- Figure 7.2** XPS spectrum of (a) C 1s and (b) O 1s peaks of control sample of rGOH.
- Figure 7.3** XPS spectrum of (a) Li 1s peak of 1M LiCl, (b) Na 1s peak of 1M NaCl, (c) K 2p peak 1M KCl, (d) Mg 2p peak of 1M MgCl₂, (e) Ca 2p peak of 1M CaCl₂ infiltrated rGOH samples.
- Figure 7.4** Stress-strain curves of (a) control and (b) 1M MgCl₂ infiltrated rGOH samples under 6 repeated cycles of compression up to 70% strain.
- Figure 7.5** Elastic modulus of rGOH samples from batch 1, 2, and 3.

LIST OF TABLES

Table 4.1	Abundance ratios of the different Si oxidation states present in the Si@SiO _x nanoparticles, calculated by curve fitting of the Si 2p spectra.
Table 5.1	EIS fitting results of PU-rGO-5.
Table 7.1	List of solutions used for ion-infiltrated rGOH samples and the resulting weight percentage of ions from ICP
Table 7.2	Average moduli of each hydrogel samples across all three batches.

CHAPTER 1

Introduction

In the past decade or so, research interest in portable energy storage devices has burgeoned due to the widespread use of portable electronics in the consumer and industrial applications, including wearable devices and bio-medical sensors and implants. To power these electronics, new class of material designs for energy storage devices need to be explored.

Reduced graphene oxide hydrogel is a free-standing three-dimensional material that is both electrically conductive and highly electrochemically active. In addition, it can retain excellent mechanical flexibility, structural and chemical stability, and high specific surface area, making it an excellent material candidate for multifunctional energy storage device for next generation of mobile and flexible electronics.

This dissertation detailed the development of novel composite reduced graphene oxide hydrogel materials for Li-ion batteries and electrochemical capacitors and new findings on the electrochemical and mechanical properties of this material. First, the background information required for understanding the discussed work is presented in Chapter 2. This chapter offers an overview of contemporary knowledge on the recent development in Li-ion battery and electrochemical capacitors utilizing graphene as part of the material design. In particular, graphene-based three-dimensional hydrogel, including its synthesis, materials characterizations, and applications, is discussed in detail.

In Chapter 3, the experimental techniques used to gather the results reported in the following chapters are presented, providing the fundamental understanding of the experimental techniques used in this study.

Chapter 4 reports the original work conducted on the synthesis and characterization of a novel silicon embedded graphene hydrogel anode material for li-ion battery.

For Chapter 5, the author reports the effects of surface defects have on graphene thin film and its electrochemical performance as a supercapacitor material. The results discussed here was discovered during author's attempt to fabricate an elastomeric supercapacitor material.

Chapter 6 then discussed the fabrication and characterization of a novel elastomeric composite supercapacitor electrode material, using a polyurethane supported foam matrix with embedded reduced graphene oxide hydrogel with high loading of graphite and MnO₂ nanoparticles to further improve its electrochemical performance.

In Chapter 7, the author discussed effects of different cations, infiltrating the graphene hydrogel, have on the mechanical properties of the hydrogel itself. In particular, the changes to elastic modulus of the hydrogel after ion-infiltration were investigated.

Chapter 8 offered a conclusion for this thesis and recommendations for prospective work.

CHAPTER 2

Background Information

2.1 Graphene and its Chemical Derivative, Graphene Oxide

Graphene has emerged in the past decade as excellent candidate for energy storage material, due to its superior chemical and physical properties. It can be prepared through a wide range of methods: historical method of thermal decomposition of graphite oxide followed by the reduction of graphene oxide to graphene[2] resulting in few- and multilayer graphene structures[3]; CVD growth typically done through metal catalysts[4]; mechanical cleavage of graphite (also known as the Scotch tape method)[5]; unzipping of carbon nanotubes[6]; and electrochemical exfoliation of graphite[7]; and etc. Graphene and its chemical derivatives, graphene oxide (GO) and reduced graphene (rGO), are constructed out of a single plane of sp^2 hybridized carbon atoms, with the exception of functional groups (such as phenol, hydroxyl, epoxide, and carboxylic acids groups[8]) on GO and non-fully-reduced GO. Its unique chemical structure offered exceptional optical, electrical, mechanical, and electrochemical properties that are still not fully explored even after decade of high intensity research. Graphene, along with GO and rGO, offers incredibly high specific surface area of $+2600 \text{ m}^2 \text{ g}^{-1}$, which contribute to their excellent electrochemical properties and making them extremely favorable for applications in energy storage devices. Graphene oxide (defined as a single layer of graphite oxide)[9, 10] can be prepared from graphite through oxidization to graphite oxide. The graphite oxide is then exfoliated to graphene oxide through a variety of methods, including simple sonication, mechanical stirring of the water/graphite oxide mixtures, and thermal exfoliation[10]. The properties of graphene are heavily depended on the preparation methods. In case of reduced graphene oxide, the graphene structure contains high amount of defects, such as Stone-Wales defects (which are pentagon and heptagon bonded to the

carbon basal plane[11]) and nanopores, to its original one-atom thick structure. These defects affect the chemical and electrochemical properties of graphene.

The sp^2 hybridized graphene contain two types of surfaces: the basal plane and edge planes; in addition, the edge planes can be separated into two types, zigzag and armchair (Figure 2.1). The edge site is known to exhibit higher electrochemical activity and offers capacitance several orders of magnitude higher than that of the basal plane[12, 13], as it is highly active due to the partial saturation of its valencies. It has been reported that each carbon atom of zigzag edge graphene has a non-bonding π -electron state, which is localized in the zigzag edges and enhance the local density of states near the Fermi energy, allowing it to be more chemically active with other reactants[14]. However, in the case of rGO sheets synthesized through solution chemistry, there exists roughly equal number of zigzag and armchair edge planes, minimizing the aforementioned effects.

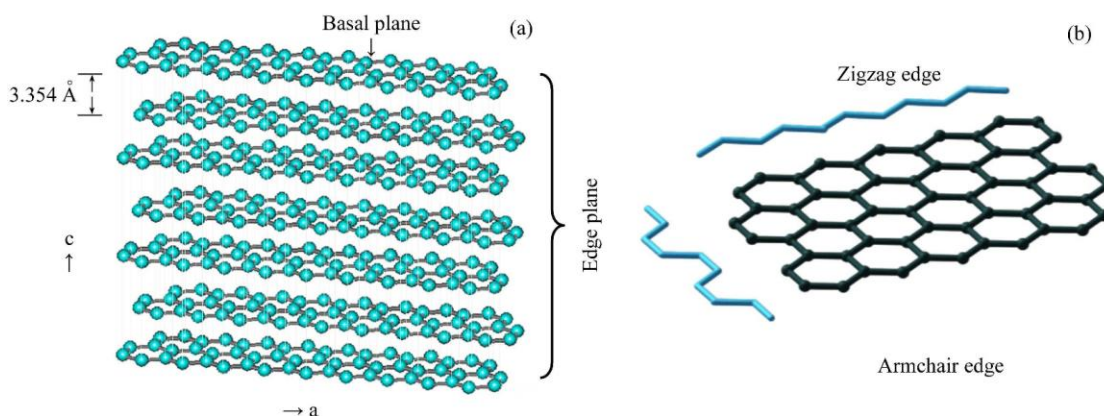


Figure 2.1 Schematic diagrams[1] showing a) 3-D graphite lattice with individual graphene layers and b) zigzag and armchair edge planes in graphene

2.2 Self-assembled Graphene and Graphene Oxide Hydrogel

Due to the two-dimensional structural of graphene and graphene oxide, the materials tend to exhibit poor dispersion and restacking during assembly into macroscopic film like structure for

application in electrochemical energy storage, as such restacking of graphene sheets tend to lower the high specific surface area resulting in lower than expected electrochemical performance. To overcome these challenges in fabrication, one of the approaches is to utilize the two-dimensional sheets to fabricate a free-standing, porous, three-dimensional graphene structure, often known as graphene hydrogel.

Graphene hydrogel is particularly interesting for electrochemical energy storage. The gel is composed of a solid network of loosely stacked and cross-linked graphene sheets interacting through physical and/or chemical bonds and could trap liquid weights orders of magnitude heavier than its own weight. Gel composed of graphene and/or graphene oxide networks can be synthesized through various procedures, including direct drying of graphene suspension and self-assembly of graphene, GO, and rGO sheets. The simplest method is via direct freeze drying of GO suspension to form GO aerogel[15-17]. Due to the high solubility and hydrophilic functional groups on GO, GO can be evenly dispersed and suspended in water at high concentration. Upon freeze drying, GO exhibits strong bonding interactions due to the hydrophobicity of its basal plane, allowing itself to assemble into a free-standing sponge like structure. GO in aqueous media can also be crosslinked by decreasing the pH of the GO solution. This results in an increase in hydrogel bonding and leads to the formation of a stable GO gelatin. Cross-linking agents can be added to the solution to increasing the bonding force between the sheets, including hydroxyl, oxygen-containing or nitrogen function group [gorgolis 2017 2d mater]. It has been reported that self-assembly of GO sheets to hydrogel can also be promoted by divalent and trivalent ions like Ca^{2+} , Mg^{2+} , Pb^{2+} , Cr^{3+} , and other.

To introduce electric conductivity and stability under moisture/aqueous environment, the GO structure needs to be reduced to rGO. Thermal reduction through high temperature of +500

°C in a dry inert environment or through strong reducing vapor can convert the GO gel into rGO[18, 19]. Graphene based hydrogel can also be synthesized via self-assembly assisted by thermal reduction. It has been widely reported that GO can be reduced in autoclave at moderately elevated temperature of 90 to 200 °C. The increase in temperature and solution pressure within the autoclave vessel induce self-assembly of GO into rGO hydrogel; variations of such hydrothermal reduction of GO suspension into rGO hydrogel have been successfully implemented across multiple studies[20-25]. The resulting dense hydrogel structure is held together by many π - π interactions and van der Waal forces between the reduced graphene oxide sheets.

2.3 Graphene-based Li-ion Battery Electrode Materials

Adapted from Xuejun Bai, Yue Yang Yu, Harold H. Kung, Baio Wang, Jianming Jiang, Journal of Power Sources, 306 (2016) 42-48.

With the widespread use of mobile electronic devices and increasing demand for electric energy storages in the transportation and energy sectors, lithium ion batteries (LIBs) have become a major research and development focus in the recent decade[26-28]. Since its introduction to the consumer market in the early 90s, the cathode of the LIBs has been consistently improved to the performance level of the current generation of mixed oxide, nanostructured materials[29-32]. Nonetheless, the energy and power density of most commercially available LIBs are still limited by the use of graphite as their anode materials, which has the theoretical capacity of 372 mAh g⁻¹[33]. Silicon (Si) has been considered as one of leading anode materials for next generation LIBs, due to its favorable working voltage and unsurpassed theoretical specific capacity of ~4200 mAh g⁻¹[34-36]. Major challenges still remain, as in the case of the volumetric changes (>300%)[37, 38] of untreated bulk Si particles that lead to rapid degradation of battery capacity.

Various approaches have been developed to improve the electrochemical performance of Si based anode. Popular strategies include the various uses of Si nanostructures, ranging from Si nanowires[39-42], nanotubes[43-45], and nanoparticles[46-48], to mesoporous[49-51] and core-shell Si structures[52-54]. In addition, various successes have been achieved through the use of Si in carbon-based composite[53, 55, 56]. Graphene, in particular, has been used as a stabilizing matrix for the Si active materials, due to its excellent electrical conductivity, mechanical flexibility, exceptional large specific surface area, and relative chemical stability. However, the resulting micro/nanostructures of these materials are limited to 1D (crumpled graphene nanoparticles)[57] and 2D constraints (graphene paper)[58, 59], which restrict the mobility of the lithium ions and electrolyte molecules within the electrode structure, thereby reducing the rate capacity and power density of the LIBs.

Graphene hydrogel (GH), as a freestanding porous 3D network, has received increasing attention for applications in electrochemical energy storage[60-62]. It retains the excellent electrical conductivity of conventional graphene papers. In addition, its unique hierarchical architecture reduces the occurrence of highly stacked graphene layers that is prevalent with various other graphene based electrode structure. This allows the electrolyte and lithium ion molecules to diffuse freely inside and throughout the electrode's structure[63] than the highly compacted, layered graphene sheets of the graphene papers[64-66]. Such properties of GH make it an ideal candidate as the supporting matrix of a novel Si-graphene composite LIBs anode. But challenges remain with the even distribution of silicon active materials within such composite's matrix, as Si nanoparticles tend to agglomerate in the aqueous solution that is used for the synthesis of GH and negatively affects the electrochemical performance of the said anode.

2.4 Graphene-based Supercapacitor Electrode Materials (add more stuff???)

Initial studies, dating back as far as 2007, utilized rGO as an electrochemically active material for EDLC application through simple physical mixture of the rGO particulates/powder, various binding agents, and carbon black filler materials[67], [68], which, nonetheless, have shown noticeable improvement in specific capacitance comparing to the performance of traditional activated carbon electrodes. Wang et al.[69] successfully demonstrated the use of free standing 2-D vacuum filtered graphene paper (GP) as a flexible EDLC electrode in the 2009 publication, thereby eliminating the need of capacity robbing filler and binding materials; in addition, the electrochemical performance of the device was further improved through an electropolymerization of the GP with a conducting polymer, polyaniline. Variation of the rGO and rGO-polyaniline flexible film electrodes have been successfully fabricated and studied since then[70], [71], [72]. Nonetheless, the definition of flexibility for these GP based 2-D electrodes is purely based on their ability to withstand bending motions, which being subject to negligible physical strain and deformation of graphene thin films due to the minimal thickness of the electrode. Alternative designs that derived from unzipped carbon nanotube (CNT) has been demonstrated as well[73]: [74], with impressive performance; although, large scale synthesis of these CNT derived graphene has proven to be challenging, owing to the complex and difficult manipulation of the CNTs as a precursor.

3-D rGO based electrodes have been successfully developed over the years, through the use of rGO based gels[75], [24], [76], with adequate mechanical properties. Other graphene-based electrodes with 3-D morphology has been studied, ranging from crumpled/corrugated graphene particles[77-79], deposited graphene coating on conducting metallic foam[80, 81], and engineered graphene structure through CVD[82], but these materials, while offer excellent electrochemical

performance, do not have the flexible mechanical properties desired by the intended applications of which this dissertation focuses on.

CHAPTER 3

General Experimental Procedures

3.1 Scanning Electron Microscopy (SEM)

The microstructure and the morphology of the samples was observed through a Hitachi SU8030 field emission high resolution scanning electron microscope. Relatively low acceleration voltage of 0.5-2 kV is used to prevent damaging the carbon-based materials during imaging.

3.2 Transmission Electron Microscopy (TEM)

TEM images in this dissertation were captured through the JEOL 2100-F microscope. The field emission gun's acceleration voltage was set at 200 kV.

3.3 X-Ray Photoelectron Spectroscopy (XPS)

Peak spectrum reported in this dissertation were measured using a Thermo Scientific ESCALAB 250Xi with X-ray source of Al K α (1486.6 eV). The binding energy scale was calibrated to adventitious carbon C 1s peak. Flood gun charge compensation was used for majority of the samples reported in this dissertation to improve the signal to noise ratio of the collected spectrum.

3.4 Focused Ion Beam (FIB)

In order to better observe some of the inner microstructural details of some graphene cated samples, the sample surface was ion-milled by FEI Helios Nanolab FIB to obtain a clear cross-

sectional image of samples. The observed microstructural features was measured digitally with ImageJ software.

3.5 Mechanical Testing

The stress-strain relationships were determined with mechanical tester, MTS Sintech 20G. A 10 lb load cell was calibrated prior to each test and then used to measure the forces exerted by the sample during the compression tests.

3.6 Electrochemical Testing

For Li-ion anode material tests, the electrochemical measurements were conducted using two-electrode CR2032 coin cells with lithium metal as the counter electrode. The electrolyte was consisted of 1 M LiPF_6 in ethylene carbonate/dimethyl carbonate (EC/DMC 1:1 vol. ratio). Celgard 2400 film was used as separator. Cell assembly was done in an argon-filled glove box (H_2O , $\text{O}_2 < 1\text{ppm}$). Galvanostatic cycling measurements were performed on BT2000 Potentiostat/Galvanostat system (Arbin Instruments) in the voltage range of 0.01-2 V vs Li^+/Li . Cyclic voltammogram (CV) and electrochemical impedance spectroscopy (EIS) were recorded by electrochemical workstation (Autolab PGSTAT128N). CV was tested at a scan rate of 0.1 mV s^{-1} within 2-0.01V and EIS were tested under the following conditions: open potential of 0.5 V, AC voltage amplitude of 10 mV, and frequency range from 10^6 to 0.01 Hz.

For tests involving electrochemical capacitors, a three electrodes setup was used, with sample electrode as the working electrode, Ag/AgCl (CH Instruments) as the reference electrode, and Pt foil (Alfa Aesar, 0.025mm, 99.9%) as the counter electrode. An aqueous solution of K_2SO_4 (0.5 M, Sigma Aldrich, 99% ACS) was the electrolyte. Using an electrochemical workstation

(Autolab PGSTAT128N), current at densities of 0.05 A/g, 0.1A/g, and 0.5 A/g, based on the weight of the active materials in the foam pieces, was applied to charge and discharge the sample over a voltage range of -0.2 to 0.6 V. Cyclic voltammetry (CV) was performed with a scan rate of 5 to 100 mV s^{-1} for a voltage scan of 0 to 1 V using a potentiostat/galvanostat system (Arbin Instrument BT2000).

EIS measurements were conducted in similar condition to that of Li-ion battery tests previously mentioned. For electrochemical capacitors, a simplified Randles cell model was used for equivalent circuit analysis.

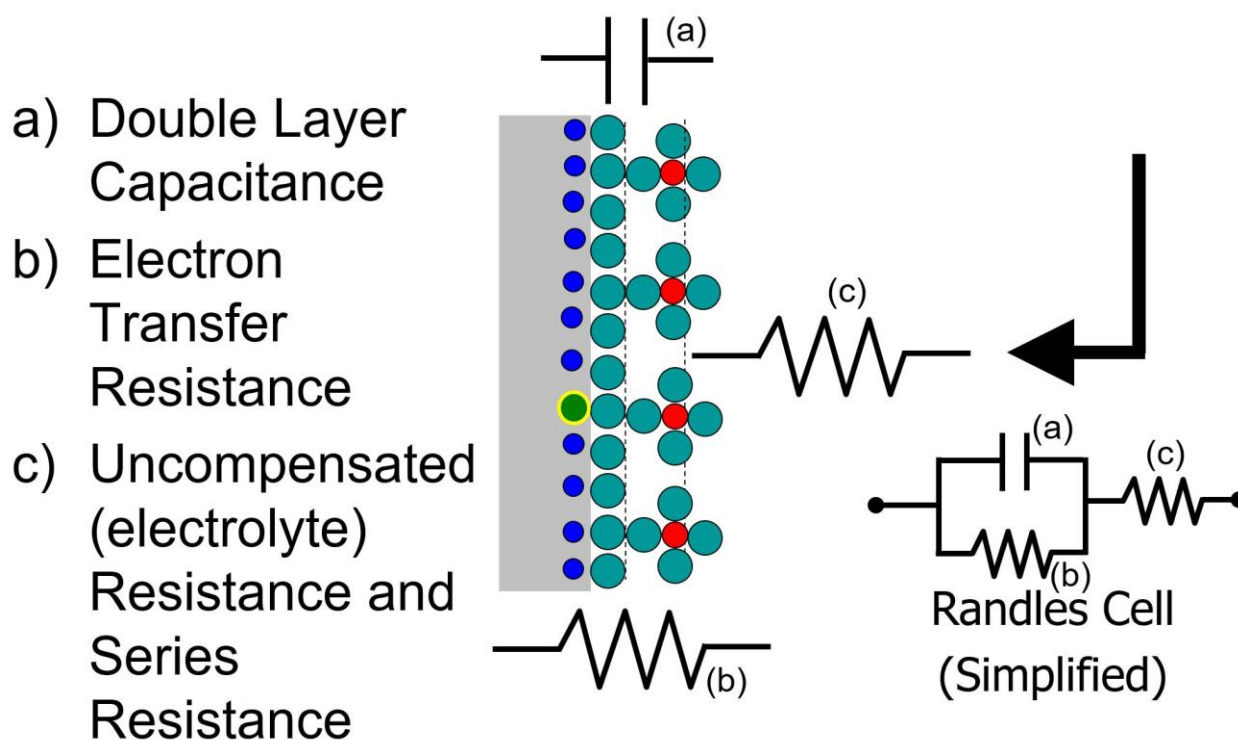


Figure 3.1 Schematic showing elements of simplified Randles cell equivalent circuit model in relationship to double layer of supercapacitors.

3.7 Synchrotron X-ray Tomography

Adapted from Yue Yang Yu, Xue Jun Bai, Mayfair C. Kung, Yeguang Xue, Yonggang Huang, Denis T. Keane, Harold H. Kung, *Carbon*, 115 (2017) 380-387.

X-ray tomography analysis was performed at Northwestern's Synchrotron Research Center at Sector 5 of Advanced Photo Source located at Argonne National Laboratory. Transmission tomograms of the samples were recorded at 6 keV using a monochromatic x-ray beam projected through a narrow gap, Si (111) monochromator. PU-rGO composite samples were cut into approx. 1 mm x 1mm x 5 mm stripes and then mounted inside a plastic 1 ml syringe. The sample-containing syringe was then mounted vertically on a rotating Newport stage with an attached goniometer (Figure 5.16). The samples are then aligned with the x-ray beam path and were turned at 0.2 degree increment for 180 degrees for the collection of x-ray tomograms. The beam was then projected on a phosphor screen, of which the resulting image was magnified by 10X and then captured by a Roper Scientific camera with 1300 x 1340, 24 micro pixels. Strain-induced structural changes of the samples can be captured using this setup through movement of the syringe plunger, which compressed the PU-rGO sample mounted within. The resulting raw images were then digitally reconstructed using Amira software for full 3D visualization of the samples.

CHAPTER 4

Si@SiO_x/graphene Hydrogel Composite Anode for Lithium-ion Battery

Adapted from Xuejun Bai, Yue Yang Yu, Harold H. Kung, Baio Wang, Jianming Jiang, *Journal of Power Sources*, 306 (2016) 42-48.

4.1 Abstract

A porous 3D graphene hydrogel (GH) composite embedded with Si nanoparticles coated with an ultrathin SiO_x layer (Si@SiO_x/GH) is successfully synthesized using a solution-based self-assembly process. The thickness of the SiO_x coating, formed by an ozone treatment of the 30-50 nm diameter Si particles, increases with the treatment temperature, and its formation results in the presence of Si²⁺ and Si⁴⁺ on the surface of the Si nanoparticles. The GH provides an electrically conducting network of interconnecting, micron-size open cells bounded by ultrathin stacked graphene sheets onto which the coated Si nanoparticles are dispersed. The agglomeration among the Si particles decreases with increasing extent of surface oxidation. Electrodes constructed with the Si@SiO_x/GH containing 71 wt.% Si@SiO_x exhibit a stable storage capacity of 1020 mAh g⁻¹ at 4 A g⁻¹ and 1640 mAh g⁻¹ after 140 cycles at 0.1 A g⁻¹. The outstanding electrochemical performance can be attributed to the porous, open cell 3D structure of GH, which provides a large internal space and flexible and electrically conductive graphemic matrix that can accommodate volumetric changes of Si nanoparticles and a highly porous 3D structure of high specific surface area that allows rapid diffusion of Li-ions and easy penetration of electrolyte.

4.2 Introduction

With the widespread use of mobile electronic devices and increasing demand for electric energy storages in the transportation and energy sectors, lithium ion batteries (LIBs) have become a major research and development focus in the recent decade[26-28]. Since its introduction to the consumer market in the early 90s, the cathode of the LIBs has been consistently improved to the performance level of the current generation of mixed oxide, nanostructured materials[29-32]. Nonetheless, the energy and power density of most commercially available LIBs are still limited by the use of graphite as their anode materials, which has the theoretical capacity of 372 mAh g⁻¹[33]. Silicon (Si) has been considered as one of leading anode materials for next generation LIBs, due to its favorable working voltage and unsurpassed theoretical specific capacity of ~4200 mAh g⁻¹[34-36]. Major challenges still remain, as in the case of the volumetric changes (>300%)[37, 38] of untreated bulk Si particles that lead to rapid degradation of battery capacity.

Various approaches have been developed to improve the electrochemical performance of Si based anode. Popular strategies include the various uses of Si nanostructures, ranging from Si nanowires[39-42], nanotubes[43-45], and nanoparticles[46-48], to mesoporous[49-51] and core-shell Si structures[52-54]. In addition, various successes have been achieved through the use of Si in carbon-based composite[53, 55, 56]. Graphene, in particular, has been used as a stabilizing matrix for the Si active materials, due to its excellent electrical conductivity, mechanical flexibility, exceptional large specific surface area, and relative chemical stability. However, the resulting micro/nanostructures of these materials are limited to 1D (crumpled graphene nanoparticles)[57] and 2D constraints (graphene paper)[58, 59], which restrict the mobility of the lithium ions and electrolyte molecules within the electrode structure, thereby reducing the rate capacity and power density of the LIBs.

Graphene hydrogel (GH), as a freestanding porous 3D network, has received increasing attention for applications in electrochemical energy storage[60-62]. It retains the excellent electrical conductivity of conventional graphene papers. In addition, its unique hierarchical architecture reduces the occurrence of highly stacked graphene layers that is prevalent with various other graphene based electrode structure. This allows the electrolyte and lithium ion molecules to diffuse freely inside and throughout the electrode's structure[63] than the highly compacted, layered graphene sheets of the graphene papers[64-66]. Such properties of GH make it an ideal candidate as the supporting matrix of a novel Si-graphene composite LIBs anode. But challenges remain with the even distribution of silicon active materials within such composite's matrix, as Si nanoparticles tend to agglomerate in the aqueous solution that is used for the synthesis of GH and negatively affects the electrochemical performance of the said anode. In this work, ultrathin SiO_x layer was formed on the surface of Si nanoparticles by ozone treatment, which is helpful to form the stable suspension with graphene oxide and the porous 3D GH composite embedded with SiO_x layer coated Si nanoparticles ($\text{Si@SiO}_x/\text{GH}$) has been synthesized successfully via a solution-based self-assembly process.

4.3 Experimental

4.3.1 Sample Preparation

The Si nanoparticles (~50nm, 99.9%, US Research Nanomaterials, Inc) were oxidized by ozone treatment at 100°C, 120°C, 150°C, and 200°C respectively with temperature ramp rate of 0.2°C min⁻¹. The samples are reacted in a fritted quartz U-tube and ozone generator was set at 10% set point with O² flowing (300mLmin⁻¹). The Si@SiO_x nanoparticles were obtained as a result of aforementioned process.

For the synthesis of Si@SiO_x/graphene hydrogel (Si@SiO_x/GH) composites, graphene oxide (GO) was first synthesized from flake graphite powder using a modified Hummers method in reported earlier publications[58, 83]. As in a typical procedure, Si@SiO_x nanoparticles (5-20 mg) were dispersed in 6ml of water/ethanol (1:2 vol. ratio) mixture solvent and sonicated for 1 hour. 4mL of GO suspension (5 mg mL⁻¹) was added and sonicated for 1hour to get stable suspension. 160 mg of L-Ascorbic acid (99%, Sigma Aldrich) was then added to the suspension, followed by 10 minutes of vigorous magnetic stirring until acid powders were completely dissolved. This mixture was then kept at 80°C for 24 hours to initiate pre-reduction and self-assembly process of GO in order to obtain a 3DSi@SiO_x/GH composite. The composite was taken out, washed repeatedly with distilled deionized (DDI) water and freeze-dried. Finally, the Si@SiO_x/GH composite was heated at 800 °C in a flow of Ar for 2 hour to further reduce GO.



Figure 4.1 Schematic illustration of procedure to synthesize Si@SiO_x/GH composites, with insert showing the digital images of the samples.

4.3.2 Sample Characterization

The transmission electron microscopy (TEM, JEOL-2100F) and high-resolution field emission scanning electron microscopy (FESEM, Hitachi SU8030) images were taken to characterize the morphologies and structures of the samples. Cycled electrode was disassembled from its coin cell and rinsed in dimethyl carbonate (DMC) in an argon-filled glovebox before characterization by FESEM. X-ray photoelectron spectroscopy (XPS) was conducted by Thermo Scientific ESCALAB 250Xi with X-ray source of Al K α (1486.6 eV). X-ray diffraction spectroscopy (XRD) was carried out by a Rigaku D/max 2550 V X-ray diffractometer using Cu-K α irradiation. Raman spectrum was measured on a T64000 triple Raman system with 514.5 nm Ar-ion laser as an excitation source. Thermogravimetric analysis (TGA) was recorded on a Netzsch TG 209 F1 Analyzer, from room temperature to 800°C with a ramp rate of 15 °C min⁻¹ and in lab air (15 mL min⁻¹).

4.3.3 Electrochemical Measurements

Electrochemical measurements were conducted using two-electrode CR2032 coin cells with lithium metal as the counter electrode at room temperature. The Si@SiO_x/GH composites were cut into a circular disc approx. 5 mm in diameter and used as working electrode, with Celgard 2400 film as separator. The electrolyte consisted of 1 M LiPF₆ in ethylene carbonate/dimethyl carbonate (EC/DMC 1:1 vol. ratio). Cell assembly was done in an argon-filled glove box (H₂O, O₂ < 1ppm). Galvanostatic cycling measurements were performed on BT2000 Potentiostat/Galvanostat system (Arbin Instruments) in the voltage range of 0.01-2 V vs Li⁺/Li. The current setting for cell tests and the specific capacity were calculated based on the total mass of Si@SiO_x/GH composites. Cyclic voltammogram (CV) and electrochemical impedance spectroscopy (EIS) were recorded by electrochemical workstation (Autolab PGSTAT128N). CV was tested at a scan rate of 0.1 mV s⁻¹ within 2-0.01V and EIS were tested under the following conditions: open potential of 0.5 V, AC voltage amplitude of 10 mV, and frequency range from 10⁶ to 0.01 Hz.

4.4 Results and Discussion

As prepared, the Si@SiO_x particles were 30-50 nm in diameter. The ozone treatment did not have observable effects on the morphology of the nanoparticles (Figure 4.7). Evident from the HRTEM (Figure 4.2) images, the Si nanoparticles were coated with a uniform layer of amorphous SiO_x, of which the thickness increased with increasing ozone treatment temperature, from 1.7 to 4.2 nm as the temperature increased from 100 to 200 °C. The fringes in the HRTEM image of the Si core (Figure 4.2d) showed an inter-planar spacing of 0.313 nm, which was consistent with the (111) planes of Si. The XPS Si 2p spectra (Figure 4.2e) showed the presence of three valence states of Si: Si4p (103.6 eV), Si2p (101.8 eV), and Si0 (99.8 eV) in these samples. The relative abundance of Si2p and Si4p increased with severity of ozone treatment, as expected, and Si0 remained the dominant species (Table 4.1).

The GH, with a 3D network of interconnecting micron-size pores, formed readily by heating a homogeneous mixture of GO and L-ascorbic acid at 80 °C for 8 h (Figure 4.8) [46]. The pores are open cells in nature, bounded by walls of ultrathin layers of stacked graphene sheets. The introduction of Si@SiO_x nanoparticles to the GH network did not change the morphology of the original GH structure (Figure 4.3), which was expected due the small volume of Si@SiO_x nanoparticles. The presence of Si@SiO_x in the composites was further confirmed through EDS.

The SEM images also showed that whereas some Si@SiO_x nanoparticles were evenly dispersed within the GH structure, others have agglomerated into micron-size clusters despite the presence of SiO_x coating (Figure 4.3 indicated by arrows). However, as the SiO_x coating thickness increased, the average size of agglomerates decreased, thereby improving the overall dispersion of the Si@SiO_x nanoparticles (Figure 4.3d and 4.9). It is noted that the changes to Si@SiO_x weight loading had minimal effects on the microstructure of composites (Figure 4.3e, f).

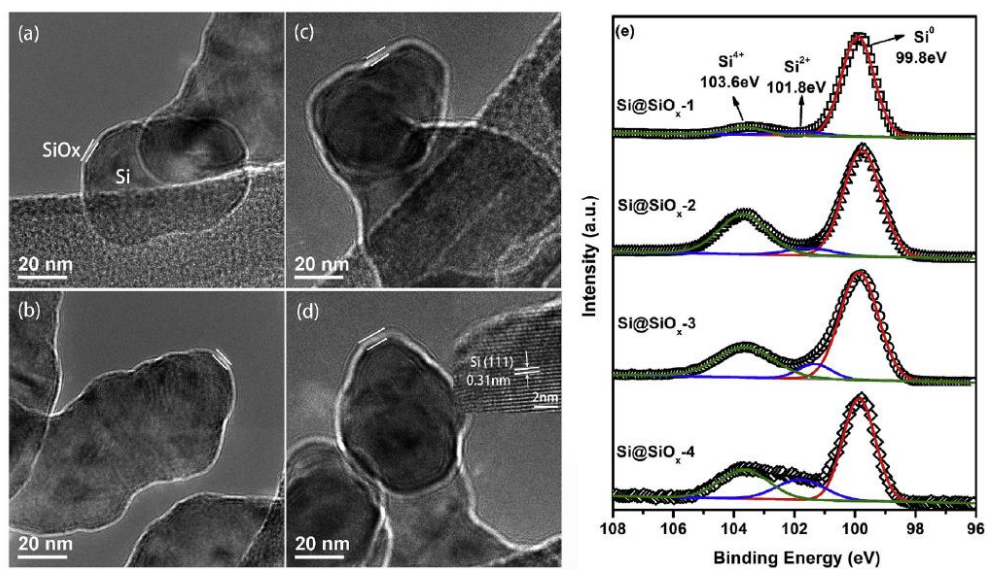


Figure 4.2 (a-d) TEM images of Si@SiO_x-1, -2, -3, -4 respectively with HRTEM image inserted, showing amorphous SiO_x layer of 1.3, 1.7, 2.4, and 4.2 nm, respectively; (e) high-resolution XPS spectra of Si 2p for the Si@SiO_x nanoparticles.

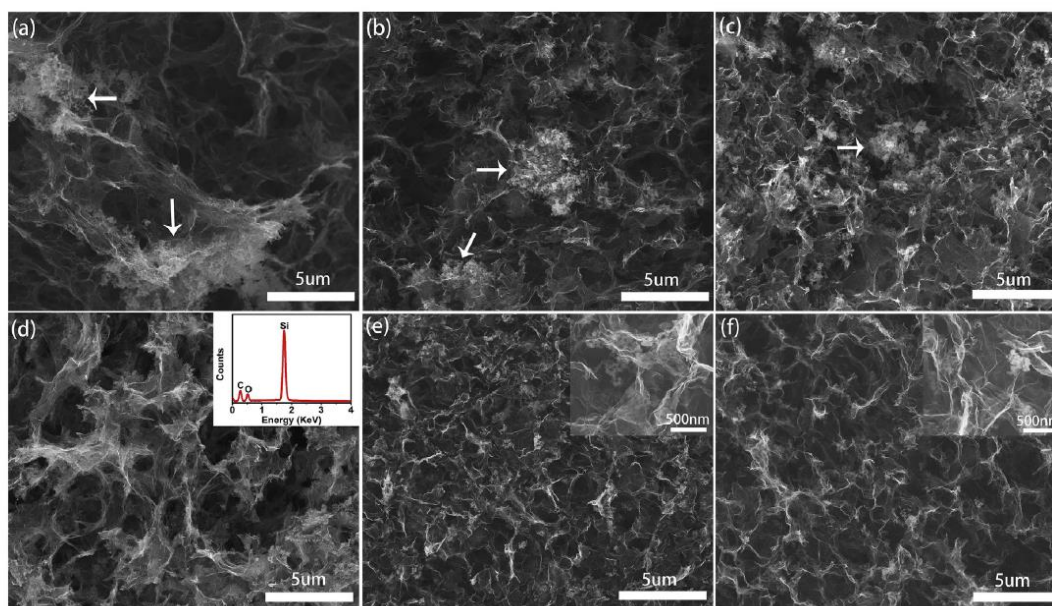


Figure 4.3 SEM images of Si@SiO_x/GH composite: (a) Si@SiO_x-1, (b) Si@SiO_x-2, (c) Si@SiO_x-3, (d) Si@SiO_x-4 (or named Si@SiO_x/GH-1) with insert showing the EDS spectrum, (e) Si@SiO_x/GH-2, and (f) Si@SiO_x/GH-3. Arrows indicate cluster of Si@SiO_x nanoparticles.

Samples	Si ⁰ content	Si ²⁺ content	Si ⁴⁺ content
Si@SiO _x -1	87%	5%	8%
Si@SiO _x -2	64%	6%	30%
Si@SiO _x -3	63%	8%	29%
Si@SiO _x -4	58%	17%	25%

Table 4.1 Abundance ratios of the different Si oxidation states present in the Si@SiO_x nanoparticles, calculated by curve fitting of the Si 2p spectra.

X-ray diffraction pattern of GO, Si@SiO_x-4, Si@SiO_x/GH-1 are compared in Figure 4.4a. For GO, a broad peak appeared at 12°, which corresponded to an interlayer spacing of 0.74 nm. This peak was no longer observable after reduction, and was replaced with another broader and

less intense peak at 25.8° , corresponding to that of graphite. This indicated successful reduction of GO to reduced graphene oxide (rGO) [47]. The patterns for Si@SiO_x-4 and Si@SiO_x/ GH-1 composite exhibited sharp diffraction peaks of crystalline Si, suggesting that the Si structure was preserved in the synthesis process. The patterns for all the Si@SiO_x/GH composites were similar, indicating consistency across all samples.

The Raman spectrum of Si@SiO_x/GH-1 (Figure 4.4b) showed a D band at 1332 cm^{-1} indicative of presence of disorder and a G band at 1594 cm^{-1} assigned to a strong tangential mode of the graphene structure. The spectra of all other composites were similar. The C1s XPS spectrum (Figure 4.4d) showed three peaks: two weak peaks at 286.3 eV and 287.5 eV, representing O-C-O/C-O and O-CO moiety respectively, and an intense peak at 284.8 eV, which represents the C/C moiety [37]. Thus, the reduction process removed most of the functional groups of GO. TGA in a flow of air resulted in complete loss of GH above 700°C but a small weight gain (<5%) for Si@SiO_x up to 800°C (Figure 4.4e). Thus, from the remaining weight after heating to $>700^\circ\text{C}$, the Si@SiO_x loading in samples Si@SiO_x/ GH-1, -2, and -3 were determined to be 71, 53, and 37 wt.%, respectively, and the densities of these three samples are 1.02, 0.618, and 0.4613 g cm^{-3} .

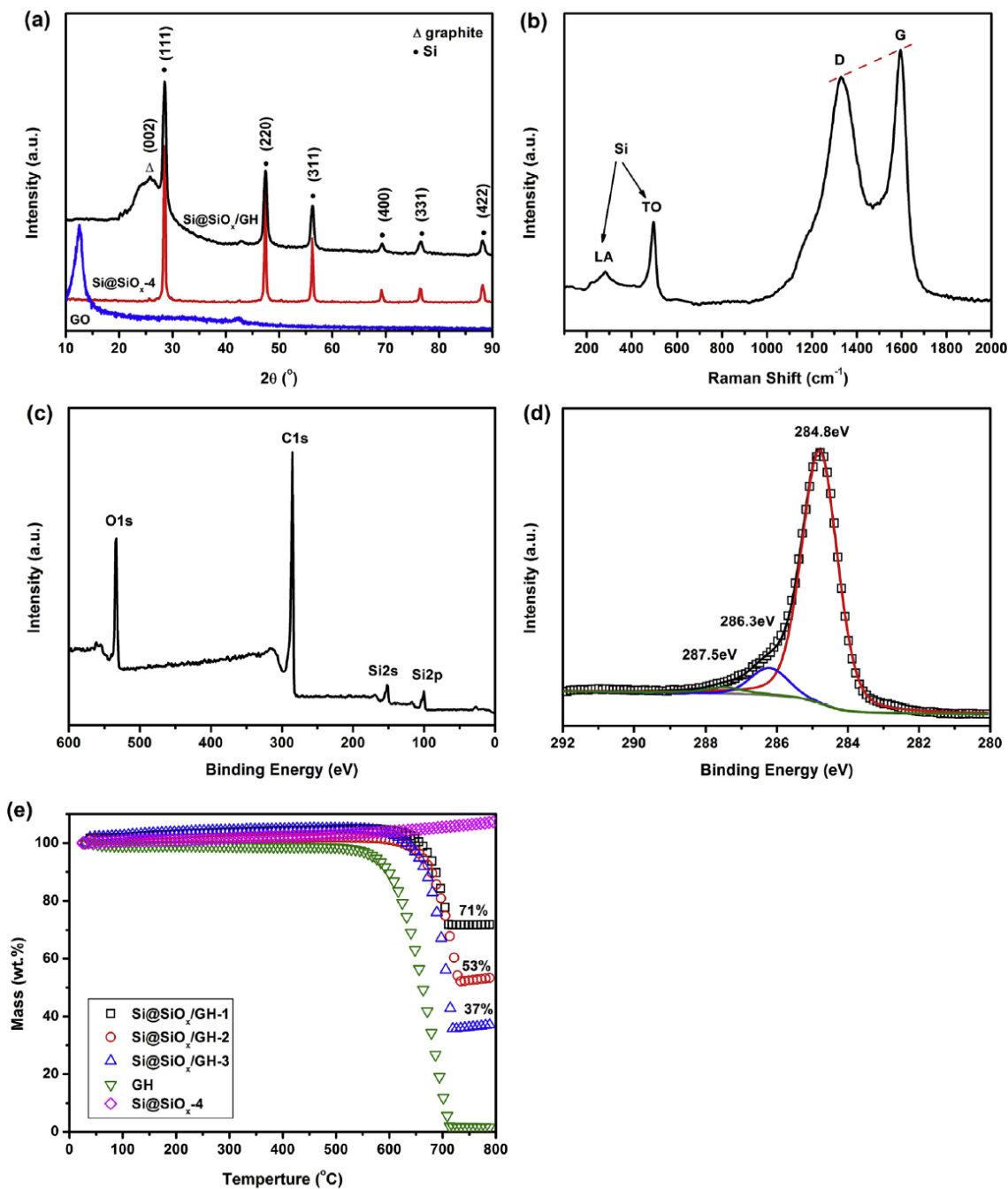


Figure 4.4 (a) XRD patterns of GO, Si@SiO_x-4, and Si@SiO_x-1; (b), (c), and (d) Raman spectrum, survey scan of XPS spectra, and high resolution C 1s XPS spectra of Si@SiO_x/GH-1, respectively; (e) TGA curves of Si@SiO_x/GH composites, GH, and Si@SiO_x-4.

The Li storage capacities of the Si@SiO_x/GH composite electrodes determined at different current densities (0.1, 0.5, 1, 2, and 4 A g⁻¹) are shown in Figure 5.5a and b. For the Si@SiO_x/GH-1, the first cycle coulombic efficiency was 53%. After 10 cycles, stable performance was reached. The initial capacity loss was mainly due to the formation of SEI film and stable products of Li with SiO_x during lithiation. The increase of Si@SiO_x loading had little effects on the cyclic stability, which showed that the porous 3D structure of GH could effectively accommodate drastic volumetric variation of Si@SiO_x during cycling, and minimize agglomeration of Si@SiO_x and detachment from the conducting GH matrix. The SiO_x coating could also serve to mitigate the formation of solid electrolyte interface (SEI) [43,48,49]. The stable capacities of Si@SiO_x/GH-1 were as high as 1640 mAh g⁻¹ at 0.1 A g⁻¹, and 1020 mAh g⁻¹ at 4 A g⁻¹. Compared to the capacity of 2080 mAh g⁻¹ at the end of the first 10 cycles at 0.1 A g⁻¹, the stable capacity at 50e140 cycles corresponded to 80% capacity retention. These values compared favorably with the reported values for Si@SiO_x/C (520 mAh g⁻¹ at 4 A g⁻¹ with 75wt.% Si@SiO_x) [29]. The relatively minor decrease in storage capacity as the current density increased reflected the consequence of the porous 3D structure, which provided abundance of lithium-ion diffusion channels that facilitated the rapid ion transport. The discharge-charge curves for Si@SiO_x/GH-1 (Figure 5.5b) showed the typical behavior of Si: the plateau below 0.25 V for the discharge curves and the gentle slopes that appeared between 0.3 and 0.6 V in the charge curves corresponded to the lithiation of Si and delithiation of Li_xSi phase, respectively. The increase of current density showed little effect on the shape of these curves.

The cyclic voltammograms (CV) profiles of Si@SiO_x/GH-1 composite electrode in the initial 5 cycles are shown in Figure 5.5c and for GH in Figure 4.11. In the first cycle, the cathodic peak at 0.74 V was attributed to the decomposition of electrolyte and the formation of SEI film

[50]. At about 0.01 V, a sharp reduction peak was observed due to the lithiation of Si and GH as well as further formation of SEI layer. In the following cycles, a much more prominent lithiation peak appeared at 0.15 V due to the formation of various Li-Si phases [51,52]. In the anodic scans, two apparent peaks at 0.35 and 0.5 V indicated the de-lithiation of Li-Si alloys [53].

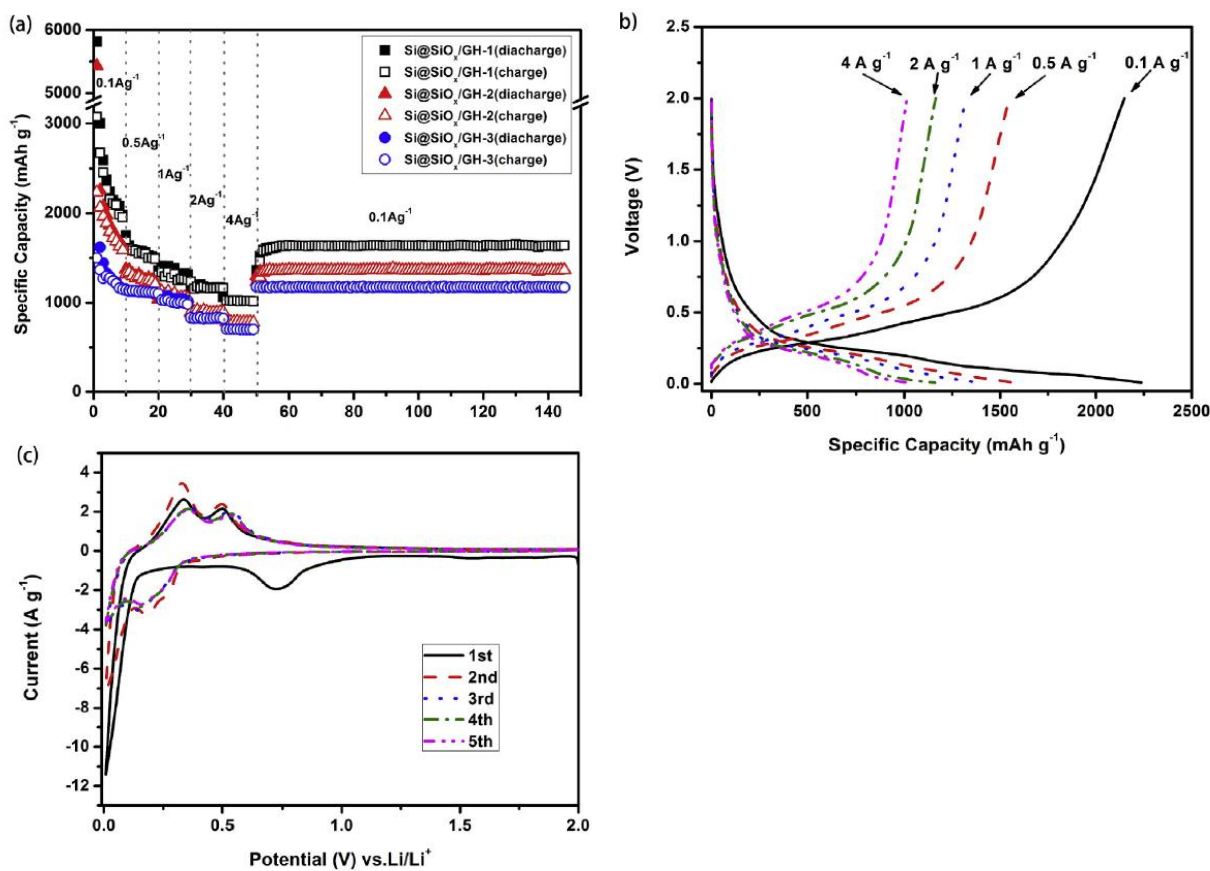


Figure 4.5 (a) Rate cycle performance of Si@SiO_x/GH composites and (b) galvanostatic charge-discharge profiles of Si@SiO_x/GH-1 at various current densities as marked; (c) Cyclic voltammograms of the Si@SiO_x/GH-1 in the initial five cycles at 0.1 mV/s. For Si@SiO_x/GH-1, 1 A g⁻¹ corresponded to about 12 mA cm⁻² for an active component of about 30 mg cm⁻².

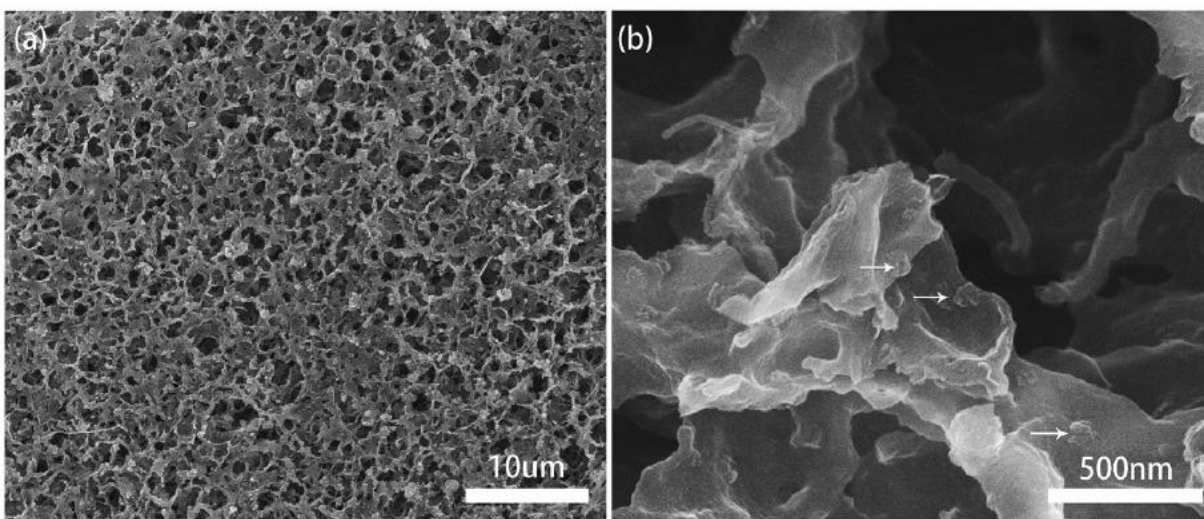


Figure 4.6 SEM images of Si@SiO_x/GH-1 anode after rate cycles test.

The structure and mechanical stability of Si@SiO_x/GH composite was further studied by post-cycling SEM images of Si@SiO_x/GH-1 electrode (Figure 4.6). Upon disassembly of the coin cell, the composite electrodes were found to retain its original porous 3D structure, despite being held in high compressive strain by the coin cell for 3 months. Under high-resolution SEM, Si@SiO_x particles show no sign of additional agglomeration post-cycling. Clearly, the 3D network structure and elasticity of GH were beneficial to the stability of Si@SiO_x nanoparticles during lithiation/de-lithiation, by accommodating the volumetric changes of Si nanoparticles while maintaining electrical connectivity between the nanoparticles and electrically conductive matrix of graphene hydrogel.

4.5 Conclusions

Porous 3D Si@SiO_x/GH composites were synthesized successfully and fabricated as anodes for LIBs. These composites, comprised of self-assembled 3D GH network with embedded Si nanoparticles coated with an ultrathin layer of SiO_x, were synthesized via a two-step solution-based process. These composites provided large specific surface areas for efficient loading of Si@SiO_x particles and accommodated volume changes of Si, while providing large amount of lithium-ion diffusion channels, fast electron transport kinetics, and excellent penetration of electrolyte solutions within their microstructure. Electrodes constructed with these composites showed outstanding rate capability (1020 mAh g⁻¹ at 4 A g⁻¹) and good cyclic stability (1640 mAh g⁻¹, 80% capacity retention between 10 and 140 cycles at 0.1 A g⁻¹). This study demonstrated an exciting pathway to the rational design and fabrication of 3D graphene matrix for application in LIBs and other electrochemical energy storage materials.

4.6 Acknowledgments

This work was supported in part by the Materials Research Science and Engineering Center (MRSEC) at Northwestern University, which is supported by the National Science Foundation under NSF Award Number DMR-1121262, by Northwestern University through the McCormick Catalyst Award and ISEN. Xuejun Bai was supported by a fellowship from the Chinese Scholarship Council. Assistance from the research groups of Prof. Jiaxing Huang and Prof. Samuel Stupp of Northwestern University for the CV tests was acknowledged.

4.7 Supplementary Data

Materials and Preparation Methods

1. Graphene oxide (GO) was synthesized from flake graphite (Asbury Carbons, 230U Grade, High Carbon Natural Graphite 99⁺) using a modified Hummers method[58, 83]. In a typical procedure, the graphite powder (2.0 g) was oxidized by stirring in a concentrated H₂SO₄ (20 mL) solution in which K₂S₂O₈ (1.0 g) and P₂O₅ (1.0 g) were completely dissolved at 80°C. The mixture, in a beaker, was kept at 80°C for 4.5 h using an oil bath. After the mixture was cooled and diluted with 1 L DDI (distilled deionized) water, the resulting solid was filtered with a Nylon membrane filter (47 mm diameter, 0.2 μm pore size, Millipore), and washed on the filter until the pH of the filtrate water became neutral. The shiny, dark-gray, oxidized graphite was dried in air overnight, and then dispersed by stirring in H₂SO₄ (75 mL) in an Erlenmeyer flask chilled in an ice bath. KMnO₄ (10 g) was added slowly with stirring to keep the temperature of reaction mixture below 20°C. The resulting thick, dark green paste was allowed to further react at 35°C for 2 h followed by addition of DDI water (160 mL) to form a dark brown suspension. To avoid overflow by foaming of the mixture due to rapid temperature rise during water addition, the flask was chilled in an ice bath and water was added in ~5 mL aliquots while monitoring the temperature closely. The temperature was kept below 50°C. After stirring for 2 more hours, the dark brownish suspension was diluted with DDI water (500 mL), and H₂O₂ (30%, 8.3 mL) was added slowly. The color of the mixture turned bright yellow. The mixture was allowed to settle overnight, then supernatant was decanted. HCl solution (10%, 800mL) was added and stirred for 3 hours. After the solution standing overnight, the supernatant was removed. The remaining product was repeatedly washed with DDI water and separated by centrifugation (20000 rpm for 1 h) until the

pH of the aliquot became neutral. Then, DDI water was added to the resulting product (GO) to make a ~0.5 % w/w aqueous suspension for storage.

2. Synthesis of graphene hydrogel (GH): 4mL of GO suspension (5 mg mL^{-1}) was added into 6ml of water/ethanol (1:2 v) mixture solvent and sonicated for 1h to get diluted and stable suspension. Then 160 mg of L-Ascorbic acid (99%, Sigma Aldrich) was added into the suspension with vigorous magnetic stirring for 10min until completely dissolving. This mixture was kept at 80°C for 24h without stirring to reduce GO and induce self-assembly process to obtain a 3D GH. Then the composite was taken out, washed repeatedly with distilled deionized (DDI) water and freeze-dried. Lastly, GH was heated at 800°C in a flow of Ar for 2 h for further reduction.

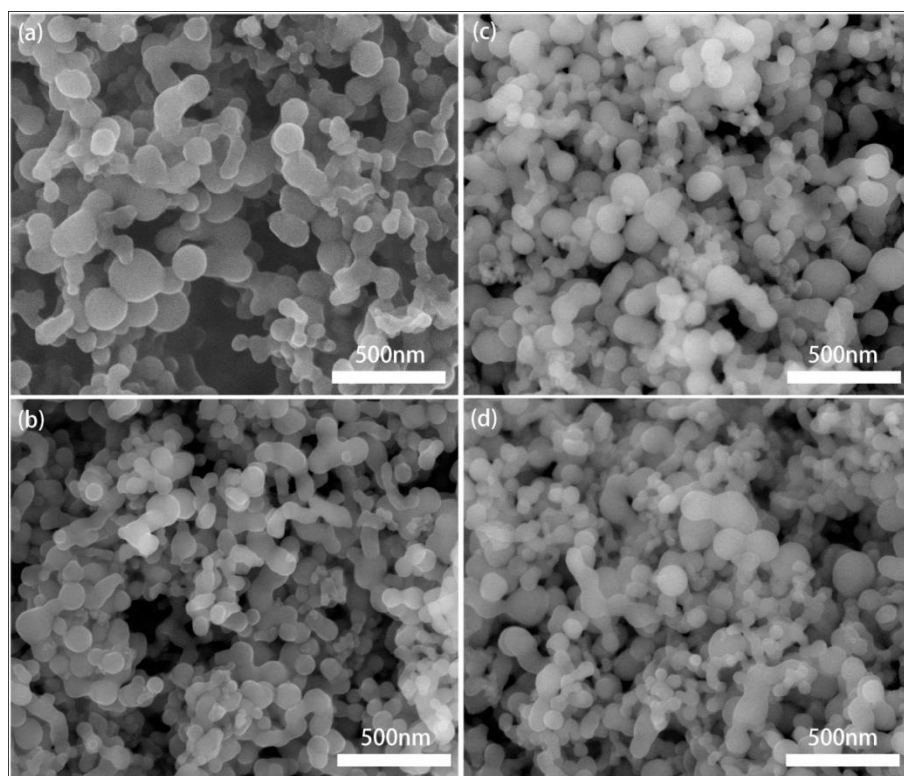


Figure 4.7 SEM images of Si@SiO_x particles: (a) Si@SiO_x-1, (b) Si@SiO_x-2, (c) Si@SiO_x-3, (d) Si@SiO_x-4.

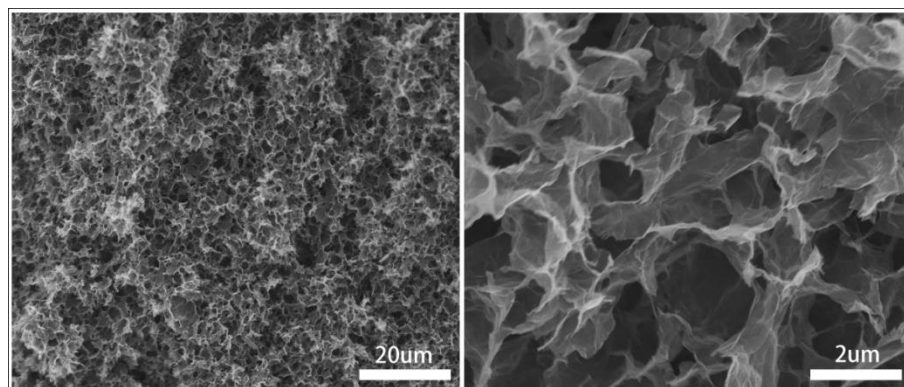


Figure 4.8 Low- and high-magnification SEM images of GH.

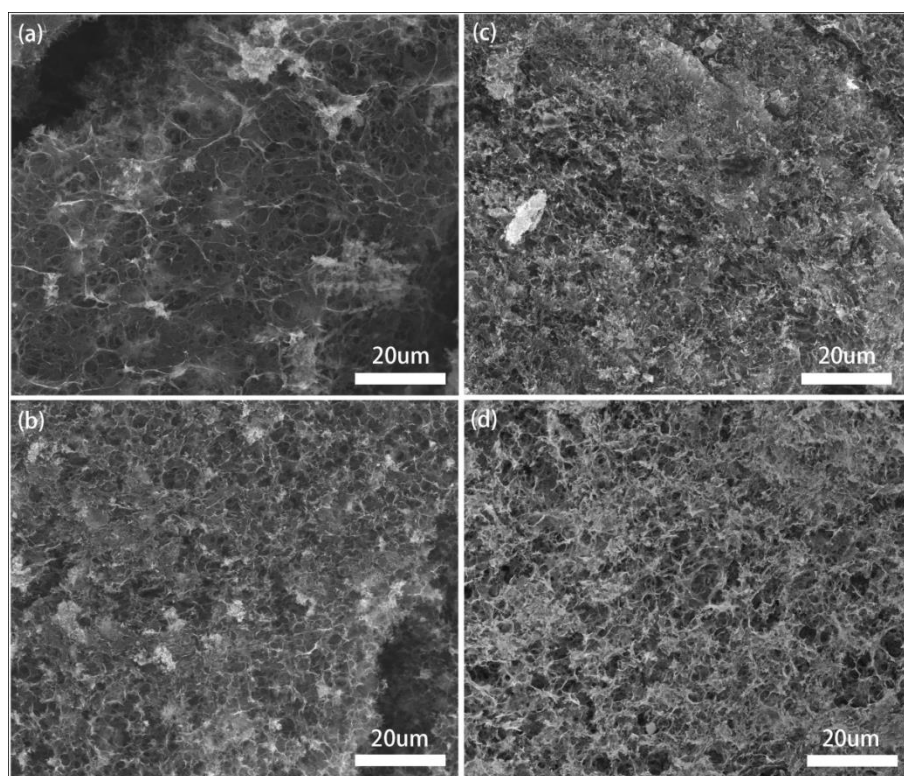


Figure 4.9 Low magnification SEM images of graphene hydrogel combined with Si@SiO_x particles: (a) Si@SiO_x-1, (b) Si@SiO_x-2, (c) Si@SiO_x-3, (d) Si@SiO_x-4.

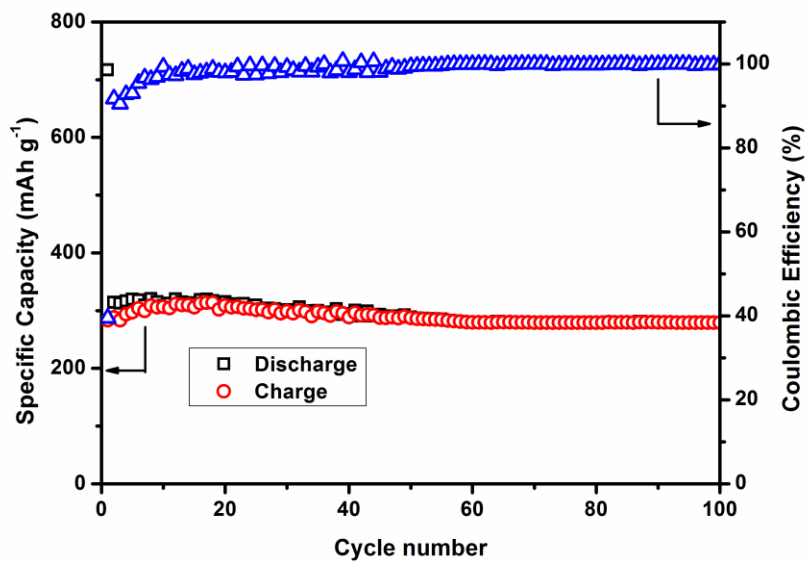


Figure 4.10 Cycling performances of GH anode at 100mA g^{-1} between 0.01 and 2.0 V.

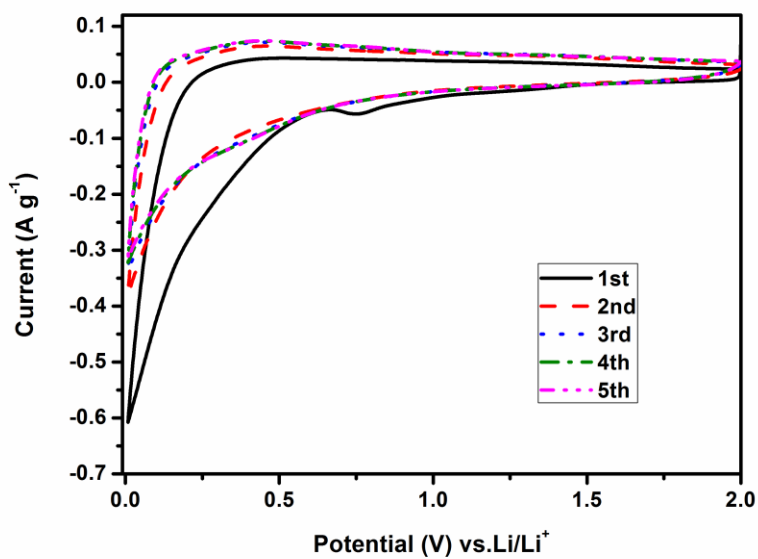


Figure 4.11 Cyclic voltammograms of the GH in the initial five cycles at 0.1mV/s and the voltage is between 0.01 and 2.0 V

CHAPTER 5

Electrochemical Properties of Reduced Graphene Oxide Thin Film on 3D Elastomeric Substrate

Adapted from Yue Yang Yu, Xue Jun Bai, Mayfair C. Kung, Yeguang Xue, Yonggang Huang, Denis T. Keane, Harold H. Kung, *Carbon*, 115 (2017) 380-387.

5.1 Abstract

Electrically conducting, 3D elastomeric composite foams are fabricated successfully using multiple cycles of infusing polyurethane foams with graphene oxide sheets followed by reduction, to form coatings of reduced graphene oxide up to 1260 nm thick. The reduced graphene oxide coating increases the compression modulus of the polyurethane foam and lowers the electrical resistance significantly, the extents of which increase with increasing coating thickness. The electrical resistance of the coated foams varies by as much as three orders of magnitude for coating thickness between ~150 and ~1200 nm, whereas the capacitance varies by one order of magnitude. Both the stress-strain and the resistance-strain behavior are highly repeatable with compression cycles performed up to 70% strain. Both SEM and X-ray tomography characterization show that deformation is mostly by bending of the pore walls up to about 20% strain, collapse of pore opening to about 60% strain, and densification beyond that. Micro-fractures also develop on the coating during the first few cycles of compression, but no obvious structural changes can be detected afterwards.

5.2 Introduction

Effective energy storage is critical for any mobile electronic device. For applications where the ability to withstand elastic deformation is essential, such as wearable electronics, surgical implants that naturally integrate with human functions, and systems with conformal formats, it is highly desirable that the energy storage components are stretchable, compressible, and bendable in all three dimensional axes. Electrodes are integral to any energy storage device. Thus, deformable electrically conducting materials that can be used to form electrodes will be critical enablers of high performance deformable electronic devices. The known approaches such as the use of metallized plastic and stretchable conducting material bonded onto elastomeric sheets and engineered into patterns,[84] such as waves,[85] mesh,[86, 87] and buckled configuration[88] are not easily amenable to forming three-dimensionally deformable material, especially deformation by compression. Other approaches include embedding carbon fiber, nanotube mats and crumpled sheets into an elastomeric matrix, and sandwiching them between elastomeric layers and forming 2D elastomeric electrodes.[89, 90] While excellent electrochemical performance has been reported for some of these 2-D designs, their applications are limited due to the limited degree of deformability. To obtain a higher degree of conformal flexibility and increase active material loading, the current 2-D electrodes have to be extended into freestanding 3-D configurations.

Electrically conducting graphene foams and carbon nanotube/graphene foams can be made compressible and elastomeric.[91-93] Since their electrical conductivity and mechanical properties both depend on the stacking of the graphene sheets and the nature (type, size) and density of defects of the sheets, they cannot be independently varied, and the material properties depend rather sensitively on the preparation procedure.

One approach to decouple the physical/mechanical and electrical properties is to form a composite of an elastomeric material, such as polyurethane that are highly deformable in three-dimensions, with an embedded electrically conducting network of, e.g. carbon nanotubes or graphene sheets. However, because of the vastly different elasticity between conducting carbon and the polyurethane, typically only a few weight percent of conducting carbon can be uniformly dispersed into the elastomer without significantly adversely affecting its mechanical properties. At such low loadings, it is difficult to achieve a highly conductive composite material. Thus, in spite of the relative ease of preparation and the advantage of 3D deformability, reported applications of these composites are currently limited to utilizing their dielectric[94, 95] and mechanical properties[96] for sensors[97] and actuators.[98, 99]

For the purpose of high electrical conductivity, stacking and overlapping of the conducting component that provides a continuous path is more desirable than distributing it uniformly within the elastomeric matrix. That is, it is desirable to coat the walls (both interior and exterior) of a porous elastomeric matrix with a conducting, electrochemically active layer than dispersing the conducting material in the matrix. Because the two phases are physically distinct in such a composite, their individual properties could be tuned independently to generate a highly conductive, electrochemically active, and deformable 3D material. Although there are a number of literature reports on such coated material using reduced graphene oxide (rGO) as the conductive phase and porous polyurethane (PU) foam as the elastomeric supporting matrix,[97, 100, 101] only two reports investigated the electrical conductivity that was found to be low.[102, 103] We conjectured that this could be because of the thickness of the rGO coating and/or the inherent low conductivity of the rGO layers due to insufficient reduction. Thus, by increasing the thickness and the degree of reduction of the rGO coating, we should be able to generate elastomeric materials of

higher electrical conductivity. In order to achieve this, a preparation procedure needs to be devised that is compatible with the hydrophobic rGO and the hydrophilic PU, while ensuring good adhesion between these two phases and maintaining electrical continuity of the conducting phase in the composite. Here we report our successful preparation of such a composite, its mechanical and electrical properties, and its application as an electric double layer capacitor electrode after subjecting it to severe deformation upon applied mechanical strain. The deformation led to the formation of surface defects that had not been observed previously in graphene-based 2-D electrode systems.

5.3 Experimental

5.3.1 Preparation of PU-rGO

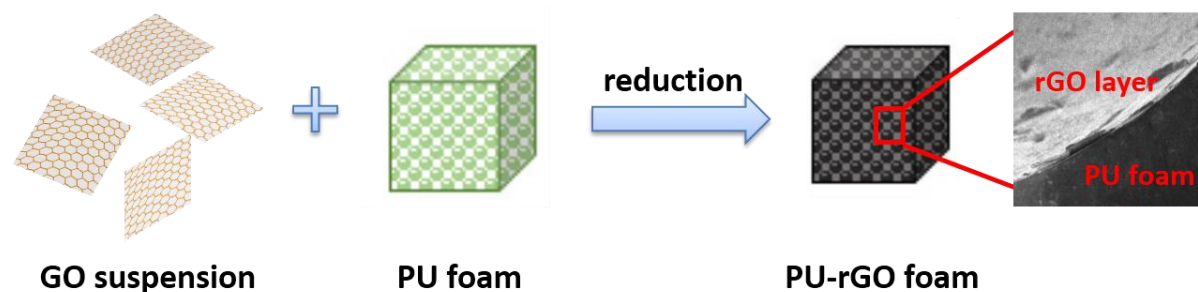


Figure 5.1 Scheme showing steps employed to form a PU-rGO foam sample.

Pieces of polyurethane (PU) foam, $2.5 \times 2.5 \times 2.5 \text{ cm}^3$, were cut from larger stock pieces obtained from BJB Enterprises (Tustin, CA, Type TC-266(50/100), IR spectrum shown in Figure S8) and used as received. An aqueous suspension of 0.5 wt.% graphene oxide (GO) was prepared using the modified Hummer's method as described previously²⁶, starting with flake graphite (Asbury Carbons, 230U Grade, High Carbon Natural Graphite 99⁺). The procedure used for the fabrication of elastomeric, electrically conductive, and electrochemically active composite is shown schematically in Figure 5.1. A piece of PU foam was submerged in 60 mL of the GO suspension for 2 h under high vacuum to remove trapped air within the porous structure. The soaked foam was removed carefully so as to retain as much of the absorbed liquid as possible, and then dried in vacuum overnight at 70 °C. The dried sample was placed on a stainless mesh screen above a 20 mL aqueous solution of ethylenediamine (1 mg mL^{-1} , Sigma Aldrich) in a sealed 40 mL Teflon autoclave vessel. The setup was then heated to 100°C for 4 h to initiate hydrothermal reduction of the GO coating. This coating process, from the initial vacuum dip-coating to the ethylenediamine-assisted hydrothermal reduction, could be repeated as many times as desired to obtain GO coatings of different thicknesses. After the desired number of coating cycles was

completed, the sample was then submerged in 60 mL 65 wt.% aqueous hydrazine monohydrate solution (Sigma Aldrich) for 3 h at 80 °C for further reduction to form the reduced graphene oxide (rGO) coating. The sample was then gently washed with distilled deionized water and then vacuum dried overnight at 80°C.

5.3.2 Characterization

Scanning electron microscopy images were collected with a high-resolution field emission scanning electron microscope (FESEM, Hitachi SU8030). In order to facilitate locating the interface for the rGO coating thickness measurement, some of the PU foams were first sputter-coated with a thin Pd metal film. Then the sample surface was ion-milled by FEI Helios Nanolab SEM/FIB to obtain a clear cross-sectional image of the PU bulk material with the rGO coating, the thickness of which was then measured digitally with an ImageJ software. No significant differences were detected with data collected from samples with and without Pd coating. X-ray photoelectron spectroscopy (XPS) was performed using a Thermo Scientific ESCALAB 250Xi (Al K α , 1486.6 eV). The stress-strain relationships were determined with a mechanical tester (MTS Sintech 20G), using a compression and rebound speed of 5 mm s⁻¹.

For electrical resistance measurements, aluminum foils serving as electrical contacts (Alfa Aesar, 0.025mm, 99.99%) were pasted with silver conducting paste onto two opposing faces of a PU-rGO foam piece to improve electrical contact. A voltage ramp from 0 to 3 V was applied across the current collectors using a potentiostat/galvanostat system (Arbin Instruments BT2000), which recorded the current passing through the foam piece.

Electrochemical tests of a foam piece were carried out in a three electrodes setup, with PU-rGO composite as the working electrode, Ag/AgCl (CH Instruments) as the reference electrode, and Pt foil (Alfa Aesar, 0.025mm, 99.9%) as the counter electrode. An aqueous solution of K₂SO₄

(0.5 M, Sigma Aldrich, 99% ACS) was the electrolyte. Using an electrochemical workstation (Autolab PGSTAT128N), current at densities of 0.05 A/g, 0.1A/g, and 0.5 A/g, based on the weight of the active materials in the foam pieces, was applied to charge and discharge the sample over a voltage range of -0.2 to 0.6 V. Cyclic voltammetry (CV) was performed with a scan rate of 5 to 100 mV s⁻¹ for a voltage scan of 0 to 1 V using a potentiostat/galvanostat system (Arbin Instrument BT2000).

5.4 Results and Discussion

The as-received PU foam had open, spherical, and interconnecting pores that averaged 500 μm in diameter (Figure 5.2a), that were packed tightly and separated by thin PU walls. The openings (necking) connecting adjacent pores were >100 μm in size on average. Three types of samples, with 1, 3, or 5 coatings of rGO, labeled PU-rGO-1, PU-rGO-3, and PU-rGO-5, respectively, were synthesized. Their weight % loadings of rGO materials were ~ 2 , ~ 5 , and ~ 7 , respectively and repeatable to within 15%, as determined by comparing the weights of pristine PU samples and PU-rGO samples after processing. PU-rGO-1 (Figure 5.2c, d) showed a thin coating of nonuniform thickness, PU-rGO-3 showed a more uniform coating ~ 600 nm thick (Figure 5.2e,f), and PU-rGO-5 showed a rather rough coating ~ 1200 nm thick with evidence of some loosely bound rGO flakes on the surface (Figure 5.2g,h).

Subjecting the PU substrate through the preparation procedure of reduction, washing and heating but without GO did not change the PU, as shown by SEM, FIB, and X-ray tomography measurements (Figure 5.10, 5.13, 5.14, and 5.17). The PU substrate also retained its original open pore structure after deposition and reduction of GO/rGO coatings (Figure 5.2c, e, g), with minimal clogging of the open PU pores. The rGO coatings on all samples adhered well to the PU and showed no obvious signs of delamination even after repeated high-strain compression.

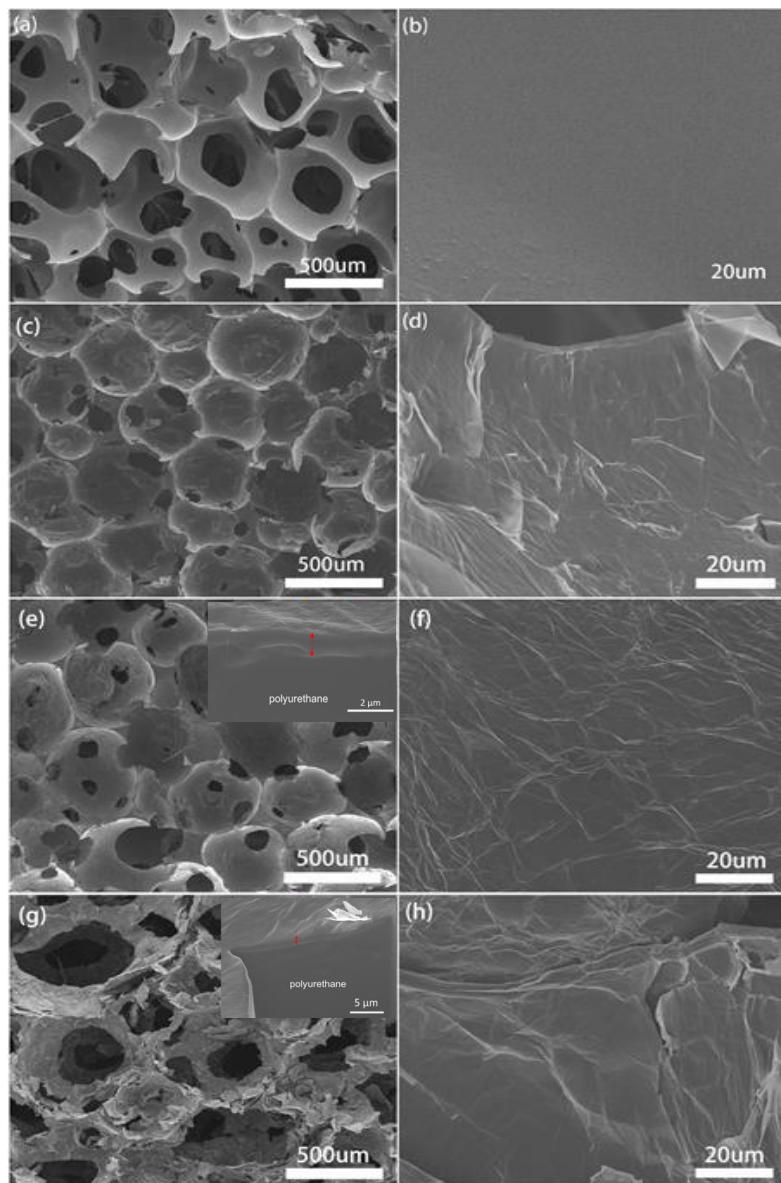


Figure 5.2 SEM images of: (a, b) pristine PU foam; (c, d) PU-rGO-1; (e, f) PU-rGO-3; inset in e is cross-sectional image obtained using FIB, with the rGO layer highlighted by arrows. From additional images (Figure S1), the thickness was estimated to be 570 ± 185 nm; and (g, h) PU-rGO-5; inset in g is cross-sectional image with rGO layer highlighted, and the thickness was estimated to be 1260 ± 220 nm (Figure S2).

The chemical composition of the rGO coatings after the two-step reduction were investigated with XPS. The intensity of oxygen containing C=O (286.8 eV) and, more significantly, C-O (284.7 eV) peaks were reduced after the two-step ethylenediamine and hydrazine reduction processing (Figure 5.3a, b, c). This results higher C/O atomic ratios were detected on samples after the said reduction processing, with the ratio jumping from 1.88:1 for unreduced rGO thin film to 6.5:1 and 6.2:1 for single and five times coated PUrGO samples, respectively. As expected, ethylenediamine-assisted hydrothermal reduction, by itself, cannot fully reduce the rGO content in the PUrGO composite, as indicated high C-O peaks and low C/O ratio of 2.2:1 in Figure 5.3d. Low amount of nitrogen doping was also detected in PU-rGO samples that were hydrothermally reduced with ethylenediamine and hydrazine (Figure 5.12).

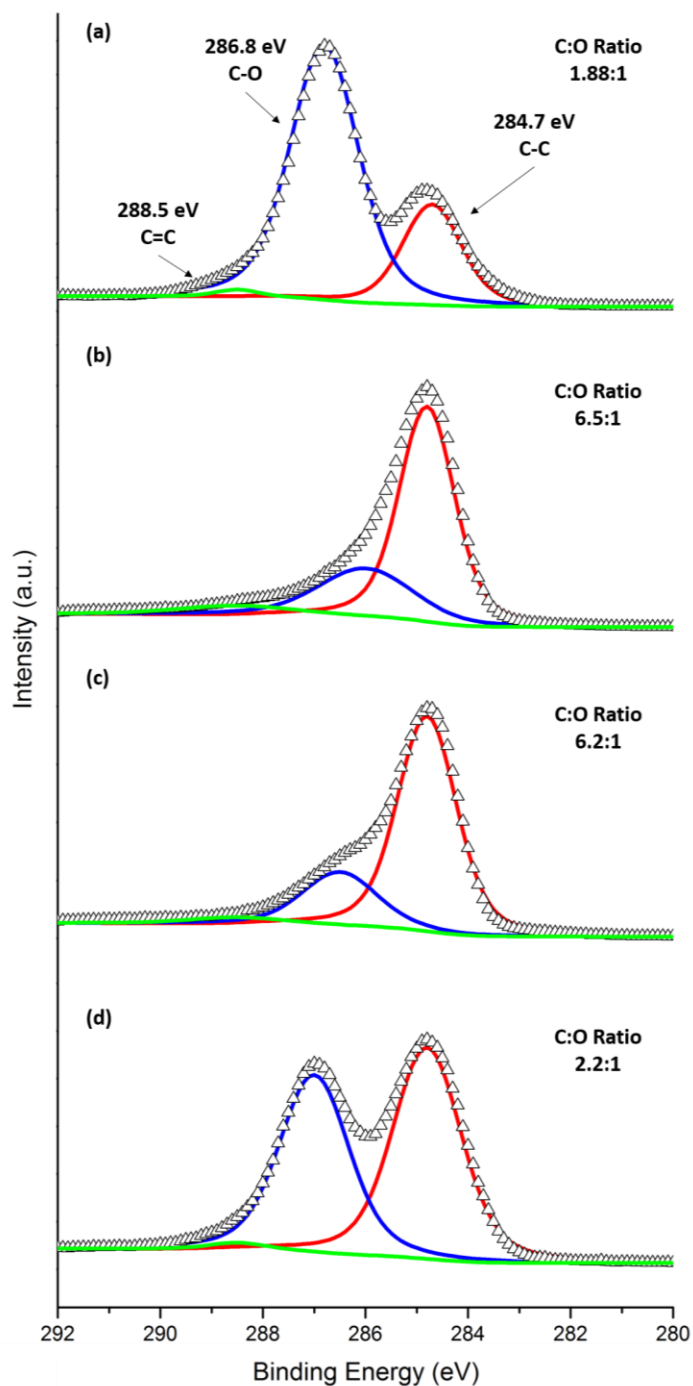


Figure 5.3 High-resolution XPS C1s spectra of (a) untreated rGO thin film, (b) PU-rGO-1 single coated and (c) PU-rGO-5 five times coated composite samples after ethylenediamine and hydrazine hydrothermal reduction, and (d) PU-rGO-1 single coated composite sample after only ethylenediamine hydrothermal reduction.

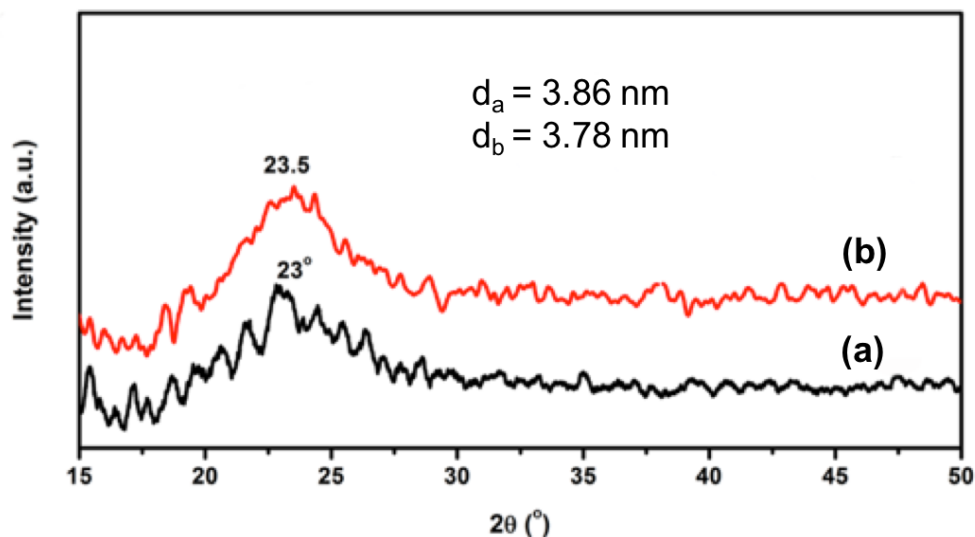


Figure 5.4 XRD patterns of sample (a) PU-rGO-1 single coated composite sample after only ethylenediamine hydrothermal reduction, (b) PU-rGO-1 single coated composite sample after ethylenediamine and hydrazine hydrothermal reduction.

In order to obtain interlayer spacing between rGO sheets in the coating, a piece of rGO coating on the external surface of a PU foam was removed using Scotch tape. XRD patterns of the coating (Figure 5.4) indicated that the interlayer stacking separation was smaller for the sample reduced with the two step hydrothermal reduction in comparison to the same sample that only underwent ethylenediamine assisted reduction.

Structural deformation of the PU-rGO composites under compression was investigated by SEM, and the data for PU-rGO-3 foam are shown in Figure 5.5. Up to about 20% strain, the deformation was mostly due to bending of the pore walls (Figure 5.5a-c). This corresponded to the linear region in the S-S curve in Figure 5.15. Between 20-60% strain (Figure 5.5d-f), collapse of pore openings began to occur, which corresponded to the plateau (or more gently sloping) region in the S-S curve. At high strain (>60%) (Figure 5.5g, h), the composite underwent densification

and began to exhibit a modulus approaching that of solid bulk material. These structural changes were similar to those observed based on reconstructed 3D images from X-ray tomography (Figure 5.17), and consistent with literature findings on the deformation mode of porous polyurethane foam.²³ Importantly, there was no obvious detachment of rGO coating from the PU matrix throughout the cycling process.

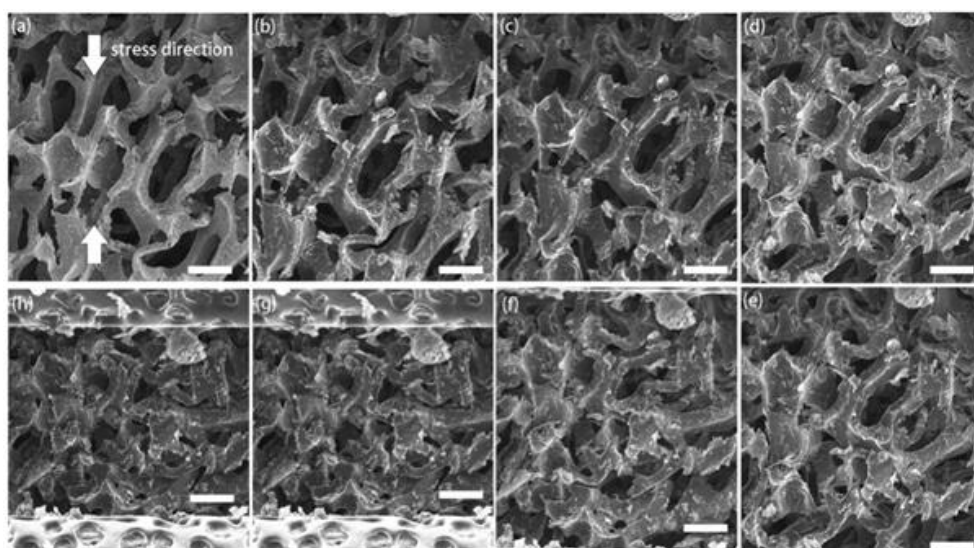


Figure 5.5 SEM images of PU-rGO-3 foam at different compressive strain (vertical compression): (a) 0%, (b) 10%, (c) 20%, (d) 30%, (e) 40%, (f) 50%, (g) 60%, and (h) 70%. The scale bar is 300 μ m.

The electrical conductivities of the composite samples were determined from I-V scans at different compressive strains. In all cases, the current across the foam increased linearly as the applied voltage increased, as exemplified by the behavior of PU-rGO-3 (Figure. 5.18). Figure 5a shows the resistance of PU-rGO-3 at various levels of strain up to 70% during repeated cyclic deformation. The overall resistance of the sample stabilized after first few (~10) cycles of

deformation when loose pieces of rGO fell off. Figure 5.6b shows the dependence of resistance on coating thickness. PU-rGO-1 with the thinnest coating exhibited the highest resistance, ~ 20 k Ω , three orders of magnitude larger than the other samples. The resistance dropped markedly to ~ 65 – ~ 470 Ω for PU-rGO-3 and ~ 20 – ~ 140 Ω for PU-rGO-5. All three samples exhibited decreasing resistance with increasing compressive strain. As shown in the SEM (Figure 5.5) and X-ray tomography images (Figure 5.17), compression led to gradual closing of the open pores, which in turn generated new electrically conductive pathways and lower resistance. Although these resistance values were slightly higher than those of graphene or graphene-CNT only electrodes,^{22,25} which is expected as the majority of the composite is consisted of the insulating PU, the relatively low resistance of these composite foam suggested very efficient use of the graphene.

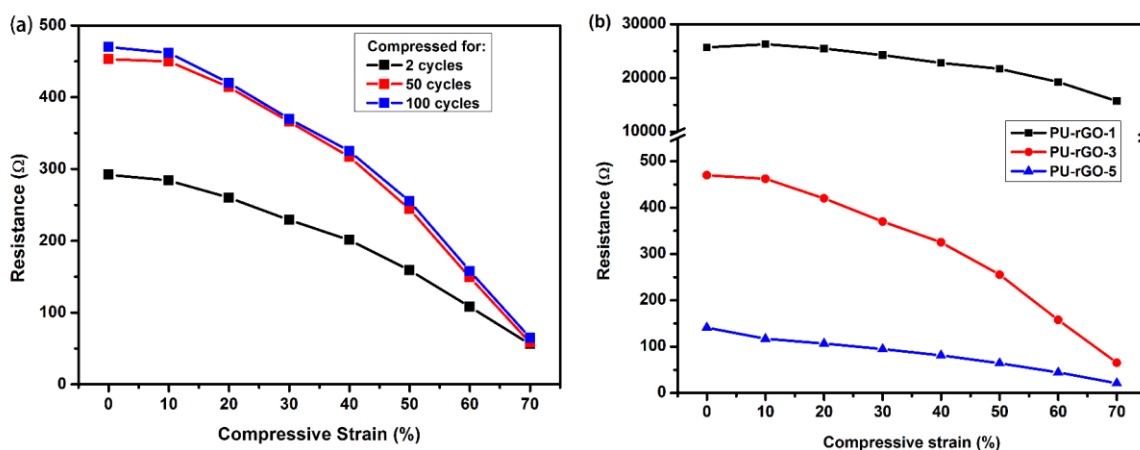


Figure 5.6 (a) Resistance of a PU-rGO-3 foam at different compressive strain after 2, 50, and 100 repeated cycles of compression; (b) Resistance of PU-rGO-1,3,5 samples as a function of applied compressive strain after 100th cycle of compression.

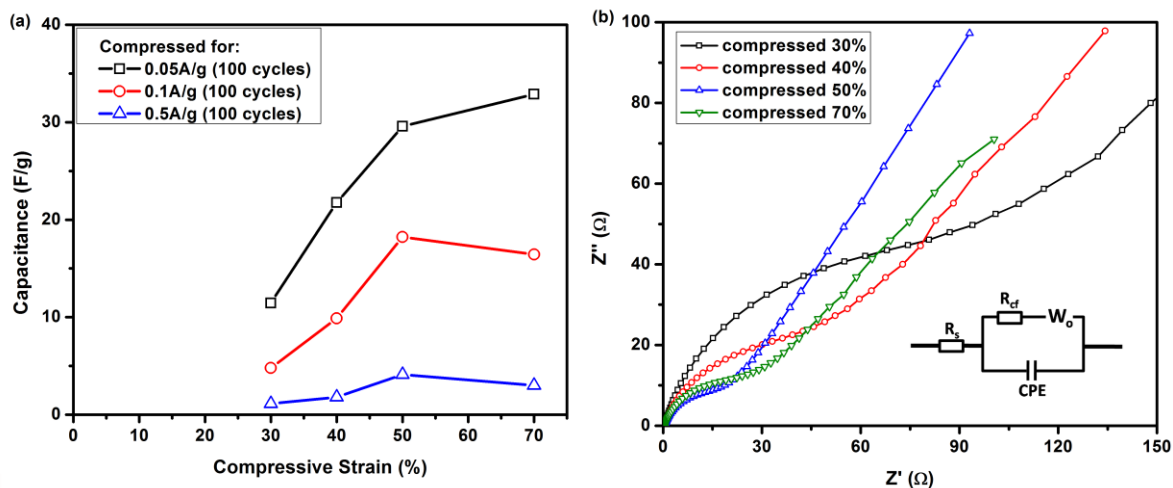


Figure 5.7 (a) Capacitance of a PU-rGO-5 foam electrode as a function of compressive strain; (b) Its EIS data at corresponding compressive strain, with illustration of equivalent circuit used for obtaining the fitted resistance values.

The capacitance and impedance of PU-rGO-5 were measured as a function of compressive strain (Figure 5.7). The impedance data were fitted with the equivalent circuit shown in the figure. The resulting series resistance (R_s), which corresponded the sum of the resistances from electrode-Pt contact, the bulk electrolyte, and the electrode material, decreased with increasing compressive strain (Table 5.1). This was expected based on the behavior of the electrical resistance with compression shown earlier. The charge transfer resistance (R_{ct}), which represented movement of charges within the Helmholtz double layer and charge transfer at functional groups of the rGO surface, decreased significantly from 30 to 50% strain and then increased again at higher strain. Such behavior was observed in capacitance as well. At the higher current densities of 0.1 A/g and 0.05 A/g, the capacitance increased from between 30% and 50% strain, then decreased at 70% strain. At a low current density of 0.05 A/g, the decrease at 70% strain was replaced by a slight

increase. These electromechanical behaviors were reproducible even after many compression cycles.

Strain	R_s (Ω)	R_{ct} (Ω)
30%	0.458	70.85
40%	0.440	19.07
50%	0.437	8.94
70%	0.431	23.02

Table 5.1 EIS fitting results of PU-rGO-5.

There were two major contributing structural factors to the observed electromechanical behavior. One was closing of the open pores as described earlier, the other was creation of open facial micro-fractures under high strain. As shown in Figure 5.8, in the first few compression cycles, the tension on the stretched surface of a bent pore walls of the macroporous PU under compression led to the creation of facial-micro-fractures on the rGO coating, which was evident in the SEM images. In later cycles after these fractures were developed, compression up to about 50% strain opened the fracture, and the exposed rGO edge planes provided added exposed surfaces to allow infiltration of electrolyte into the interlayer spacing between stacked graphene sheets, which resulted in the increased capacitance. When the strain was released, closing of the micro-fracture opening decreased the interfacial area, returning the sample closer to its original state, and the capacitance decreased. At higher strain than 50%, closing of macropores that decreased the exposed interfacial area began to contribute significantly. At high current when rate of ion transport limited participation of very small cracks, pore closing dominated the capacitance

behavior, and a decrease in capacitance and an increase in R_{ct} were observed. At low currents, where influence of ion transport was less prominent, the capacitance continued to increase but at a reduced rate.

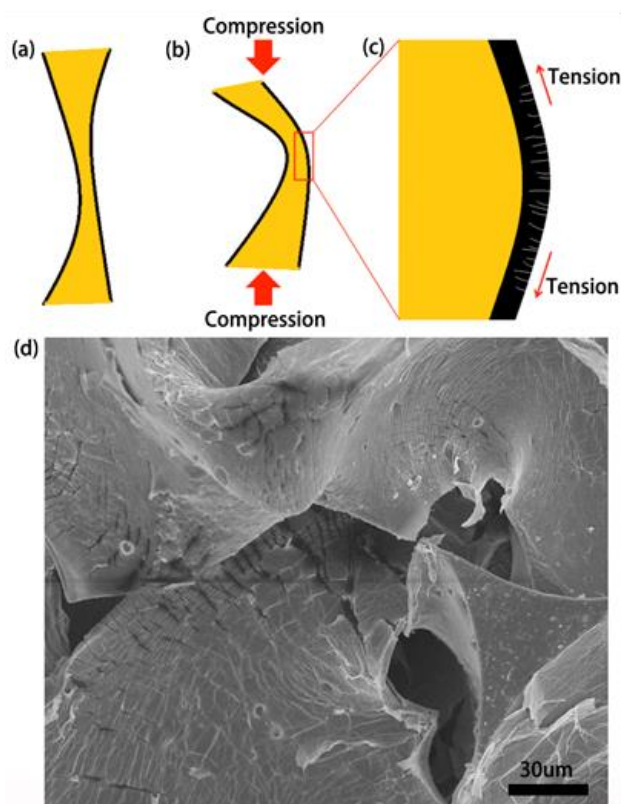


Figure 5.8 (a) Schematic cross-sectional diagrams of a coating of stacked graphene layers (black) on a PU substrate (yellow) and (b and c) after bending due to compression, showing tension-induced formation of micro-fracture. (d) SEM image of PU-rGO-3 under 70% compression strain, exhibiting facial micro-cracks of the rGO coating.

5.5 Conclusion

A 3D, porous, electrically conducting elastomeric composite foam was successfully fabricated that was suitable for use as flexible electrical conductors and electrodes for electrical energy storage devices. The material, consisting of an elastomeric PU foam coated with a conducting layer of rGO, was highly durable to repeated compression cycling. Good adhesion between the rGO coating and the supporting PU matrix resulted in highly repeatable behavior even though micro-fractures were formed by compression at high strain, suggesting the beneficial effect of decoupling the component for electrochemical properties from the component for mechanical properties.

5.5 Acknowledgements

This work was supported in part by the Materials Research Science and Engineering Center (MRSEC) at Northwestern University, which is supported by the National Science Foundation under NSF Award Number DMR-1121262, by Northwestern University through the McCormick Catalyst Award and ISEN. Xuejun Bai was supported by a fellowship from the Chinese Scholarship Council. Assistance from the research group of Prof. Samuel Stupp of Northwestern University for the capacitance and EIS tests was acknowledged. We also thank Garrett Chinyu Lau (NU), Dr. Yuanlong Shao (Donghua University), and Dr. Mark E Seniw (CLaMMP, NU) for helpful discussions.

5.6 Supplementary Data

Fourier Transform Infrared Spectroscopy

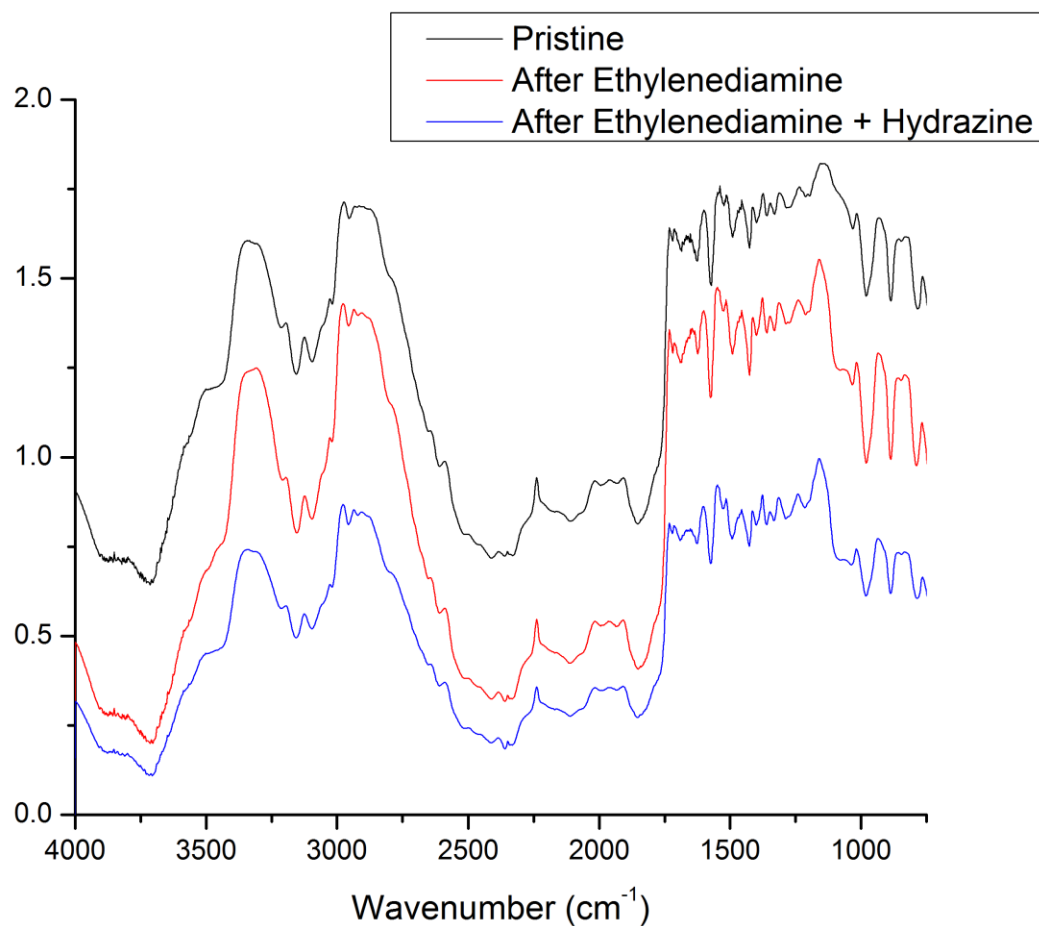


Figure 5.9 FTIR spectra of polyurethane foam in as received condition, after 4 hours of hydrothermal treatment at 100 °C with ethylenediamine, and same sample as after additional 3 hours of submersion in 65 wt.% hydrazine monohydrate solution at 80 °C.

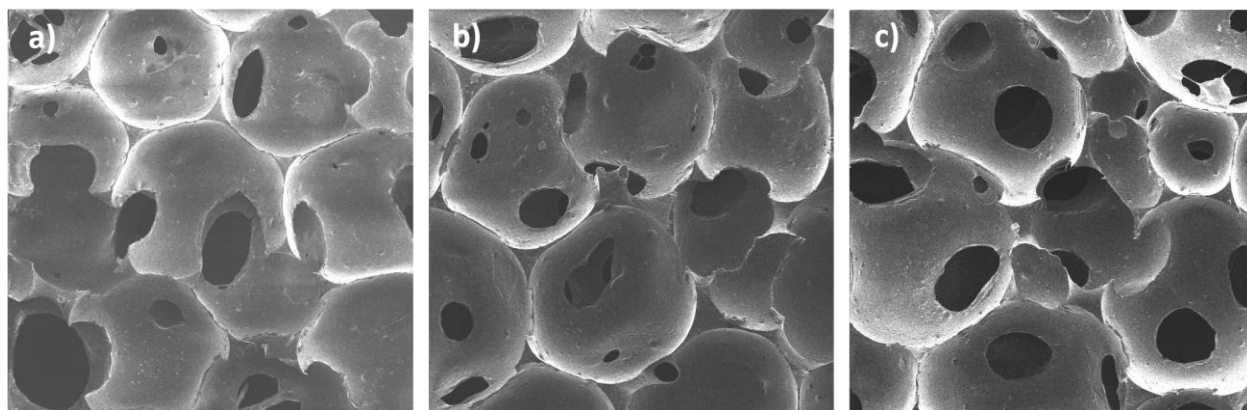


Figure 5.10 SEM images of (a) as received PU foam, (b) PU foam after 4 hours of hydrothermal treatment at 100 °C with ethylenediamine, (c) same sample as (b) after 3 hours of submersion in 65 wt.% hydrazine monohydrate solution at 80 °C.

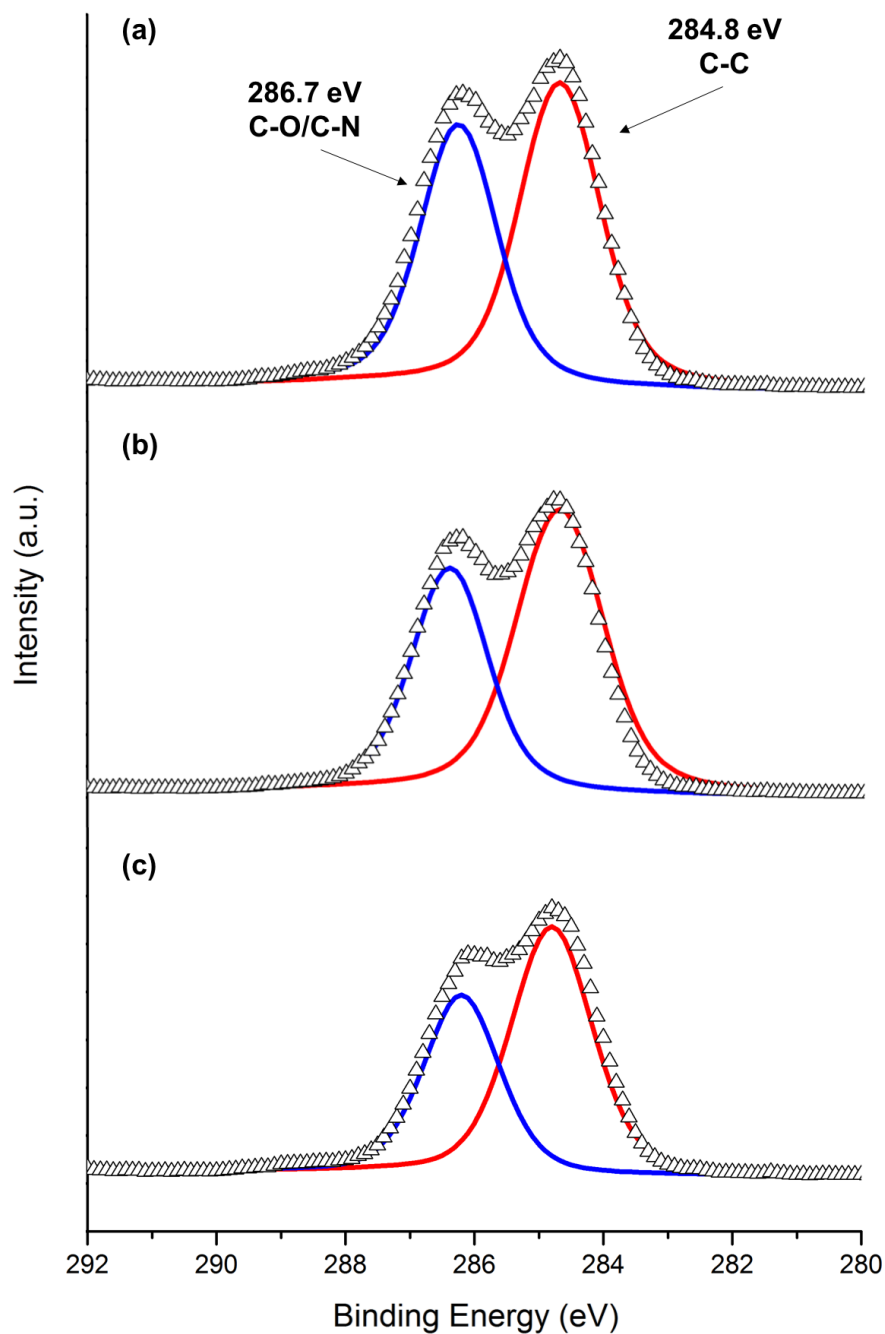


Figure 5.11 XPS C1s spectra of (a) as received PU, (b) PU foam after 4 hours of hydrothermal treatment at 100 °C with ethylenediamine, (c) same sample as (b) after additional 3 hours of submersion in 65 wt.% hydrazine monohydrate solution at 80 °C.

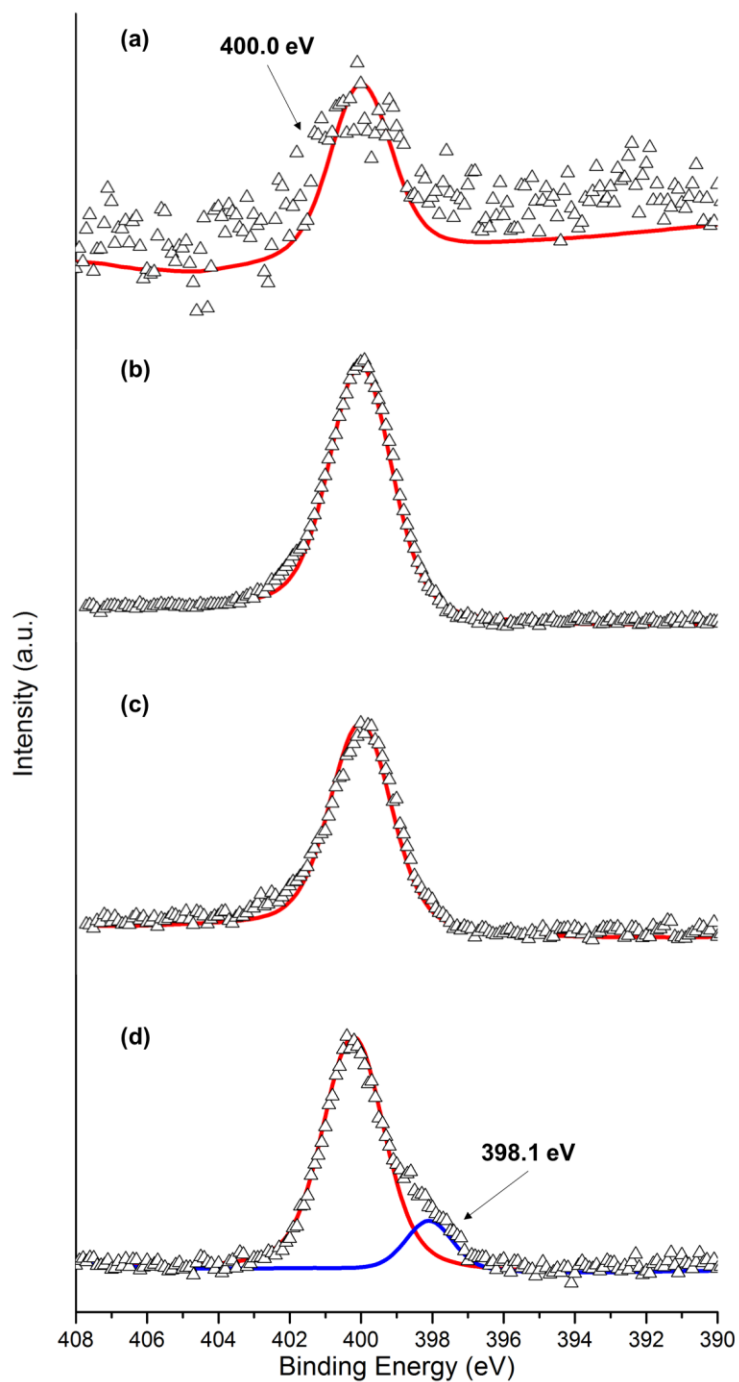


Figure 5.12 XPS N1s spectra of (a) untreated rGO thin film, (b) PU-rGO-1 single coated and (c) PU-rGO-5 five times coated composite samples after ethylenediamine and hydrazine hydrothermal

reduction, and (d) PU-rGO-1 single coated composite sample after only ethylenediamine hydrothermal reduction.

Focused Ion Beam Thickness Measurement

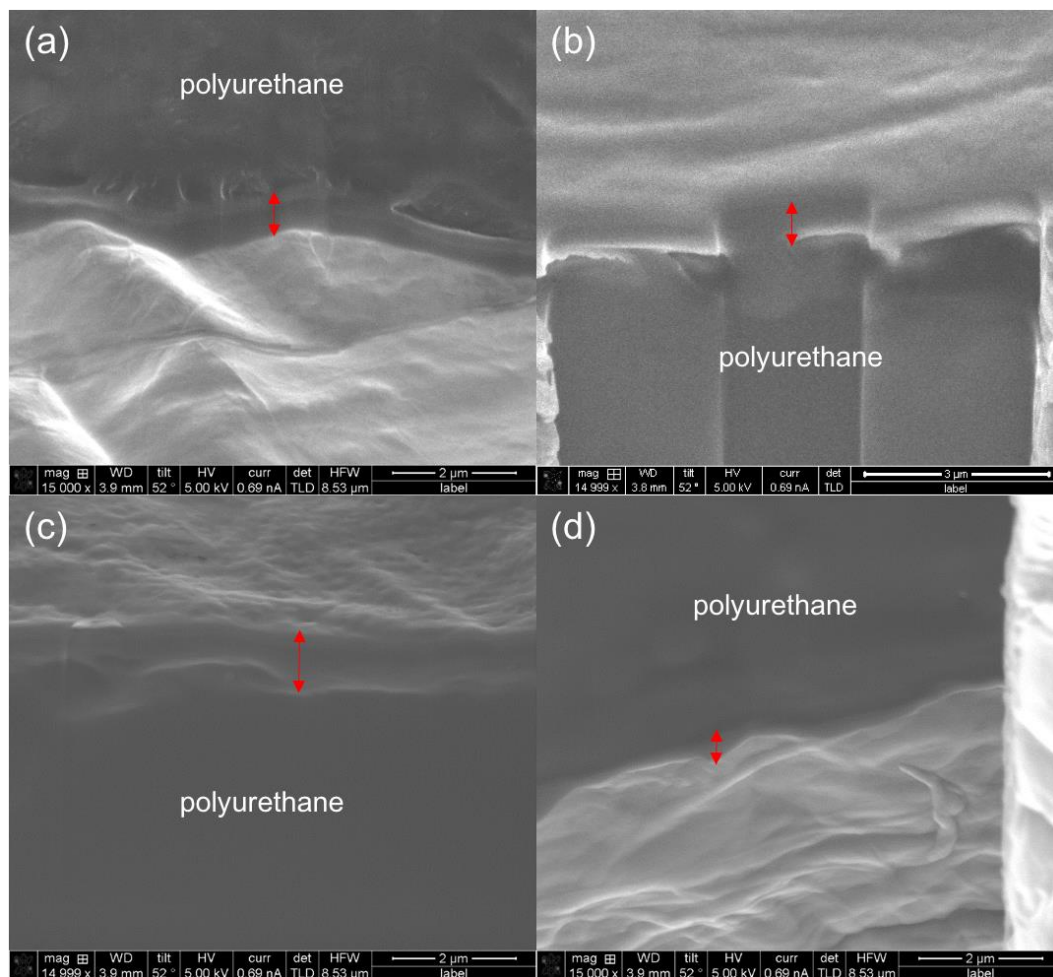


Figure 5.13 SEM images of FIB milled PU-rGO-3 at 4 separate regions. No Pd coating was applied for these samples. The thickness of the rGO was measured every μm for all four images to arrive an average of 570 nm, with a standard deviation of 185 nm.

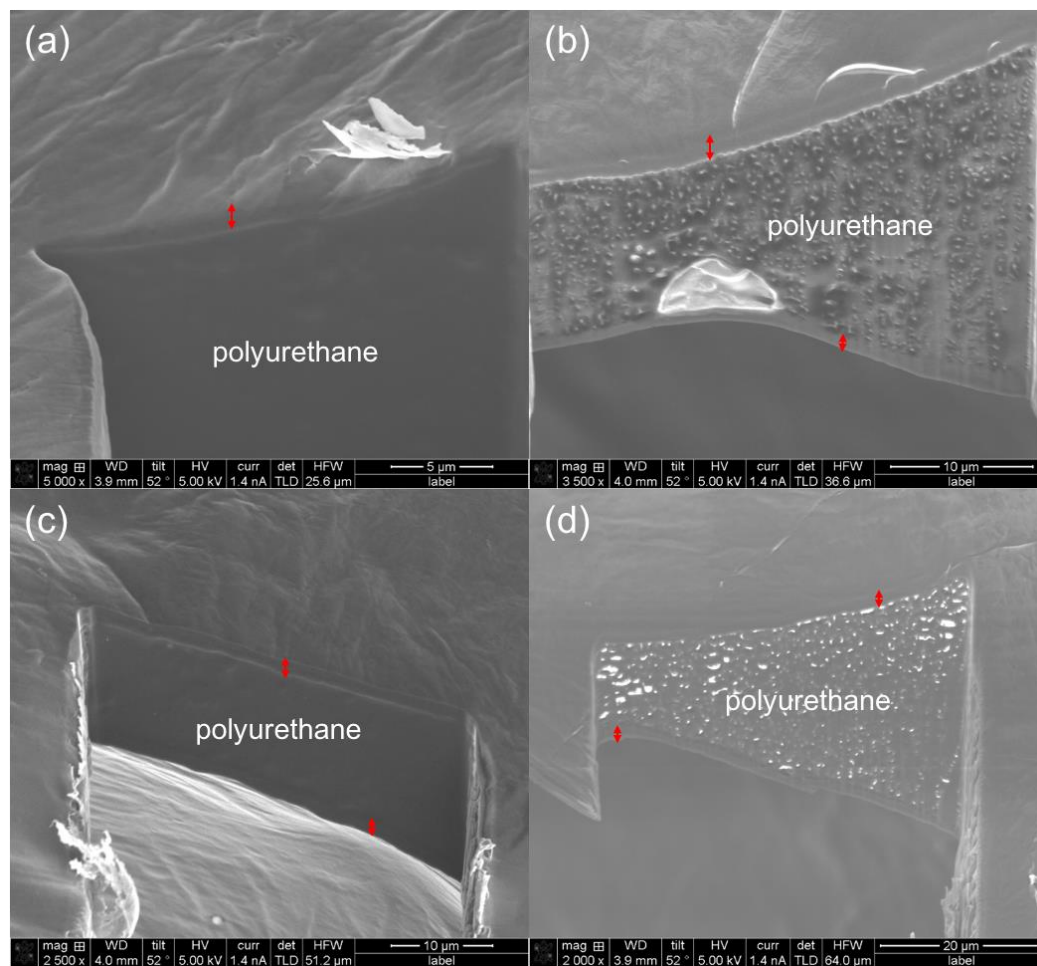


Figure 5.14 FIB milled SEM images of PU-rGO-5 at 4 individual regions. No Pd coating was applied to these samples. The thickness of the rGO was measured every μm for all four images to arrive an average of 1260 nm, with standard deviation of 220 nm.

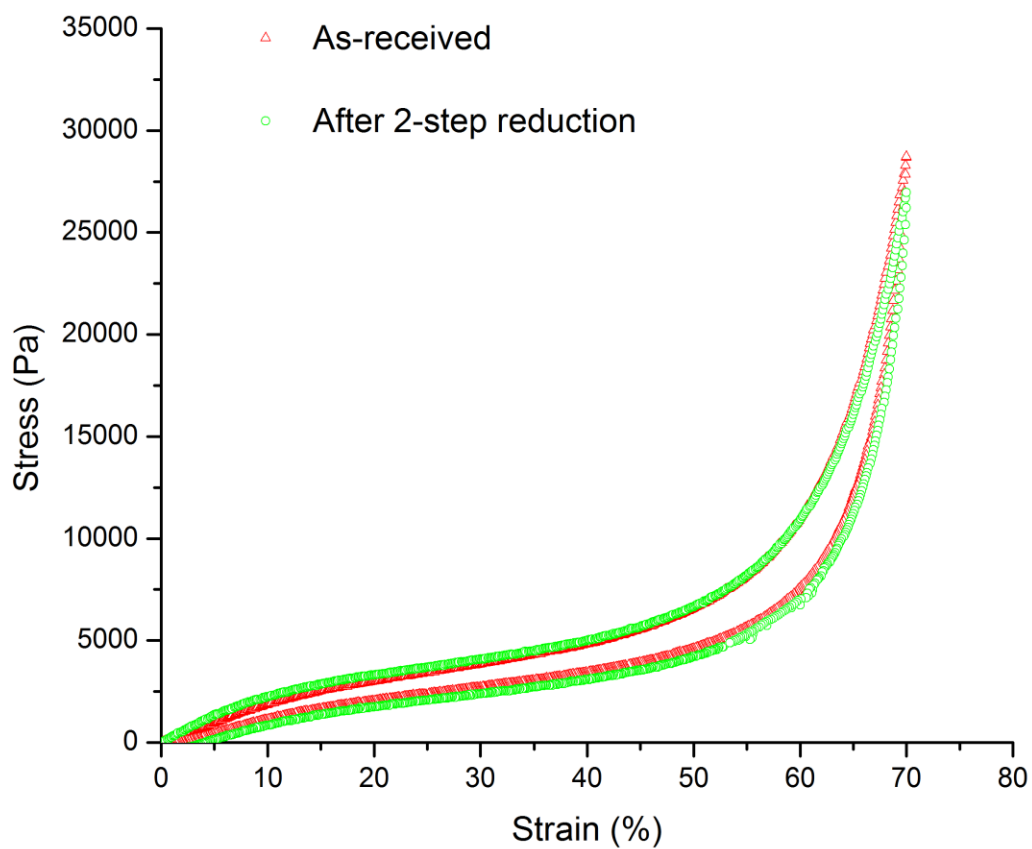


Figure 5.15 Compressive stress-strain (S-S curves) of polyurethane foam in as received condition and after 4 hours of hydrothermal treatment at 100 °C with ethylenediamine plus additional 3 hours of submersion in 65 wt.% hydrazine monohydrate solution at 80 °C.

As expected, an increase in rGO coating thickness led to a slight increase in both the initial modulus and collapse stress of the composite foams. An extension of the classical model for open-cell foam²⁴ to account for the effect of coating layer could be formulated to describe the S-S behavior of the composite. The initial modulus of the composite foam E^* is related to the bulk properties of PU E_{PU} and rGO E_{rGO} , and their volume ratio by (See details in SI):

$$\begin{aligned}
 E^* &= E_{PU} \left(\frac{V_{PU}}{V_{Foam}} \right)^2 + E_{rGO} \left(\left(\frac{V_{rGO} + V_{PU}}{V_{Foam}} \right)^2 - \left(\frac{V_{PU}}{V_{Foam}} \right)^2 \right) \\
 &\approx E_{PU} \left(\frac{V_{PU}}{V_{Foam}} \right)^2 + 2E_{rGO} \left(\frac{V_{rGO}}{V_{Foam}} \right) \left(\frac{V_{PU}}{V_{Foam}} \right)
 \end{aligned} \tag{1}$$

where V_{PU} and V_{rGO} are the volume of PU and rGO, respectively. V_{Foam} is the total volume of the

foam, and $V_{rGO} \gg V_{PU}$ was used to simplify the equation. The last term $2E_{rGO} \left(\frac{V_{rGO}}{V_{Foam}} \right) \left(\frac{V_{PU}}{V_{Foam}} \right)$

represents the increased modulus due to rGO coating. Here both $\frac{V_{PU}}{V_{Foam}}$ and E_{rGO} were

independent of the thickness of rGO coating, while $\frac{V_{rGO}}{V_{Foam}}$ scaled linearly with the coating thickness. As a result, the increased initial modulus depended linearly on the rGO coating thickness. Using this relation, the coating thickness based on the measured modulus could be estimated. For example, from Figure 3, the initial moduli of PU foams PU-rGO-3 and PU-rGO-5 were calculated to be:

$$E^*_{PU \text{ foam}} = 22.5 \text{ KPa}$$

$$E^*_{\text{PU-rGO-3}} = 28.0 \text{ KPa}$$

$$E^*_{\text{PU-rGO-5}} = 30.5 \text{ KPa} \quad [2]$$

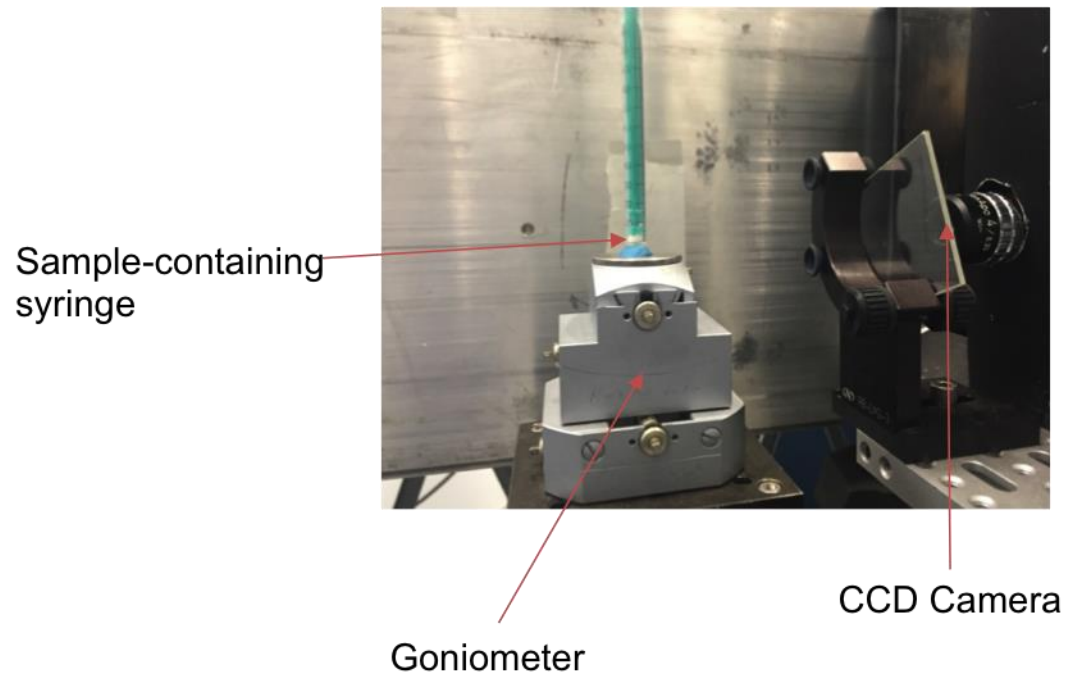
and the ratio of coating thickness of PU-rGO-5 and PU-rGO-3 was estimated to be:

$$\frac{t_{\text{PU-rGO-5}}}{t_{\text{PU-rGO-3}}} = \frac{E^*_{\text{PU-rGO-5}} - E^*_{\text{PU foam}}}{E^*_{\text{PU-rGO-3}} - E^*_{\text{PU foam}}} \approx 1.45 \quad [3]$$

This was close to the measured thickness values $t_{\text{PU-rGO-5}}/t_{\text{PU-rGO-3}} = 670/420 \approx 1.6$.

Synchrotron X-ray Tomography

X-ray tomography analysis was performed at Northwestern's Synchrotron Research Center at Sector 5 of Advanced Photo Source located at Argonne National Laboratory. Transmission tomograms of the samples were recorded at 6 keV using a monochromatic x-ray beam projected through a narrow gap, Si (111) monochromator. PU-rGO composite samples were cut into approx. 1 mm x 1mm x 5 mm stripes and then mounted inside a plastic 1 ml syringe. The sample-containing syringe was then mounted vertically on a rotating Newport stage with an attached goniometer (Figure 5.16). The samples are then aligned with the x-ray beam path and were turned at 0.2 degree increment for 180 degrees for the collection of x-ray tomograms. The beam was then projected on a phosphor screen, of which the resulting image was magnified by 10X and then captured by a Roper Scientific camera with 1300 x 1340, 24 micro pixels. Strain-induced structural changes of the samples can be captured using this setup through movement of the syringe plunger, which compressed the PU-rGO sample mounted within. The resulting raw images were then digitally reconstructed using Amira software for full 3D visualization of the samples.



9

Figure 5.16 X-ray tomography setup.

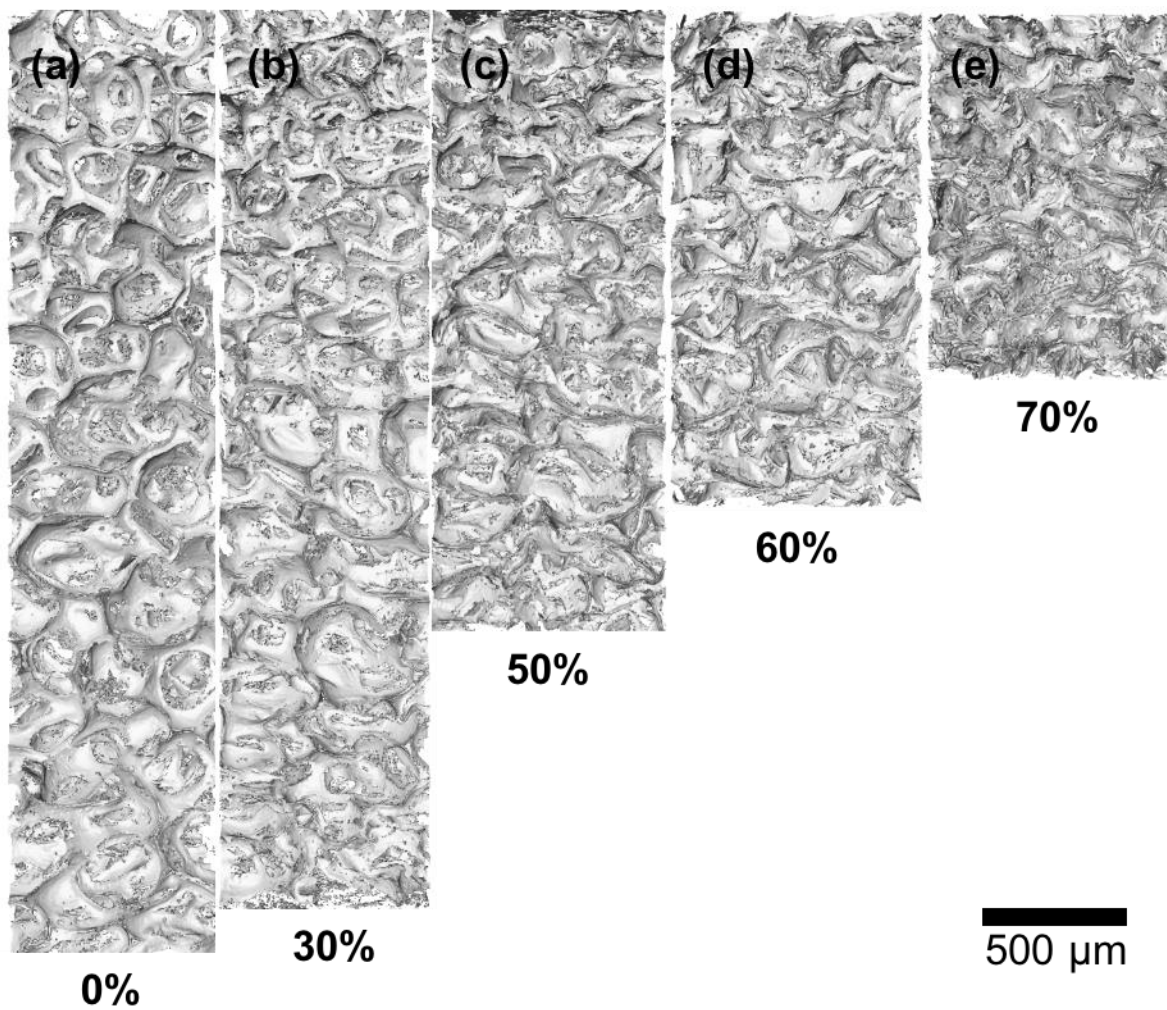


Figure 5.17 X-ray tomography images of PU-rGO-3 foam under (a) 0%, (b) 30%, (c) 50%, (d) 60%, and (e) 70% uniaxial compression.

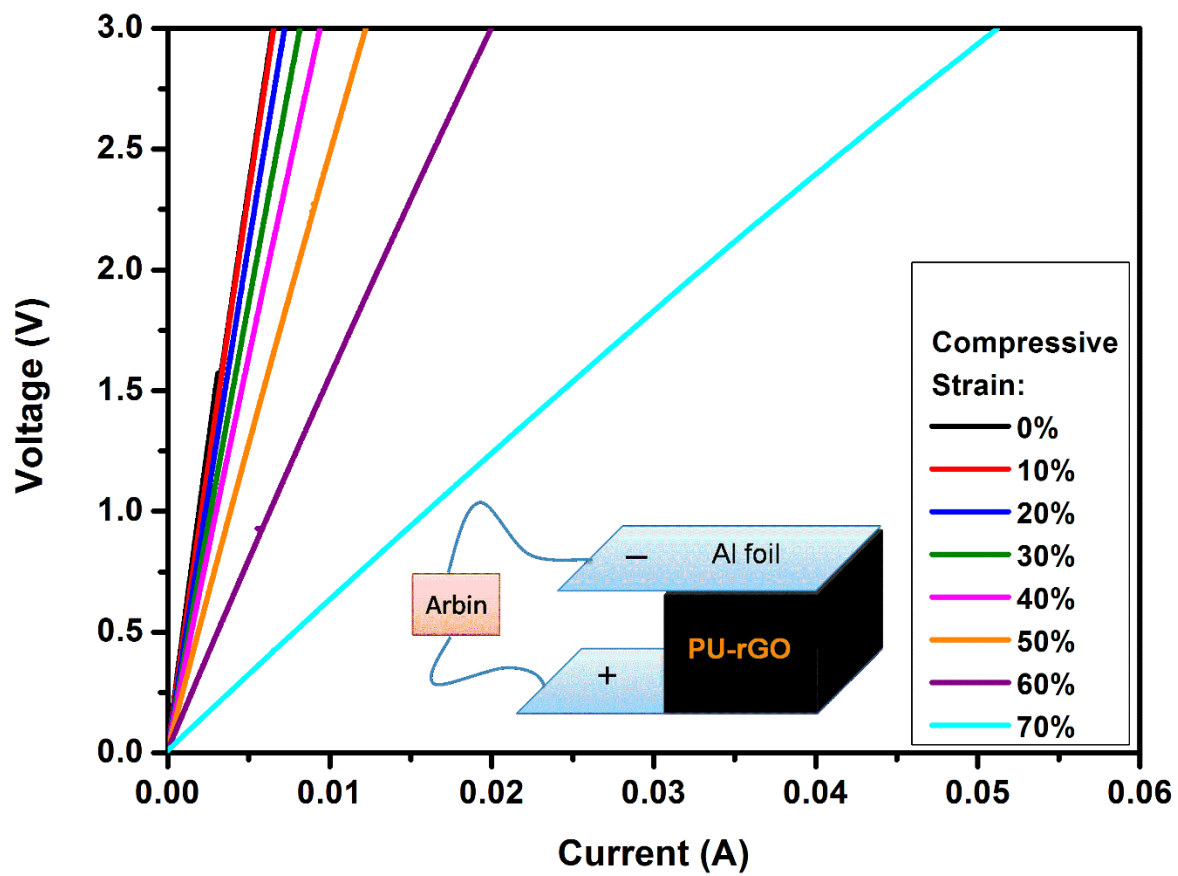


Figure 5.18 I-V curves of PU-rGO-3 with different compressive strain.

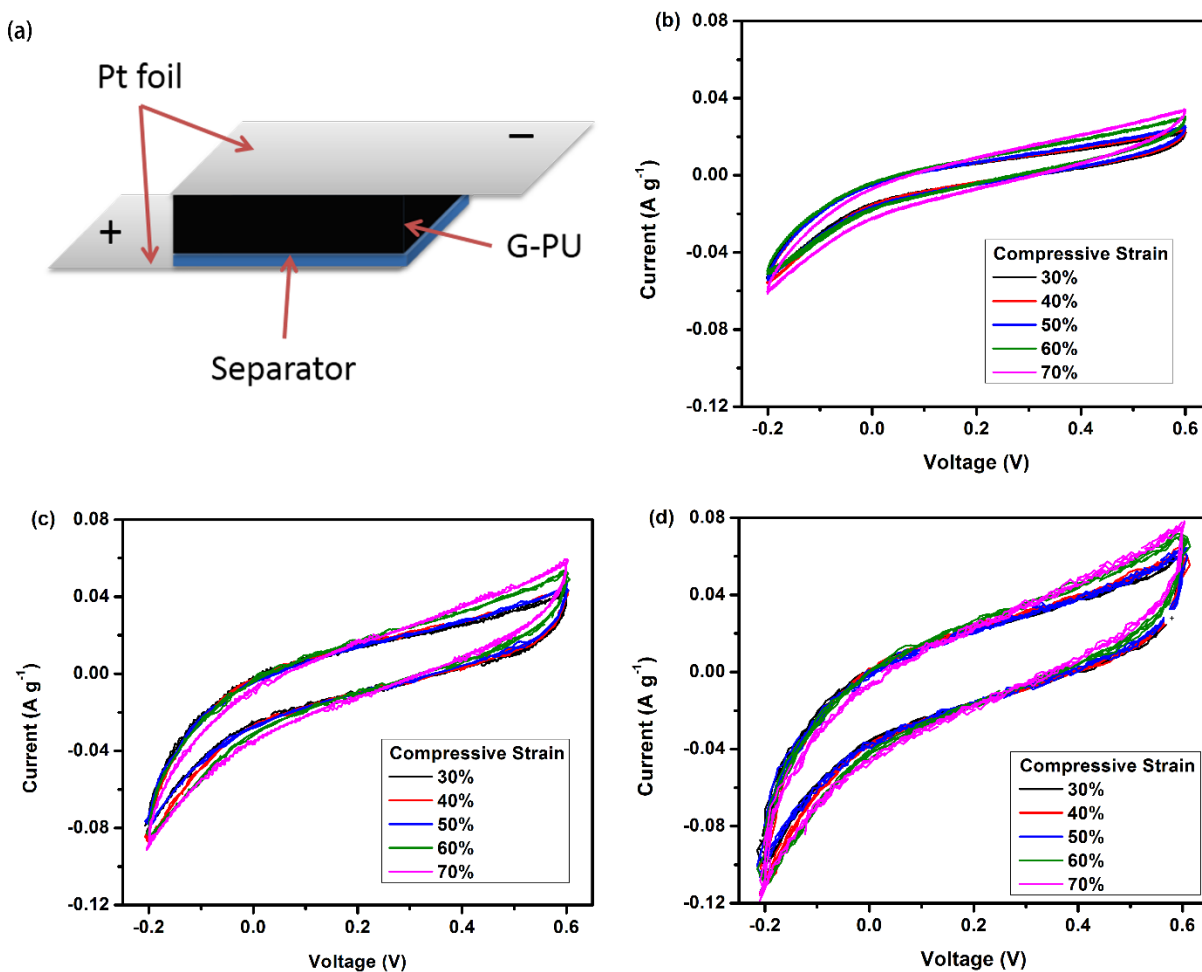


Figure 5.19 (a) A schematic diagram of the electrochemical testing device; Comparison of CV curves of PU-rGO foam with different compressive strain at (b) 10 mV s^{-1} , (c) 50 mV s^{-1} , and (d) 100 mV s^{-1} .

CHAPTER 6

Reduced Graphene Oxide Hydrogel Embedded Polyurethane Composite as Elastomeric Supercapacitor Electrode Materials

*Preliminary draft of publishable work by Yue Yang Yu, Xuejun Bai, Mayfair C. Kung,
Harold H. Kung*

6.1 Abstract

A porous 3D graphene hydrogel composite embedded with particles of additional active materials, graphite and MnO₂, is successfully synthesized using a solution-based self-assembly process. To prevent agglomeration of hydrophobic graphite and MnO₂ particles during the solution-based synthesis process, particles of active materials were wrapped with hydrophilic graphene oxide (GO) platelets through a solution-based processing. This is achieved by spray drying aqueous suspension of active materials and GO, which results in composite particles, consisting of crumpled GO sheets and embedded particles of active materials. The reduced graphene oxide based hydrogel electrode was then synthesized through hydrothermal reduction process using the aforementioned spray-dried particles. An open pore polyurethane foam was used as the supporting matrix to enhance mechanical stability of the composite hydrogel electrode. The GO-assisted spray-drying process stabilizes the hydrophobic particles of active materials, resulting in even distribution of active materials throughout the entire hydrogel structure. The increase in electrical conductivity and electrochemical performance of such composite electrode were demonstrated in a two-electrode electric double layer capacitor setup.

6.1 Introduction

For mobile electronic devices, high-performing and cost-effective energy storage solutions remains to be highly critical. Particularly in applications such as wearable electronic devices and surgical implants that need to be integrated with human's biomechanical functions, the components of the energy storage systems need retain the same degree of mechanical flexibility in all three-dimensional axes. The existing work in this area of flexible energy storage materials includes the use of conducting polymer and carbon films[104], nanotubes and fibers[105-107], graphene sheets[105, 108], all restricted to two-dimensional designs with limited degree of deformability.

To obtain a higher degree of flexibility, freestanding three-dimensional configurations were investigated. Previous work[109] showed the feasibility of fabricating rGO coated porous elastomeric substrate and utilizing its mechanical and electrochemical properties as an elastomeric electrode material for electrochemical capacitor (electric double-layer capacitor). The flexible substrate and the conformal rGO coating offered an excellent platform to observe the effects of mechanical deformations and surface defects have on the electrochemical performance of the composite electrode. Nonetheless, the electrochemical performance of the materials reported in this previous work is below that of the higher performing materials reported in the literature, which exhibited higher than 150 F g^{-1} in capacitance even at high current density of $+20 \text{ A g}^{-1}$ [110]. The low performance of material presented in previous work can be contributed to two key mechanisms. One, the geometric shape of the tested electrodes is unfavorable to its electrical and electrochemical performance. The high thickness of the elastic three-dimensional electrode (up to 25 μm , comparing to most film electrode which are measured in microns) significantly reduces the conductivity of the electrode. In addition, the use of non-conductive polyurethane substrate

further increases the resistance of the electrode and lowers the electrochemical performance of rGO coating, the active phase of the composite electrode. Secondly, the vacuum assisted dip-coating process of PU substrate with GO suspension made it challenging to retain a high loading of electrochemically active rGO phase within the composite electrode.

A novel approach to significantly improve the electrochemical performance of the composite system was designed to address the issue with low loading of active materials presented by previous work. By introducing three dimensional flexible graphene hydrogel phase within the open pores of the porous PU substrate, the loading of active rGO phase is no longer restricted to only the two dimensional pore walls of the substrate, thereby allowing much higher loading of active materials within the microstructure of the PU. The performance of the composite materials was then further improved by introducing secondary phase to the rGO hydrogel, including graphite particles, which improves the electrical double layer capacitance, and MnO₂ nanoparticles, which improves the pseudocapacitance. A novel solution mechanical spray-drying technique was used for embedding the nanoparticles, without the assists of additional chemical processes or additives that are often needed for prevent agglomeration of these hydrophobic nanoparticles during the hydrothermal reduction process of the rGO hydrogel.

6.2 Experimental

6.2.1 Preparation of Spray-dried GO wrapped powder

Nanoparticles of graphite and MnO₂ were obtained from US Nano Research. An aqueous suspension of 0.5 wt.% graphene oxide (GO) was prepared using the modified Hummer's method as described previously²⁶, starting with flake graphite (Asbury Carbons, 230U Grade, High Carbon Natural Graphite 99⁺).

0.6 g of polyvinylpyrrolidone (PVP) (Sigma Aldrich) were added to 120 ml of ethanol (200 proof, Fisher Scientific), which was then sonicated for 10 minutes to ensure the solid is completely dissolved. 1.6 g of either graphite or MnO₂ powder was then added to the prepared ethanol-PVP solution. The suspension was then sonicated for additional 30 minutes to break up any agglomeration of the as-received powder. The suspended ethanol mixture containing PVP and active materials of either graphite or MnO₂ was then mixed with 160 ml of 0.5 wt. % GO suspension. The resulting mixture was then stirred on the stir-plate until it is ready for spray drying.

A Buchi Mini Spray Dryer B-290 is used for the following process. The standard nozzle tip diameter of 0.7 mm was used; the inlet and outlet were set to 120 C and 90 C, respectively. The previously prepared suspension containing GO, PVP, and active materials (graphite or MnO₂) were then fed through the system using the built-in suction pump, while being stirred to prevent phase separation of the suspension. The resulting powder, containing either graphite (GO-G) or MnO₂ (GO-Mn) was captured by the cyclone particle collector and was then collected and stored in air-tight container for future use.

Functional principle

Step 1 - Heating:

Heat the inlet air to the desired temperature (max. 220 °C)

Step 2 - Droplet formation:

Two-fluid nozzle for the B-290 and.

Step 3 - Drying chamber:

Conductive heat exchange between drying gas and sample droplets.

Step 4 - Particle collection:

Cyclone technology

Step 5 - Outlet filter:

Collection of finest particles to protect the user and the environment.

Step 6 - Drying gas:

Delivered by aspirator

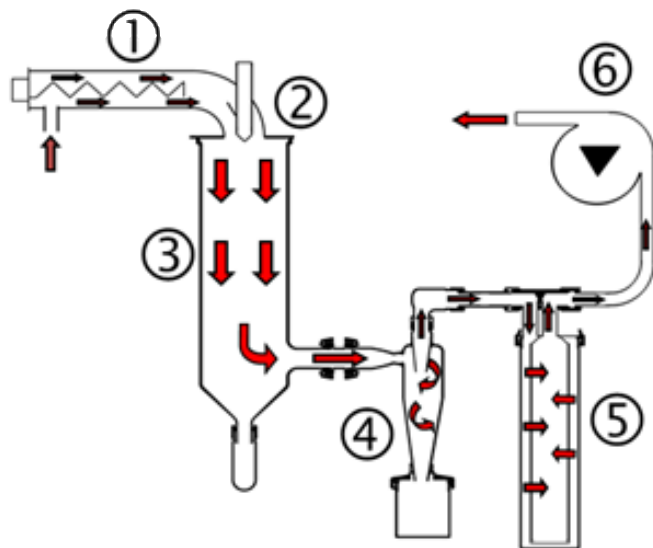


Figure 6.1 Diagram showing the functional principle of Buchi Mini Spray Dryer B-290. Diagram is retained from Technical Data Sheet publicly available from www.buchi.com

6.2.2 Preparation of PU-rGOH Composite Electrode

Similar to our previous published work, pieces of polyurethane (PU) foam, 2.5x2.5x2.5 cm³, were cut from larger stock pieces, Type TC-266(50/100), obtained from BJB Enterprises (Tustin, CA). The pieces were gently wash with a mixture of DDI water and ethanol and then vacuum dried overnight to remove any remaining moisture.

40 ml 0.75 wt. % GO suspension was obtained from the original 0.5 wt. % suspension through further centrifugation. 600 mg of L-ascorbic acid (Sigma Aldrich) was then added to the GO suspension and stirred for 30 minutes. 1.2 g of either GO-G or GO-Mn powder was added to 40 ml of ethanol and stirred for 30 minutes as well. The two suspensions, one with GO and L-

ascorbic acid and the other with spray-dried powder, were mixed together and stirred for an additional 30 minutes. The pre-cut PU piece was then completely submerged into the mixed suspension and fully compressed multiple times to remove any trapped air bubbles within the porous structure of the PU foam piece and to ensure complete infiltration of prepared mixture. The mixture, along with the submerged PU piece, was then sealed in air-tight glass vial and heated in oil bath at 80 °C for 24 hours. The resulting PU-rGOH composites were then removed and washed in DDI water for 24 hours to remove any excess L-ascorbic acid. The samples were then vacuum dried overnight to remove the remaining moisture. The graphite containing sample was labeled as G-PGH and MnO₂ containing sample was labeled as Mn-PGH.

6.2.3 Sample Characterization and Measurements

Scanning electron microscopy images were collected with a high-resolution field emission scanning electron microscope (FESEM, Hitachi SU8030). X-ray photoelectron spectroscopy (XPS) was performed using a Thermo Scientific ESCALAB 250Xi (Al K α , 1486.6 eV).

The stress-strain relationships were determined with a mechanical tester (MTS Sintech 20G), using a compression and rebound speed of 5 mm s⁻¹.

For electrical resistance measurements, aluminum foils serving as electrical contacts (Alfa Aesar, 0.025mm, 99.99%) were pasted with silver conducting paste onto two opposing faces of a PU-rGO foam piece to improve electrical contact. A voltage ramp from 0 to 3 V was applied across the current collectors using a potentiostat/galvanostat system (Arbin Instruments BT2000), which recorded the current passing through the foam piece.

Electrochemical tests of a foam piece were carried out in a three electrodes setup, with PU-rGO composite as the working electrode, Ag/AgCl (CH Instruments) as the reference electrode,

and Pt foil (Alfa Aesar, 0.025mm, 99.9%) as the counter electrode. An aqueous solution of K_2SO_4 (0.5 M, Sigma Aldrich, 99% ACS) was the electrolyte. Using an electrochemical workstation (Autolab PGSTAT128N), current at densities of 0.05 A/g, 0.1A/g, and 0.5 A/g, based on the weight of the active materials in the foam pieces, was applied to charge and discharge the sample over a voltage range of -0.2 to 0.6 V. Electrochemical impedance spectrometry was performed using the same Autolab workstation.

6.3 Results and Discussion

The as-received graphite and MnO₂ particles were observed to have diameters ranging 5-10 μm and <1 μm, respectively, after sonication in ethanol solution, as shown in Figure 6.2a and c. A piece of Si wafer was dip coated with the suspension containing the particles. After drying, the Si wafer was then observed under SEM. As a result, slight agglomeration of both the graphite and MnO₂ were observed (Figure 6.2a and c). This is due to the surface tension of the ethanol pulling the micro/nanoparticles together upon drying on the Si wafer. After spray drying with GO suspension, both the graphite and MnO₂ were evenly wrapped with GO sheets (Figure 6.2b and d). The diameters of both types of spray-dried GO powders was approx. 10-30 μm in diameter.

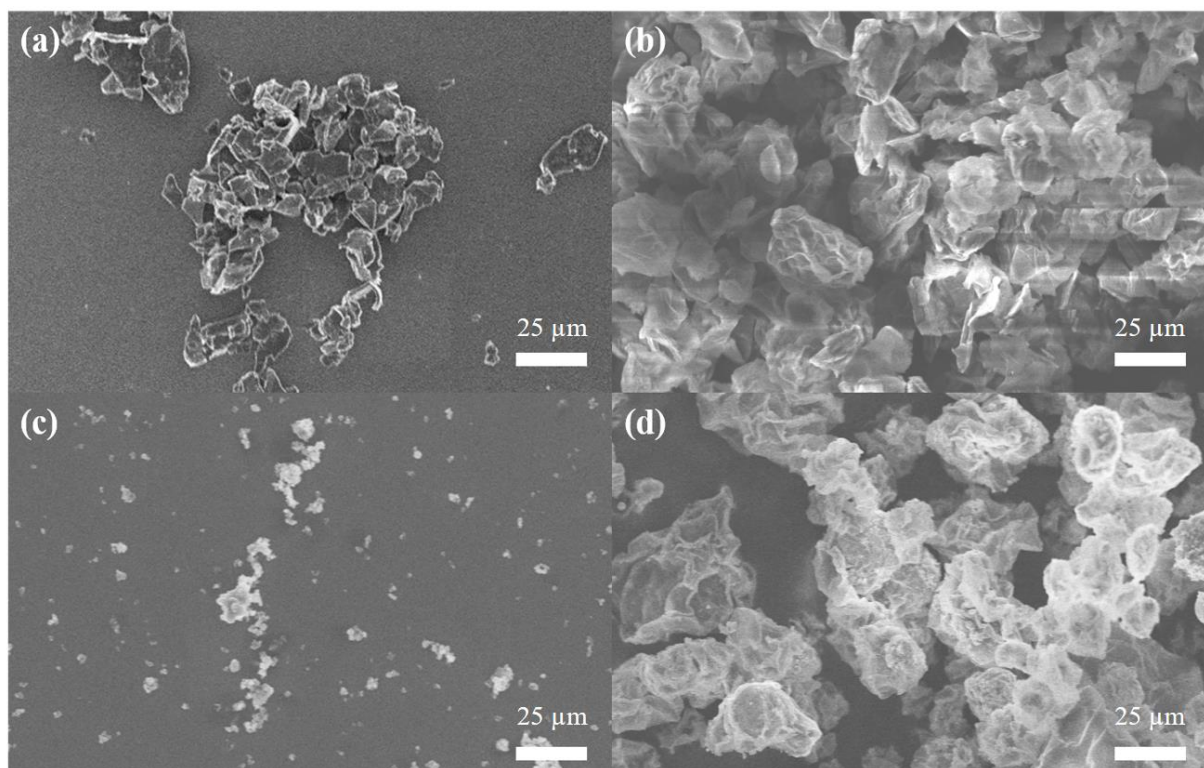


Figure 6.2 SEM images of (a) as-received graphite particles after sonication, (b) spray-dried graphene oxide wrapped graphite particles, (c) as-received MnO₂ particles after sonication, (d) spray-dried graphene oxide wrapped MnO₂ particles. Scale bar is 25 μm.

As reported in previous work[109], the PU has an open pore structure with average pore diameter around 500 μm , allowing suspension of GO-G and GO-Mn to infiltrate the PU structure and forming rGOH upon hydrothermal reduction. The resulting samples show not only rGOH forming within open pores of the PU substrate (Figure 6.3a and c), but also the surface of the PU substrate itself was coated with layers of reduced graphene oxide sheets as (Figure 6.3b and d). Similar to prior work[109], the G-PGH and Mn-PGH samples remained to highly flexible, as exhibited by its elastomeric PU substrate. As shown in Figure 6.XX, a slight increase in the elastic modulus of the G-PGH and Mn-PGH was observed, due to the additional graphene hydrogel phase within the open pores of the PU supporting matrix. The addition of rGOH structure within the pores of PU substrate does not affect the mechanical properties of original PU substrate by much. Structural deformation of the composites under compression was identical to previous reported results[109], which can be described adequately with the classical model for open-cell foams[111].

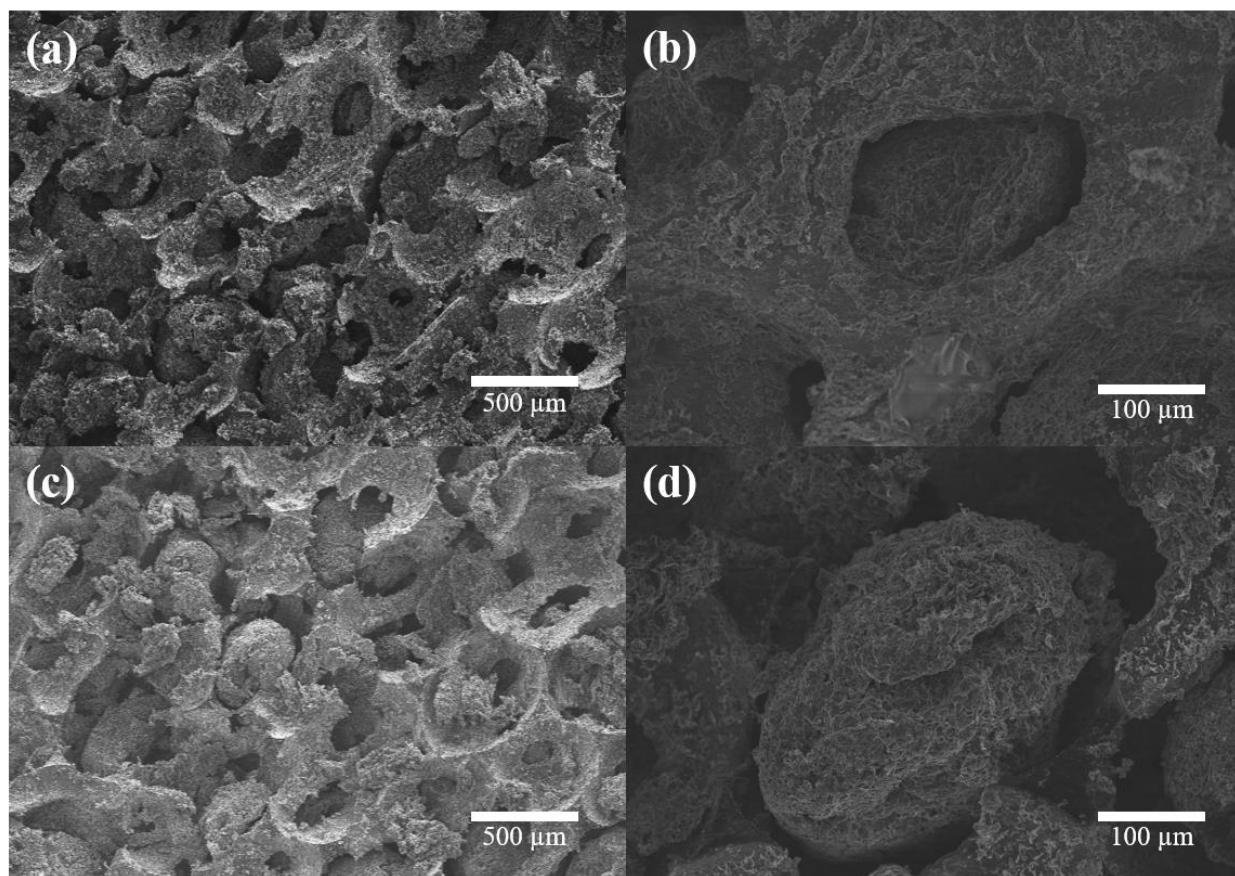


Figure 6.3 SEM images of G-PGH under (a) 35X and (b) 350X magnifications and Mn-PGH under (c) 35X and (d) 350X magnifications. Corresponding scale bars are shown within each image.

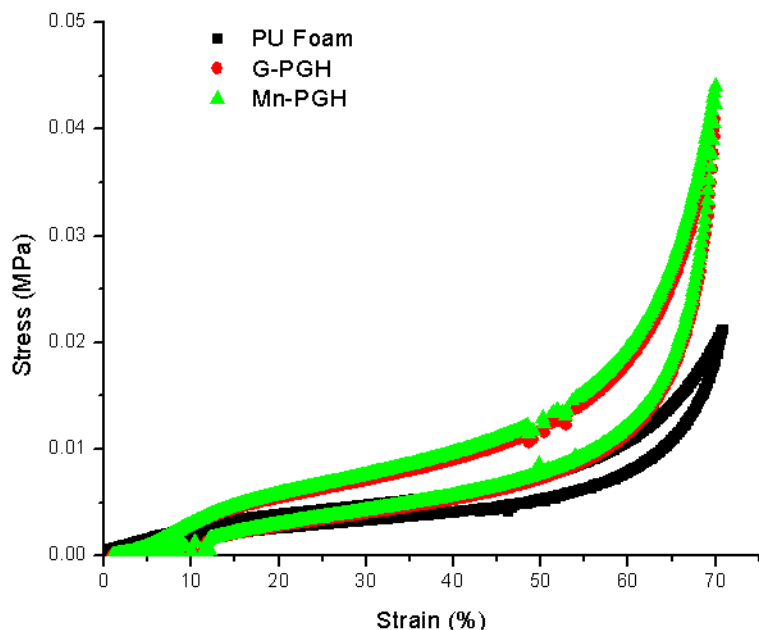


Figure 6.xx Stress-strain measurement of as-received PU foam, G-PGH, and Mn-PGH samples.

For the XPS spectrum shown in Figure 6.4, flakes of rGOH were removed from G-PGH and Mn-PGH samples using copper backed double sided tape and then characterized with XPS. C 1s spectra of G-PGH sample showed a higher intensity C-C peak, due to the embedded graphite particles (Figure 6.4a). For Mn-PGH sample, its O 1s peak (Figure 6.4d) is entirely composed of organic C-O and C=O peaks at ~ 531.5 eV and ~ 533 eV, respectively, with no detectable metallic Mn-O peak at ~ 529 eV[112]. The C:O ratio of Mn-PGH is 6.5:1, indicating that the hydrothermal reduction of the GO phase of the composite is successful. The Mn 3s spectra (Figure 6.3e) showed two distinct peaks at ~ 84.4 eV and ~ 89.3 eV. The ΔE of the two peaks is approximate 4.9 eV, showing that the oxidation state is Mn $^{4+}$ [113].

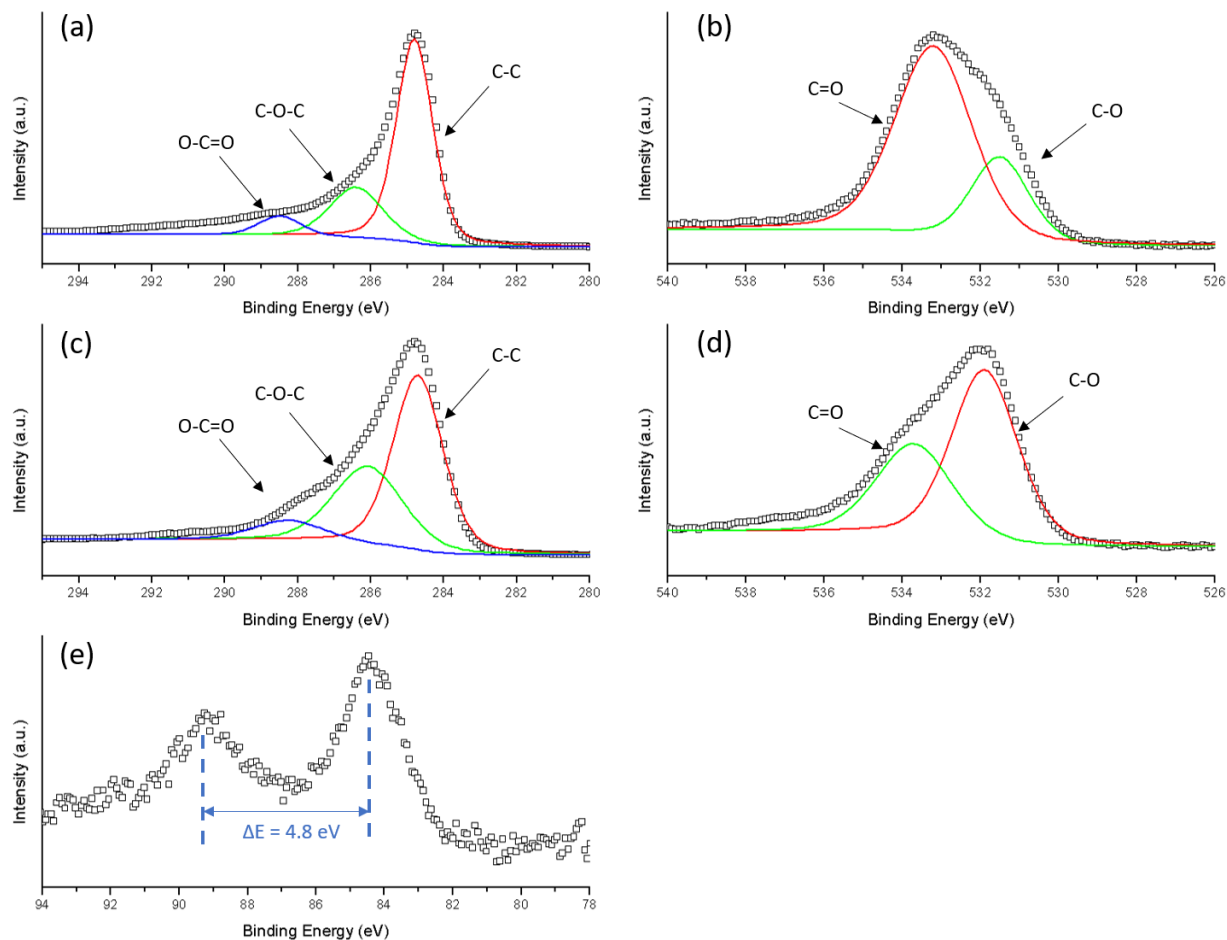


Figure 6.4 XPS spectrum of (a) C 1s and (b) O 1s of G-PGH, (c) C 1s, (d) O 1s, and (e) Mn 3s of Mn-PGH.

Both the G-PGH and Mn-PGH were compressed to 70% for up to 100 cycles. Resistance of the samples at 0, 50, and 100 cycles (Figure 6.5). Both samples showed minimal degradation to electrical conductivity. The G-PGH showed slightly lower resistance due to its higher conductive carbon content relative to the Mn-PGH. Both samples showed a linear trend in reduction of resistance as higher compressive strain is applied to the samples up to 50% strain. After which, the resistance value for both sample plateaued. This can be explained through the deformation mechanism of the PU substrate upon compression. When uncompressed, the rGOH particles within the open pores of the PU substrate are free standing, as shown in Figure 6.3d.

Since the rGOH particles were separated by the wall of the porous PU substrate, they did not contribute significantly to the electrical conductivity of the sample. As the sample underwent compression, increasing number of rGOH particles became in contact with each other as the open pores of the PU substrate collapse (see Figure 5.5). At strain higher than 50%, most of the pores of the PU substrate collapsed, allowing majority to the rGOH to be in physical contact of each other and allowing electricity to pass through and forming large number of conductive pathways within the sample. With majority of rGOH particle already electrically conductive, increasing the strain at 50% and above therefore do not further lower the resistance by much.

The capacitance and impedance of the G-PGH and Mn-PGH samples were measured as a function of the applied compressive strain (Figure 6.6) in configuration shown in Figure 5.19. At low current density of 0.05 A g^{-1} , the capacitance for both samples increased as the compressive strain was increased. And as expected, the embedded MnO_2 particles within the Mn-PGH exhibited higher capacitance due to the pseudocapacitance. However, the capacitance plateaued under 0.1 A g^{-1} and decreased under 0.5 A g^{-1} at strain above 50% for both samples. This is again due to the deformation mechanism of the PU substrate, as higher than 50% strain closes the previously open pores with the porous PU substrate. At higher current densities, the required fast ion transport can no longer infiltrate the collapsed pores of the PU substrate and reducing the electrochemical performance of the rGOH and its embedded active materials of graphite or MnO_2 . The EIS spectrum showed similar trends. At compressive strain between 30 to 50%, the charge transfer resistance of the test cells was reduced as the strain was increased, with a slight reduction in series resistance observed as well. At 70% compressive strain, the charge transfer resistance increased from the measurement taken at 50%, as indicated by the larger semi-circle of the EIS

plot (Figure 6.6c and d). Both the electrical and electrochemical measurements revealed that the non-conductive PU substrate was still hindering the performance of the composite electrode.

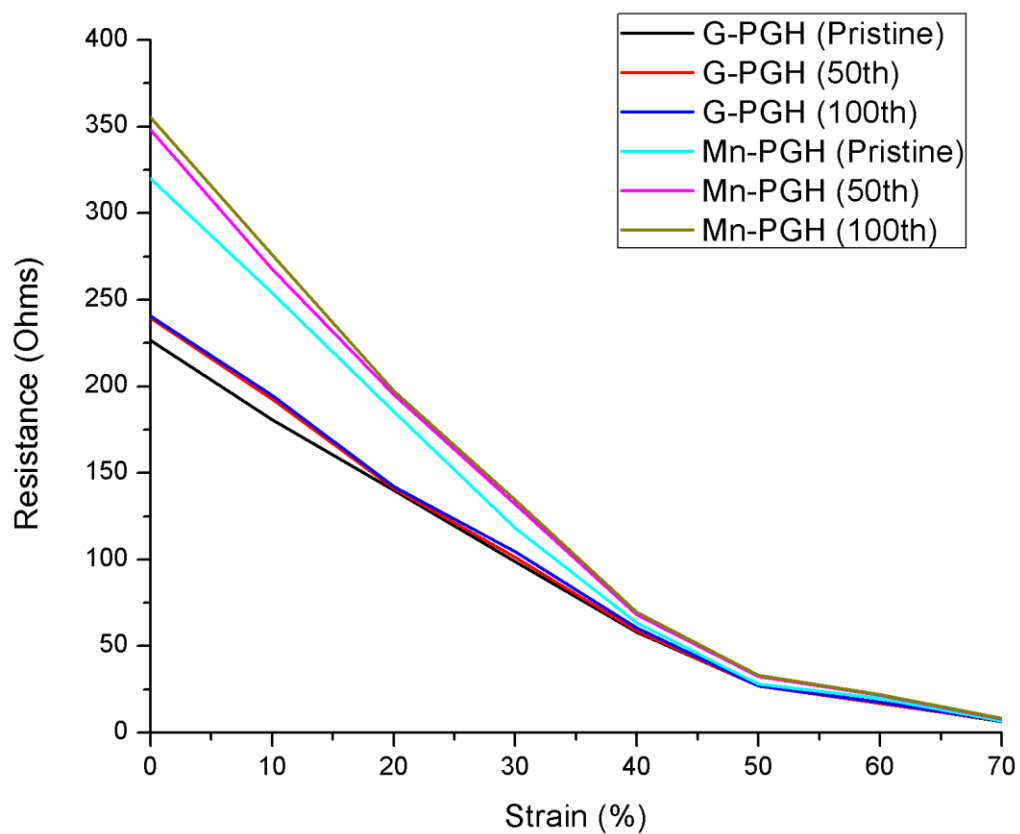


Figure 6.5 Resistance of G-PGH and Mn-PGH electrode samples under compressive strain of 0 to 70% and after 0, 50, and 100 repeated cycles of 70% compression.

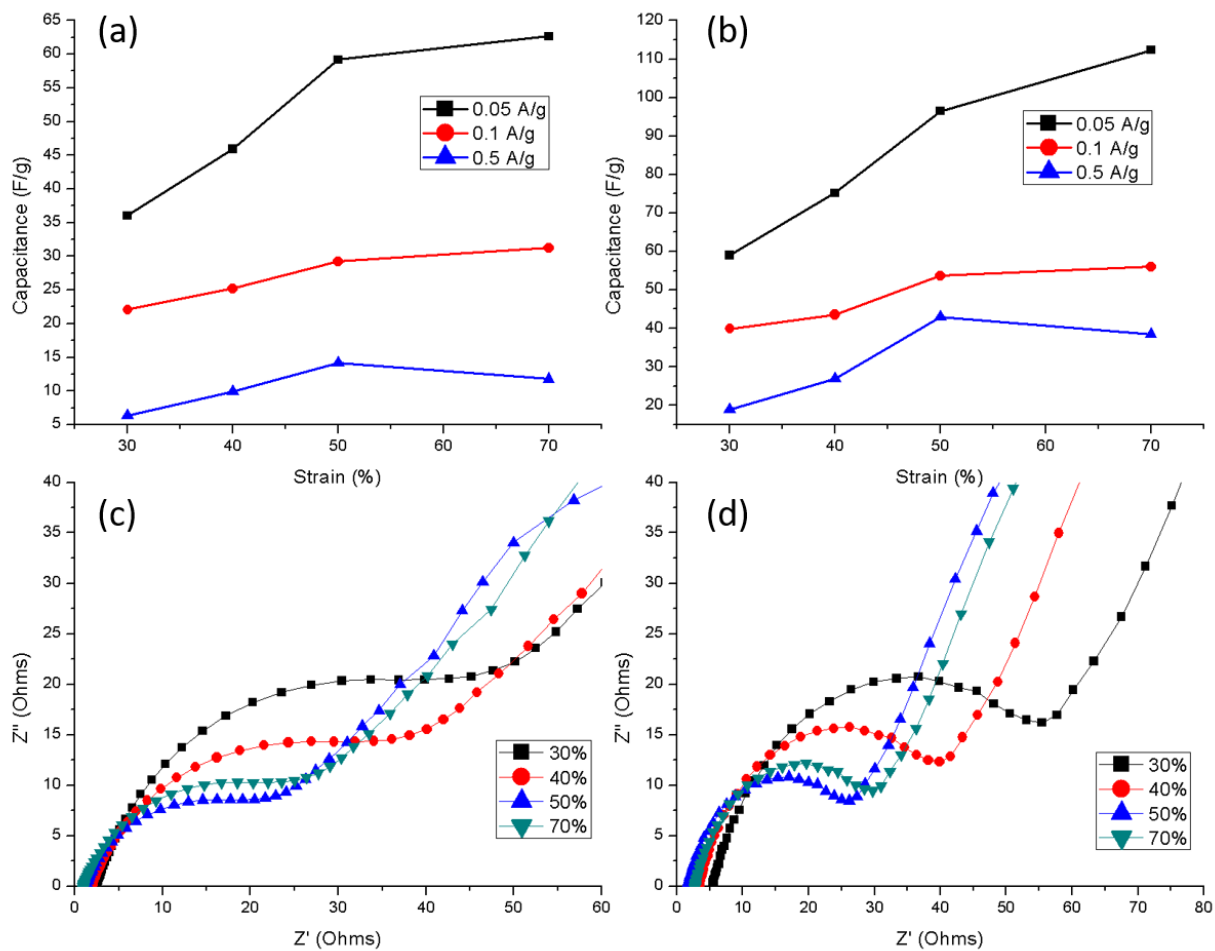


Figure 6.6 Capacitances of (a) GO-G and (b) GO-Mn samples under 0.05 A g^{-1} , 0.1 A g^{-1} , and 0.5 A g^{-1} and under compressive strain of 30%, 40%, 50%, and 70%. EIS spectrum of (c) GO-G and (d) GO-Mn samples under compressive strain of 30%, 40%, 50%, and 70%.

6.4 Conclusion

Mechanical spray drying process was successfully implemented to wrap the hydrophobic exterior of graphite and MnO_2 particles with hydrophilic GO sheets. The resulting powder was then suspended with GO suspension and then underwent chemically assisted (L-ascorbic acid) hydrothermal reduction to form rGO hydrogel. By filling the porous PU substrate of these suspended mixtures, composite electrode materials can be formed which retained the highly flexible mechanical properties of the pristine PU substrate. The conductivity and the electrochemical performance was improved two to three times that of the PUrGO composite reported in Chapter 5; however, the use of non-conductive PU substrate still significantly hinders the performance the composite electrodes, particularly at high current densities.

CHAPTER 7

Effects of Ion Infiltration on the Mechanical Properties of Free Standing

Reduced Graphene Oxide Hydrogel

Preliminary draft of publishable work by Yue Yang Yu, Xuejun Bai, Mayfair C. Kung,

Harold H. Kung

7.1 Introduction

Graphene based hydrogels offer a unique combination of free-standing three-dimensional structure and high degree of multi-axial flexibility while retaining the excellent electrical and electrochemical properties of its graphene base material. While the hydrogel materials have been studied intensively in energy storage applications, particularly as electrochemical capacitor electrodes, much of the contemporary research focus have neglected the flexible mechanical properties of such hydrogel materials. On the other hand, a review of the literature has revealed that have been multiple high impact studies on the drastic effects of trace amount of intercalated ions have on the stability and mechanical strength of stacked sheets of graphene, graphene oxide, and reduce graphene[114-118]. The goal of this study is to offer an improved understanding of the mechanical behaviors and offer solution based process via ion-filtrating the reduced graphene hydrogel (rGOH) with monovalent and divalent salt solutions to modify the elastic modulus of the rGOH materials.

7.2 Experimental

7.2.1 Preparation of Reduced Graphene Oxide Hydrogel Samples

As reported in our previous published work, an aqueous suspension of 0.5 wt.% graphene oxide (GO) was prepared using the modified Hummer's method as described previously²⁶, starting with flake graphite powder (Asbury Carbons, 230U Grade, High Carbon Natural Graphite 99⁺).

The 0.5 wt.% GO suspension was then diluted down to 0.25 wt.% concentration using DDI water. 40 ml of the said GO suspension was then poured into a 40 ml Teflon autoclave tube (to the brink). The Teflon tube was then capped and sealed within a stainless-steel pressure vessel. The device was then put into a programmable oven. The oven was first ramped to 90 °C in 30 minutes and then dwelled at this temperature for 12 hours. Temperature was then slowly ramped to 160 °C in 12 hours. This is to allow a consistent and cavity-free reduced graphene oxide hydrogel (rGOH) structure to form from the GO suspension. The sample was then dwelled at 160 °C for additional 12 hours to fully reduced the hydrogel sample. Due to the cylindrical shape of the Teflon vessels used, the resulting hydrogel is conformal to the vessels used and retain the same cylindrical shape after hydrothermal reduction.

For control sample, the resulting hydrogel from the previous step was washed in DDI water for 72 hours to remove any residual ions from the GO synthesis steps and any possible containments during the hydrothermal reduction step described above. For the ion-infiltrated samples, samples were soaked in the corresponding solutions (Table 7.1) for 72 hours after the DDI water washing. The ion-infiltrated samples were then wash in DDI water for additional 72 hours to remove any excess ions that were not trapped between the stacked reduced graphene oxide layers of the rGOH. Both the control and ion-infiltrated samples were then vacuum dried for 24

hours to remove remaining moisture. Three complete batches of samples were prepared for consistency.

Samples	Weight Percent (wt. %)				
	Li	Na	K	Mg	Ca
Control	0.00096	0.00045	0.00051	0.00012	0.00023
1M HCl	0.00057	0.00061	0.00080	0.00034	0.00045
2M HCl	0.00077	0.00019	0.00021	0.00014	0.00074
1M LiCl	5.36680	0.00753	0.00316	0.00295	0.00472
1M NaCl	0.00770	15.81816	0.00420	0.00164	0.00148
1M KCl	0.00588	0.34100	22.53967	0.00746	0.00374
1M MgCl ₂	0.00039	0.00968	0.00101	17.26059	0.00446
1M CaCl ₂	0.00358	0.00473	0.00238	0.00373	24.74610

Table 7.1 List of solutions used for ion-infiltrated rGOH samples and the resulting weight percentage of ions from ICP

7.2.2 Characterization

Scanning electron microscopy images were collected with a high-resolution field emission scanning electron microscope (FESEM, Hitachi SU8030). X-ray photoelectron spectroscopy (XPS) was performed using a Thermo Scientific ESCALAB 250Xi (Al K α , 1486.6 eV). All rGOH samples were cut with cleaned razor blades and then peeled with copper double tape to reveal fractured surfaces of the stacked graphene layers for XPS measurements.

Inductively coupled plasma mass spectrometry (ICP-MS) was conducted to all samples to measure the amount of residual cation ions after sample preparations. Thermo iCAP Q ICP-MS was used for this study. rGOH samples were calcinated at 750 °C in lab air for 6 hours. The residues were then dissolved in concentrated nitric acid (Sigma-Aldrich 70% ACS reagent) for ICP-MS measurements.

The stress-strain relationships were determined with a mechanical tester (MTS Sintech 20G), using a compression and rebound speed of 0.5 mm s^{-1} . Each sample was loaded along its cylindrical axis for uniaxial compression to 70% strain for 6 times. The length and diameter of each samples were carefully measured with a caliper to calculate the correct stress in MPa and strain in mm/mm or %.

7.3 Results and Discussion

The cross-sectional SEM image of control sample is shown in Figure 7.1a, with loosely stacked reduced graphene oxide sheets forming the pore walls of the hydrogel (Figure 7.1d). Ion-infiltration process introduced no observable changes to the microstructure of the hydrogels (Figure 7.1b and c). All samples were highly porous with average pore diameter of $200\mu\text{m}$ and able to retain significant amount water prior to vacuum drying.

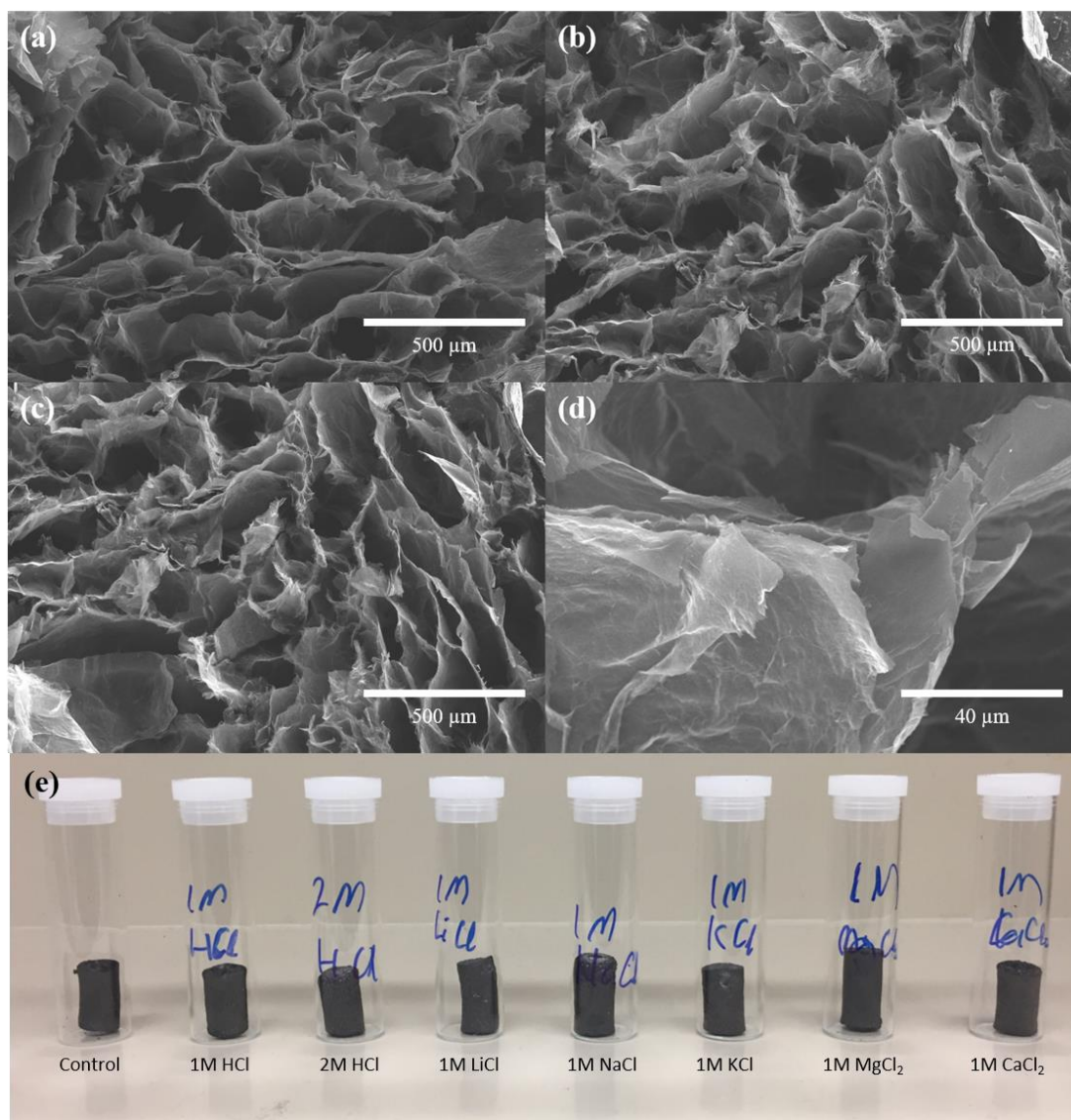


Figure 7.1 SEM images of (a) control, (b) 2M HCl, (c) 1M MgCl₂, (d) pore walls of rGOH. (e) Reduced graphene oxide hydrogel (rGOH) samples after ion infiltration and vacuum drying.

ICP-MS of the control sample showed negligible amount of ion contents, indicating no ion contamination of the sample during the synthesis process (Table 7.1). The C:O ratio of the control was approximately 7:1 (Figure 7.2). Both the 1M and 2M HCl treated samples showed nearly no traceable amount of chlorine after washing (Table 7.1), indicating that chlorine anions were not intercalated into the stacked graphene layers of the rGOH. Monovalent and divalent ions were successfully introduced to the stacked graphene layers of the rGOH, as shown by the XPS spectra in Figure 7.3 and high weight percentages of Li, Na, K, Mg, and Ca ions measured by ICP-MS (Table 7.1). Lithium were difficult to detect with XPS due to low *Z*-number and the lack of secondary peaks that could assist in confirmation, hence the Li 1s spectrum in Figure 7.4a showed mostly background noise.

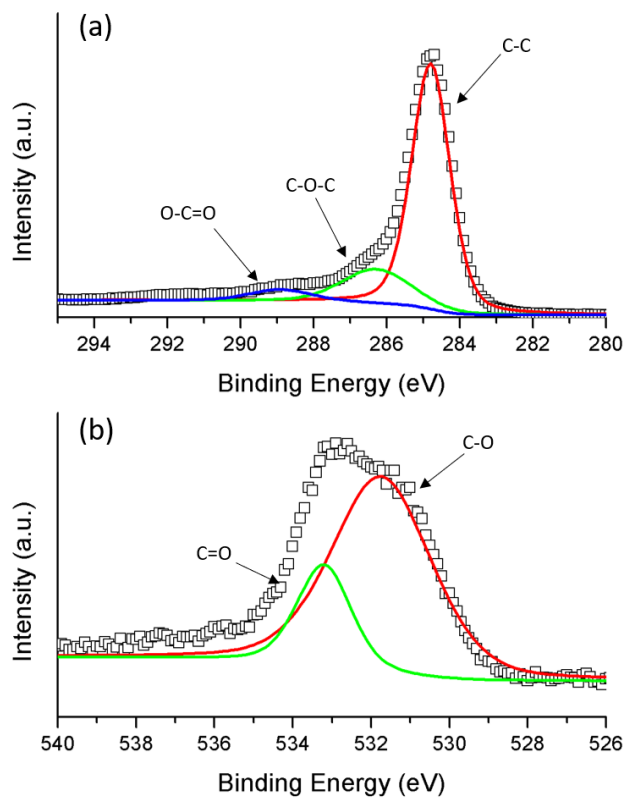


Figure 7.2 XPS spectrum of (a) C 1s and (b) O 1s peaks of control sample of rGOH.

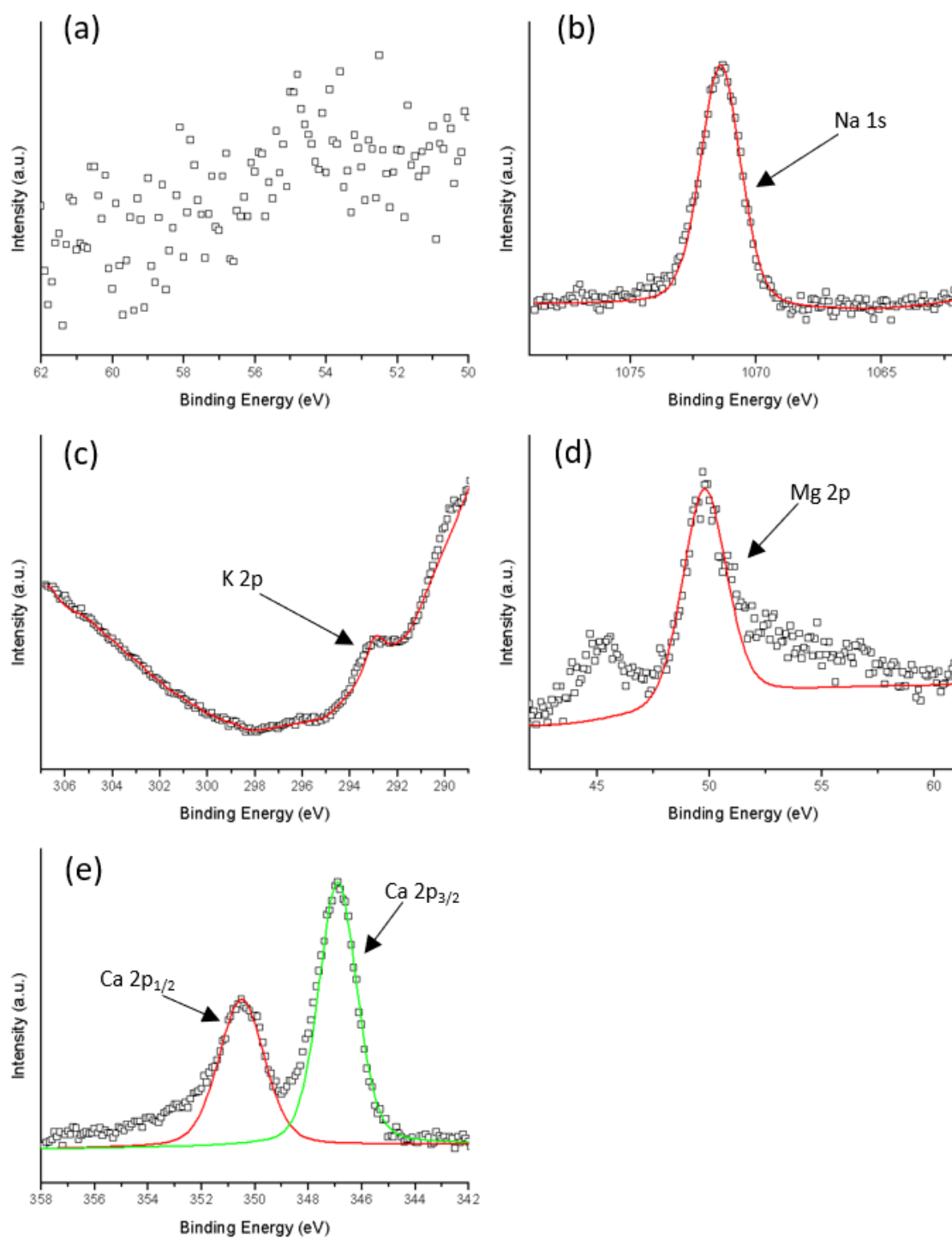


Figure 7.3 XPS spectrum of (a) Li 1s peak of 1M LiCl, (b) Na 1s peak of 1M NaCl, (c) K 2p peak 1M KCl, (d) Mg 2p peak of 1M MgCl₂, (e) Ca 2p peak of 1M CaCl₂ infiltrated rGOH samples.

During initial cycle of compression test, all rGOH samples showed linearly deformation regime (Figure 7.5). The regime is not to be confused with the initial elastic deformation commonly exhibited by metallic materials and such. Instead, the linearly deformation was caused by the crumpling of the small irregular edges at the two ends of the cylindrical sample. Once the irregular features were crushed, the stress mostly plateaued due to the continuing crumpling of the sample under uniaxial compression. Upon reaching 50-60 % strain, the stress increased dramatically as the sample is now fully compressed and is now undergoing densification due to the continuing uniaxial compression. All hydrogel samples are highly flexible, due to the loosely stacked graphene layers forming the pore walls, and were able to rebound back to ~70% of its original length, despite being compressed down to 30% of its axial length.

In the second cycle (labeled as 1 or R1 in Figure 7.5), the samples exhibited a mostly elastic stress-strain relationship. A linearly elastic regime was first observed in the first 20%. As the sample densify under increasing strain, the modulus increased dramatically. This behavior was observed in the following cycles, with a slight degradation in the sample's modulus and rebounded length. However, by the fourth and fifth cycles, the samples have mostly stabilized and showed minimal degradation in its elastic properties. The difference in the stress-strain relationship between the first and following cycles of compression can be contributed to the following mechanism. During the first cycle, heavily cross-linked graphene sheets within the porous structure of the sample was broken. The breakings of those cross-linked bonds between the graphene sheets produced plateau region of the stress strain curves seen in Figure 7.5. In the following cycles, very few remaining bonds remained, allowing the samples to be mostly elastic upon compression. As cycles were repeated, the mechanical properties of the samples stabilizes as almost all cross-linking bonds were broken. Both the control (Figure 7.5a) and ion-infiltrated

samples showed similar stress-strain properties, with ion-infiltrated samples, particularly the 1M MgCl_2 shown in Figure 7.5b, able to endure higher stress comparing to the control sample.

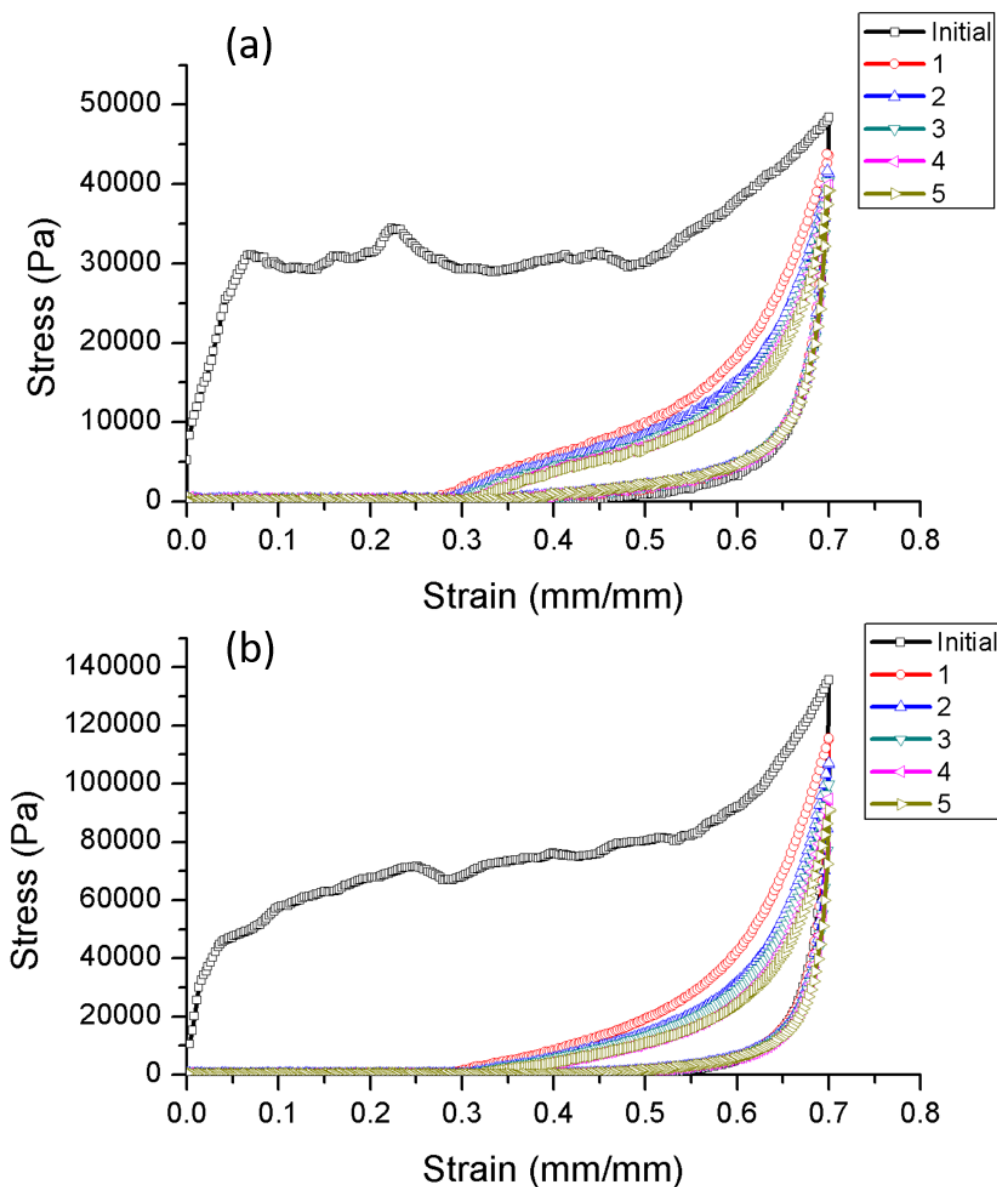


Figure 7.5 Stress-strain curves of (a) control and (b) 1M MgCl_2 infiltrated rGOH samples under 6 repeated cycles of compression up to 70% strain.

Elastic moduli were calculated from the second, third, fourth, and fifth cycles of compression test. The modulus was derived from initial linear region of the stress-strain curves, by measuring the slope at the initial point of the curve. Average of the five measured was then

noted as the modulus of each corresponding samples, as shown in Figure 7.6. As expected, control sample, with no ion infiltration, exhibited the lowest elastic modulus. For HCl treated samples and despite the lack of detectable chlorine in the XPS spectra (Figure 7.3a and b), increasing the concentration of HCl from 1M to 2M resulted in a small but detectable increase in the sample's elastic modulus. For 1M LiCl, NaCl, and KCl infiltrated samples, the elastic modulus was slightly increased but might be within the range of experimental errors. For 1M MgCl₂ and 1M CaCl₂, the presence of divalent ions significantly increased the elastic modulus of the hydrogel samples from 0.0381 MPa of the control sample to 0.0801 and 0.0964 MPa of the MgCl₂ and CaCl₂ samples, respectively. As reported in literature[114-116], the divalent ions are able to bridge the functional groups on the GO and rGO. The ions were effectively “cross-linking” the rGO sheets through the remaining functional groups, resulting in the increase in elastic modulus reported in Figure 7.6 and Table 7.2. The monovalent ions of Li⁺, Na⁺, and K⁺ were not effective in bridging the functional groups within the hydrogel and thereby had a minimal impact on the elastic modulus of the hydrogels.

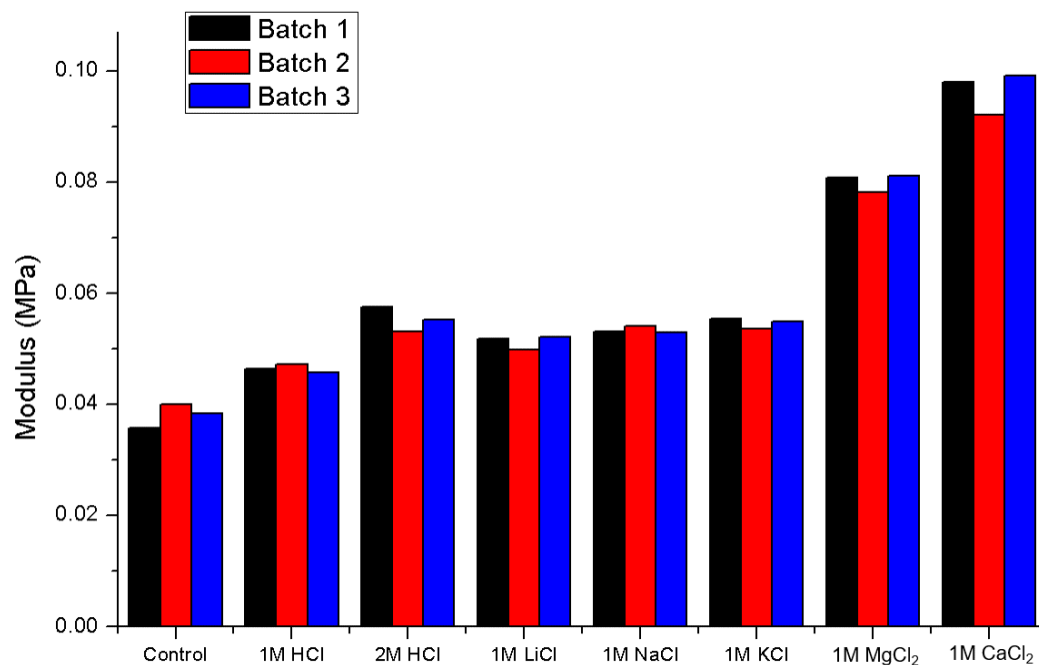


Figure 7.6 Elastic modulus of rGOH samples from batch 1, 2, and 3.

Sample	Average (MPa)
Control	0.0381
1M HCl	0.0465
2M HCl	0.0554
1M LiCl	0.0513
1M NaCl	0.0534
1M KCl	0.0546
1M MgCl ₂	0.0801
1M CaCl ₂	0.0964

Table 7.2 Average moduli of each hydrogel samples across all three batches.

7.4 Conclusion

Graphene hydrogel samples with consistent microstructure were synthesized through a non-chemically assisted hydrothermal reduction process, which then infiltrated with various monovalent and divalent salt solutions. The samples were able to retain a consistent amount of monovalent (Na, K) and divalent (Mg, Ca) cations even after washing. The samples were then compressed multiple time to measure its mechanical properties, during which the elastic moduli of each samples were derived. Results showed that the elastic moduli were increased significantly by the intercalation of divalent Mg^{2+} and Ca^{2+} ions, whereas the monovalent ions affect the elastic moduli of the samples to a lesser degree.

CHAPTER 8

Conclusions and Recommendations for Future Work

Graphene has become intensively studied material for electrochemical energy storage device in the last decade. While the two-dimensional electrode design, using graphene based films and particles, have achieved excellent electrochemical performance in numerous reported literature, the use of a three-dimensional and multi-axial flexible graphene based hydrogel electrode allows the designs of a new class of multi-functional Li-ion batteries and supercapacitors to be possible.

As reported in Chapter 4, Graphene hydrogel composites with silicone nanoparticles were successfully incorporated into the design of a high-performance Li-ion battery cell, demonstrating excellent gravimetric energy density and cycling performance even at high C-rate. These composites, comprised of self-assembled 3D GH network with embedded Si nanoparticles coated with an ultrathin layer of SiO_x , were synthesized via a two-step solution-based process. These composites provided large specific surface areas for efficient loading of Si@SiO_x particles and accommodated volume changes of Si, while providing large amount of lithium-ion diffusion channels, fast electron transport kinetics, and excellent penetration of electrolyte solutions within their microstructure. Electrodes constructed with these composites showed outstanding rate capability (1020 mAh g^{-1} at 4 A g^{-1}) and good cyclic stability (1640 mAh g^{-1} , 80% capacity retention between 10 and 140 cycles at 0.1 A g^{-1}). This study demonstrated an exciting pathway to the rational design and fabrication of 3D graphene matrix for application in LIBs and other electrochemical energy storage materials. Future in this aspect of the dissertation research could involve further improving performance of the device by increasing the volumetric density of the

hydrogel based electrode, which can be achieved by synthesis of hydrogel of denser porous structures with higher specific surface area.

For applications in electrochemical supercapacitors, a three-dimensional elastomeric electrode design offered significant advantages to the traditional film and sheet electrode configurations. In particular, the elastomer like properties of the hydrogel offered the opportunity to design multi-functional device that could not act as energy storage but also be able to capture the mechanical energy of the elastic deformation performed on the electrode, by varying its capacitance as the electrode is deformed.

To better study the effects of mechanical properties of graphene and graphene hydrogel, a two-part study was conducted as part of this dissertation. In Chapter 5, the existence of deformation induced facile defects on reduced graphene oxide coating was observed on a flexible three-dimensional polyurethane substrate. The exposed edge plane of the graphene layers significantly affects the electrochemical properties of the constructed device as a result. While the use of porous three-dimensional substrate subjected the graphene coating to complex bending deformations, future work could involve a quantitative study of the formation of such deformation-induced defects on a two-dimensional system, which offers better experimental control and ease of characterization.

In Chapter 7, manipulation of the elastic modulus of single phase reduced graphene oxide hydrogel was achieved through introduction of ions through a solution based infiltration process. Divalent cations of Mg^{2+} and Ca^{2+} were particularly effective in increasing the elastic modulus of the hydrogel by introducing additional cross-links between the loose stacked graphene layers of the hydrogel structure—consistent with previous literature reports on effects of divalent cations on mechanical stability of two-dimensional graphene thin films. Contemporary literature has reported

limited study on the possible chemical and physical interactions between the divalent cations and graphene and its chemical derivatives, graphene oxide and reduced graphene oxide. Nonetheless, the exact mechanism of cross-linking between graphene layers by cations is still not well understood. Future work could involve theoretical studies through computational modeling of the interaction between intercalated cations and the chemical structure of graphene and the functional groups of its chemical derivatives.

Using the knowledge gained from previous studies in this dissertation and other work conducted during author's graduate study, a novel method of synthesizing nanoparticle embedded hydrogel composite was demonstrated in Chapter 6. A mechanical spray drying process was successfully implemented to wrap the hydrophobic exterior of graphite and MnO_2 particles with hydrophilic GO sheets. The resulting powder was then suspended with GO suspension and then underwent chemically assisted (L-ascorbic acid) hydrothermal reduction to form rGO hydrogel. By filling the porous PU substrate of these suspended mixtures, composite electrode materials can be formed which retained the highly flexible mechanical properties of the pristine PU substrate. The conductivity and the electrochemical performance was improved two to three times that of the PUrGO composite reported in Chapter 5; however, the use of non-conductive PU substrate still significantly hinders the performance the composite electrodes, particularly at high current densities. Significant improvement to the electrochemical performance of the hydrogel composite can be reached in future studies by replacing the non-conductive polyurethane substrate with that of a conductive one. Candidate materials for such use include conducting polymers and flexible metallic foam.

References

1. Kim, Y.A., et al., *Important roles of graphene edges in carbon-based energy storage devices*. Journal of Energy Chemistry, 2013. **22**(2): p. 183-194.
2. Brodie, B.C., *XIII. On the atomic weight of graphite*. Philosophical Transactions of the Royal Society of London, 1859. **149**: p. 249-259.
3. Yu, A.P., et al., *Graphite nanoplatelet-epoxy composite thermal interface materials*. Journal of Physical Chemistry C, 2007. **111**(21): p. 7565-7569.
4. Shang, N.G., et al., *Catalyst-Free Efficient Growth, Orientation and Biosensing Properties of Multilayer Graphene Nanoflake Films with Sharp Edge Planes*. Advanced Functional Materials, 2008. **18**(21): p. 3506-3514.
5. Novoselov, K.S., et al., *Electric field effect in atomically thin carbon films*. Science, 2004. **306**(5696): p. 666-669.
6. Jiao, L.Y., et al., *Narrow graphene nanoribbons from carbon nanotubes*. Nature, 2009. **458**(7240): p. 877-880.
7. Liu, N., et al., *One-step ionic-liquid-assisted electrochemical synthesis of ionic-liquid-functionalized graphene sheets directly from graphite*. Advanced Functional Materials, 2008. **18**(10): p. 1518-1525.
8. Kim, F., L.J. Cote, and J. Huang, *Graphene oxide: surface activity and two-dimensional assembly*. Adv Mater, 2010. **22**(17): p. 1954-8.
9. Zhu, Y.W., et al., *Graphene and Graphene Oxide: Synthesis, Properties, and Applications*. Advanced Materials, 2010. **22**(35): p. 3906-3924.
10. Park, S. and R.S. Ruoff, *Chemical methods for the production of graphenes (vol 4, pg 217, 2009)*. Nature Nanotechnology, 2010. **5**(4): p. 309-309.

11. Gomez-Navarro, C., et al., *Atomic Structure of Reduced Graphene Oxide*. Nano Letters, 2010. **10**(4): p. 1144-1148.
12. Jang, I.Y., et al., *Exposed Edge Planes of Cup-Stacked Carbon Nanotubes for an Electrochemical Capacitor*. Journal of Physical Chemistry Letters, 2010. **1**(14): p. 2099-2103.
13. Yuan, W., et al., *The edge- and basal-plane-specific electrochemistry of a single-layer graphene sheet*. Sci Rep, 2013. **3**: p. 2248.
14. Sun, C.Q., S.Y. Fu, and Y.G. Nie, *Dominance of Broken Bonds and Unpaired Nonbonding pi-Electrons in the Band Gap Expansion and Edge States Generation in Graphene Nanoribbons*. Journal of Physical Chemistry C, 2008. **112**(48): p. 18927-18934.
15. Xue, Y.H., et al., *Nitrogen-Doped Graphene Foams as Metal-Free Counter Electrodes in High-Performance Dye-Sensitized Solar Cells*. Angewandte Chemie-International Edition, 2012. **51**(48): p. 12124-12127.
16. Long, Y., et al., *Oxidation of SO₂ to SO₃ catalyzed by graphene oxide foams*. Journal of Materials Chemistry, 2011. **21**(36): p. 13934-13941.
17. Lin, Y.R., et al., *Superhydrophobic Functionalized Graphene Aerogels*. ACS Applied Materials & Interfaces, 2011. **3**(7): p. 2200-2203.
18. Zhao, Y., et al., *A Versatile, Ultralight, Nitrogen-Doped Graphene Framework*. Angewandte Chemie-International Edition, 2012. **51**(45): p. 11371-11375.
19. Niu, Z.Q., et al., *A Leavening Strategy to Prepare Reduced Graphene Oxide Foams*. Advanced Materials, 2012. **24**(30): p. 4144-4150.
20. Qiu, L., et al., *Biomimetic superelastic graphene-based cellular monoliths*. Nature Communications, 2012. **3**.

21. Worsley, M.A., et al., *Synthesis of Graphene Aerogel with High Electrical Conductivity*. Journal of the American Chemical Society, 2010. **132**(40): p. 14067-14069.
22. Worsley, M.A., et al., *High Surface Area, sp(2)-Cross-Linked Three-Dimensional Graphene Monoliths*. Journal of Physical Chemistry Letters, 2011. **2**(8): p. 921-925.
23. Xu, Y.X., et al., *Self-Assembled Graphene Hydrogel via a One-Step Hydrothermal Process*. Acs Nano, 2010. **4**(7): p. 4324-4330.
24. Hu, H., et al., *Ultralight and Highly Compressible Graphene Aerogels*. Advanced Materials, 2013. **25**(15): p. 2219-2223.
25. Wu, Z.S., et al., *Three-Dimensional Nitrogen and Boron Co-doped Graphene for High-Performance All-Solid-State Supercapacitors*. Advanced Materials, 2012. **24**(37): p. 5130-5135.
26. Goodenough, J.B. and Y. Kim, *Challenges for rechargeable Li batteries*. Chemistry of Materials, 2010. **22**(3): p. 587-603.
27. Dunn, B., H. Kamath, and J.-M. Tarascon, *Electrical Energy Storage for the Grid: A Battery of Choices*. Science, 2011. **334**(6058): p. 928-935.
28. Li, H., et al., *Research on advanced materials for Li-ion batteries*. Advanced Materials, 2009. **21**(45): p. 4593-4607.
29. Li, J., C. Daniel, and D. Wood, *Materials processing for lithium-ion batteries*. Journal of Power Sources, 2011. **196**(5): p. 2452-2460.
30. Lu, L.G., et al., *A review on the key issues for lithium-ion battery management in electric vehicles*. Journal of Power Sources, 2013. **226**: p. 272-288.
31. Zhang, M., et al., *One-step hydrothermal synthesis of Li₂FeSiO₄/C composites as lithium-ion battery cathode materials*. Journal of Materials Science, 2012. **47**(5): p. 2328-2332.

32. Huang, B., X.D. Zheng, and M. Lu, *Synthesis and electrochemical properties of carbon nano-tubes modified spherical Li₂FeSiO₄ cathode material for lithium-ion batteries*. Journal of Alloys and Compounds, 2012. **525**: p. 110-113.
33. Tarascon, J.M. and M. Armand, *Issues and challenges facing rechargeable lithium batteries*. Nature, 2001. **414**(6861): p. 359-367.
34. Kim, T., et al., *Carbon nanotubes (CNTs) as a buffer layer in silicon/CNTs composite electrodes for lithium secondary batteries*. Journal of Power Sources, 2006. **162**(2 SPEC. ISS.): p. 1275-1281.
35. Ma, H., et al., *Nest-like silicon nanospheres for high-capacity lithium storage*. Advanced Materials, 2007. **19**(22): p. 4067-+.
36. Kim, H. and J. Cho, *Superior lithium electroactive mesoporous Si@Carbon core-shell nanowires for lithium battery anode material*. Nano Letters, 2008. **8**(11): p. 3688-3691.
37. Ma, C.L., et al., *Exfoliated graphite as a flexible and conductive support for Si-based Li-ion battery anodes*. Carbon, 2014. **72**: p. 38-46.
38. Zhou, X., et al., *Self-Assembled Nanocomposite of Silicon Nanoparticles Encapsulated in Graphene through Electrostatic Attraction for Lithium-Ion Batteries*. Advanced Energy Materials, 2012. **2**(9): p. 1086-1090.
39. Johnson, D.C., et al., *Synthesis of copper silicide nanocrystallites embedded in silicon nanowires for enhanced transport properties*. Journal of Materials Chemistry, 2010. **20**(10): p. 1993-1998.
40. Laïk, B., et al., *An electrochemical and structural investigation of silicon nanowires as negative electrode for Li-ion batteries*. Journal of Solid State Electrochemistry, 2010. **14**(10): p. 1835-1839.

41. Chen, H., et al., *Silicon nanowires coated with copper layer as anode materials for lithium-ion batteries*. Journal of Power Sources, 2011. **196**(16): p. 6657-6662.
42. Hu, L.B., et al., *Si nanoparticle-decorated Si nanowire networks for Li-ion battery anodes*. Chemical Communications, 2011. **47**(1): p. 367-369.
43. Park, M.H., et al., *Silicon nanotube battery anodes*. Nano Letters, 2009. **9**(11): p. 3844-3847.
44. Lee, W.J., et al., *Nanoscale Si coating on the pore walls of SnO₂ nanotube anode for Li rechargeable batteries*. Chemical Communications, 2010. **46**(4): p. 622-624.
45. Song, T., et al., *Arrays of Sealed Silicon Nanotubes As Anodes for Lithium Ion Batteries*. Nano Letters, 2010. **10**(5): p. 1710-1716.
46. Si, Q., et al., *A high performance silicon/carbon composite anode with carbon nanofiber for lithium-ion batteries*. Journal of Power Sources, 2010. **195**(6): p. 1720-1725.
47. Wang, L., et al., *A novel carbon-silicon composite nanofiber prepared via electrospinning as anode material for high energy-density lithium ion batteries*. Journal of Power Sources, 2010. **195**(15): p. 5052-5056.
48. Wu, H., et al., *Engineering Empty Space between Si Nanoparticles for Lithium-Ion Battery Anodes*. Nano Letters, 2012. **12**(2): p. 904-909.
49. Yu, D.S. and L.M. Dai, *Self-Assembled Graphene/Carbon Nanotube Hybrid Films for Supercapacitors*. Journal of Physical Chemistry Letters, 2010. **1**(2): p. 467-470.
50. Yao, Y., et al., *Interconnected Silicon Hollow Nanospheres for Lithium-Ion Battery Anodes with Long Cycle Life*. Nano Letters, 2011. **11**(7): p. 2949-2954.

51. Chen, D., et al., *Reversible lithium-ion storage in silver-treated nanoscale hollow porous silicon particles*. *Angewandte Chemie (International ed. in English)*, 2012. **51**(10): p. 2409-13.
52. Zhang, T., et al., *Core-shell Si/C nanocomposite as anode material for lithium ion batteries*. *Pure and Applied Chemistry*, 2006. **78**(10): p. 1889-1896.
53. Du, C., et al., *Covalently-functionalizing synthesis of Si@C core-shell nanocomposites as high-capacity anode materials for lithium-ion batteries*. *Journal of Materials Chemistry*, 2011. **21**(39): p. 15692-15697.
54. Hu, Y.S., et al., *Superior storage performance of a Si@SiO_x/C nanocomposite as anode material for lithium-ion batteries*. *Angewandte Chemie - International Edition*, 2008. **47**(9): p. 1645-1649.
55. Liu, B., et al., *Hierarchical silicon nanowires-carbon textiles matrix as a binder-free anode for high-performance advanced lithium-ion batteries*. *Scientific Reports*, 2013. **3**.
56. Lee, B.S., et al., *Fabrication of Si core/C shell nanofibers and their electrochemical performances as a lithium-ion battery anode*. *Journal of Power Sources*, 2012. **206**: p. 267-273.
57. Zhao, X., et al., *support-In-Plane Vacancy-Enabled High-Power Si-Graphene Composite Electrode for Lithium-Ion Batteries*. *Advance Energy Materials*, 2011. **1**(6).
58. Zhao, X., et al., *In-Plane Vacancy-Enabled High-Power Si-Graphene Composite Electrode for Lithium-Ion Batteries*. *Advance Energy Materials*, 2011. **1**(6): p. 1079-1084.
59. Lee, J.K., et al., *Silicon nanoparticles-graphene paper composites for Li ion battery anodes*. *Chemical Communications*, 2010. **46**(12): p. 2025-2027.

60. Chabot, V., et al., *A review of graphene and graphene oxide sponge: material synthesis and applications to energy and the environment*. Energy & Environmental Science, 2014. **7**(5): p. 1564-1596.
61. Xu, Y.X., et al., *Flexible Solid-State Supercapacitors Based on Three-Dimensional Graphene Hydrogel Films*. ACS Nano, 2013. **7**(5): p. 4042-4049.
62. Xu, Y., et al., *Functionalized graphene hydrogel-based high-performance supercapacitors*. Advanced materials, 2013. **25**(40): p. 5779-84.
63. Tao, Y., et al., *Towards ultrahigh volumetric capacitance: graphene derived highly dense but porous carbons for supercapacitors*. Scientific Reports, 2013. **3**.
64. Wang, R.H., et al., *Solvothermal-Induced 3D Macroscopic SnO₂/Nitrogen-Doped Graphene Aerogels for High Capacity and Long-Life Lithium Storage*. ACS applied materials & interfaces, 2014. **6**(5): p. 3427-3436.
65. Liu, X., et al., *3D graphene aerogel-supported SnO₂ nanoparticles for efficient detection of NO₂*. Rsc Advances, 2014. **4**(43): p. 22601-22605.
66. Lu, S.T., et al., *Three-Dimensional Sulfur/Graphene Multifunctional Hybrid Sponges for Lithium-Sulfur Batteries with Large Areal Mass Loading*. Scientific Reports, 2014. **4**.
67. Stoller, M.D., et al., *Graphene-based ultracapacitors*. Nano Lett, 2008. **8**(10): p. 3498-502.
68. Wang, Y., et al., *Supercapacitor Devices Based on Graphene Materials*. Journal of Physical Chemistry C, 2009. **113**(30): p. 13103-13107.
69. Wang, D.W., et al., *Fabrication of Graphene/Polyaniline Composite Paper via In Situ Anodic Electropolymerization for High-Performance Flexible Electrode*. ACS Nano, 2009. **3**(7): p. 1745-52.

70. Wu, Q., et al., *Supercapacitors Based on Flexible Graphene/Polyaniline Nanofiber Composite Films*. *ACS Nano*, 2010. **4**(4): p. 1963-1970.
71. Zhang, K., et al., *Graphene/Polyaniline Nanofiber Composites as Supercapacitor Electrodes*. *Chemistry of Materials*, 2010. **22**(4): p. 1392-1401.
72. Yu, A.P., et al., *Ultrathin, transparent, and flexible graphene films for supercapacitor application*. *Applied Physics Letters*, 2010. **96**(25).
73. Wang, H.W., et al., *Cutting and Unzipping Multiwalled Carbon Nanotubes into Curved Graphene Nanosheets and Their Enhanced Supercapacitor Performance*. *ACS Applied Materials & Interfaces*, 2012. **4**(12): p. 6826-6833.
74. Zhang, C.G., et al., *Splitting of a Vertical Multiwalled Carbon Nanotube Carpet to a Graphene Nanoribbon Carpet and Its Use in Supercapacitors*. *ACS Nano*, 2013. **7**(6): p. 5151-5159.
75. Zhao, Y., et al., *Highly compression-tolerant supercapacitor based on polypyrrole-mediated graphene foam electrodes*. *Adv Mater*, 2013. **25**(4): p. 591-5.
76. Tao, Y., et al., *Towards ultrahigh volumetric capacitance: graphene derived highly dense but porous carbons for supercapacitors*. *Sci Rep*, 2013. **3**: p. 2975.
77. Luo, J., H.D. Jang, and J. Huang, *Effect of sheet morphology on the scalability of graphene-based ultracapacitors*. *ACS Nano*, 2013. **7**(2): p. 1464-71.
78. Mao, S., et al., *A General Approach to One-Pot Fabrication of Crumpled Graphene-Based Nanohybrids for Energy Applications*. *ACS Nano*, 2012. **6**(8): p. 7505-7513.
79. Yan, J., et al., *High-performance supercapacitor electrodes based on highly corrugated graphene sheets*. *Carbon*, 2012. **50**(6): p. 2179-2188.

80. Choi, B.G., et al., *3D Macroporous Graphene Frameworks for Supercapacitors with High Energy and Power Densities*. *ACS Nano*, 2012. **6**(5): p. 4020-4028.
81. Ye, S.B., J.C. Feng, and P.Y. Wu, *Deposition of Three-Dimensional Graphene Aerogel on Nickel Foam as a Binder-Free Supercapacitor Electrode*. *ACS Applied Materials & Interfaces*, 2013. **5**(15): p. 7122-7129.
82. Miller, J.R., R.A. Outlaw, and B.C. Holloway, *Graphene electric double layer capacitor with ultra-high-power performance*. *Electrochimica Acta*, 2011. **56**(28): p. 10443-10449.
83. Han, K., et al., *Li₂S-reduced graphene oxide nanocomposites as cathode material for lithium sulfur batteries*. *Journal of Power Sources*, 2014. **251**(0): p. 331-337.
84. Zhang, Y., Y. Huang, and J.A. Rogers, *Mechanics of stretchable batteries and supercapacitors*. *Curr. Opin. Solid State Mater. Sci.*, 2015. **19**(3): p. 190-199.
85. Rogers, J.A., T. Someya, and Y. Huang, *Materials and Mechanics for Stretchable Electronics*. *Science (Washington, DC, U. S.)*, 2010. **327**(5973): p. 1603-1607.
86. Ge, J., et al., *Stretchable Conductors Based on Silver Nanowires: Improved Performance through a Binary Network Design*. *Angew. Chem., Int. Ed.*, 2013. **52**(6): p. 1654-1659.
87. Sekitani, T., et al., *A Rubberlike Stretchable Active Matrix Using Elastic Conductors*. *Science (Washington, DC, U. S.)*, 2008. **321**(5895): p. 1468-1472.
88. Kim, D.-H., et al., *Flexible and stretchable electronics for biointegrated devices*. *Annu. Rev. Biomed. Eng.*, 2012. **14**: p. 113-128.
89. Zang, J., et al., *Stretchable and High-Performance Supercapacitors with Crumpled Graphene Papers*. *Sci. Rep.*, 2014. **4**: p. 6492.
90. Cheng, T., et al., *Stretchable Thin-Film Electrodes for Flexible Electronics with High Deformability and Stretchability*. *Adv. Mater.*, 2015. **27**(22): p. 3349-3376.

91. Zhang, Y., et al., *In-situ synthesis of carbon nanotube/graphene composite sponge and its application as compressible supercapacitor electrode*. *Electrochim. Acta*, 2015. **157**: p. 134-141.
92. Gao, Y., et al., *Transparent, flexible, and solid-state supercapacitors based on graphene electrodes*. *APL Mater.*, 2013. **1**(1): p. 012101/1-012101/7.
93. Samad, Y.A., et al., *Graphene Foam Developed with a Novel Two-Step Technique for Low and High Strains and Pressure-Sensing Applications*. *Small*, 2015. **11**(20): p. 2380-2385.
94. Dimiev, A., et al., *Low-Loss, High-Permittivity Composites Made from Graphene Nanoribbons*. *ACS Appl. Mater. Interfaces*, 2011. **3**(12): p. 4657-4661.
95. Dimiev, A., et al., *Permittivity of Dielectric Composite Materials Comprising Graphene Nanoribbons. The Effect of Nanostructure*. *ACS Appl. Mater. Interfaces*, 2013. **5**(15): p. 7567-7573.
96. Gupta, T.K., et al., *Superior nano-mechanical properties of reduced graphene oxide reinforced polyurethane composites*. *RSC Adv.*, 2015. **5**(22): p. 16921-16930.
97. Yao, H.-B., et al., *A Flexible and Highly Pressure-Sensitive Graphene-Polyurethane Sponge Based on Fractured Microstructure Design*. *Adv. Mater. (Weinheim, Ger.)*, 2013. **25**(46): p. 6692-6698.
98. Chen, T., et al., *Ultra high permittivity and significantly enhanced electric field induced strain in PEDOT:PSS-RGO@PU intelligent shape-changing electro-active polymers*. *RSC Adv.*, 2014. **4**(109): p. 64061-64067.
99. Chen, T., et al., *Achieving High Performance Electric Field Induced Strain: A Rational Design of Hyperbranched Aromatic Polyamide Functionalized Graphene-Polyurethane Dielectric Elastomer Composites*. *J. Phys. Chem. B*, 2015. **119**(12): p. 4521-4530.

100. Krol, P., et al., *Composites prepared from the waterborne polyurethane cationomers-modified graphene. Part I. Synthesis, structure, and physicochemical properties*. Colloid Polym. Sci., 2015. **293**(2): p. 421-431.
101. Hodlur, R.M. and M.K. Rabinal, *Self assembled graphene layers on polyurethane foam as a highly pressure sensitive conducting composite*. Compos. Sci. Technol., 2014. **90**: p. 160-165.
102. Chen, D. and G. Chen, *In situ synthesis of thermoplastic polyurethane/graphene nanoplatelets conductive composite by ball milling*. J. Reinf. Plast. Compos., 2013. **32**(5): p. 300-307, 8 pp.
103. Ding, J.N., et al., *Electrical conductivity of waterborne polyurethane/graphene composites prepared by solution mixing*. J. Compos. Mater., 2012. **46**(6): p. 747-752.
104. Pushparaj, V.L., et al., *Flexible energy storage devices based on nanocomposite paper*. Proceedings of the National Academy of Sciences of the United States of America, 2007. **104**(34): p. 13574-13577.
105. Gwon, H., et al., *Flexible energy storage devices based on graphene paper*. Energy & Environmental Science, 2011. **4**(4): p. 1277-1283.
106. Bae, J., et al., *Fiber Supercapacitors Made of Nanowire-Fiber Hybrid Structures for Wearable/Flexible Energy Storage*. Angewandte Chemie-International Edition, 2011. **50**(7): p. 1683-1687.
107. Cakici, M., K.R. Reddy, and F. Alonso-Marroquin, *Advanced electrochemical energy storage supercapacitors based on the flexible carbon fiber fabric-coated with uniform coral-like MnO₂ structured electrodes*. Chemical Engineering Journal, 2017. **309**: p. 151-158.

108. Xu, L.L., et al., *Graphene/cotton composite fabrics as flexible electrode materials for electrochemical capacitors*. Rsc Advances, 2015. **5**(32): p. 25244-25249.
109. Yu, Y.Y., et al., *Electromechanical properties of reduced graphene oxide thin film on 3D elastomeric substrate*. Carbon, 2017. **115**: p. 380-387.
110. Zang, J., et al., *Stretchable and high-performance supercapacitors with crumpled graphene papers*. Sci Rep, 2014. **4**: p. 6492.
111. L.J. Gibson, M.F.A., *Cellular Solids: Structure and Properties*. 2nd ed. 1997, New York: Cambridge University Press.
112. Maria C. Militello, S.W.G., *Manganese Dioxide (MnO₂) by XPS*. Surface Science Spectra, 2001. **8**.
113. Biesinger, M.C., et al., *Resolving surface chemical states in XPS analysis of first row transition metals, oxides and hydroxides: Cr, Mn, Fe, Co and Ni*. Applied Surface Science, 2011. **257**(7): p. 2717-2730.
114. Park, S., et al., *Graphene oxide papers modified by divalent ions - Enhancing mechanical properties via chemical cross-linking*. Acs Nano, 2008. **2**(3): p. 572-578.
115. Jiang, X., et al., *Self-Assembly of Reduced Graphene Oxide into Three-Dimensional Architecture by Divalent Ion Linkage*. Journal of Physical Chemistry C, 2010. **114**(51): p. 22462-22465.
116. Chowdhury, I., et al., *Aggregation and Stability of Reduced Graphene Oxide: Complex Roles of Divalent Cations, pH, and Natural Organic Matter*. Environmental Science & Technology, 2015. **49**(18): p. 10886-10893.
117. Yeh, C.N., et al., *On the origin of the stability of graphene oxide membranes in water*. Nature Chemistry, 2015. **7**(2): p. 166-170.

118. Li, A.T., et al., *Incorporating multivalent metal cations into graphene oxide: Towards highly-aqueous-stable free-standing membrane via vacuum filtration with polymeric filters.* *Materials Today Communications*, 2017. **11**: p. 139-146.